Naval Research Laboratory

Washington, DC 20375-5320

NRL/~~MR~~ FR/8120--97-9875

Performance Characteristics of a Retroreflector Array Optimized for LEO Spacecraft

G. Charmaine Gilbreath
Peter B. Rolsma
Robert Kessel
Robert B. Patterson
James A. Georges III

Advanced Systems Technology Branch
Space Systems Development Department

December 31,1997

Approved for public release; distribution unlimited.

REPORT DOCUMENTATION PAGE

Form Approved
OMB No. 0704-0188

Public reporting burden for this collection of information is estimated to average 1 hour per response, including the time for reviewing instructions, searching existing data sources, gathering and maintaining the data needed, and completing and reviewing the collection of information. Send comments regarding this burden estimate or any other aspect of this collection of information, including suggestions for reducing this burden, to Washington Headquarters Services, Directorate for Information Operations and Reports, 1215 Jefferson Davis Highway, Suite 1204, Arlington, VA 22202-4302, and to the Office of Management and Budget. Paperwork Reduction Project (0704-0188), Washington, DC 20503.

1. AGENCY USE ONLY (*Leave Blank*)	2. REPORT DATE	3. REPORT TYPE AND DATES COVERED
	December 31, 1997	Final Report

4. TITLE AND SUBTITLE

Performance Characteristics of a Retroreflector Array Optimized for LEO Spacecraft

5. FUNDING NUMBERS

6. AUTHOR(S)

G. Charmaine Gilbreath, Peter B. Rolsma, Robert Kessel, Robert B. Patterson and James A. Georges III

7. PERFORMING ORGANIZATION NAME(S) AND ADDRESS(ES)

Naval Research Laboratory
Washington, DC 20375-5320

8. PERFORMING ORGANIZATION REPORT NUMBER

NRL/FR/8120–97-9875

9. SPONSORING/MONITORING AGENCY NAME(S) AND ADDRESS(ES)

Space and Naval Warfare Systems Command
SAP/FMBMB (AFOY)
Washington, DC 20050-6335

10. SPONSORING/MONITORING AGENCY REPORT NUMBER

11. SUPPLEMENTARY NOTES

12a. DISTRIBUTION/AVAILABILITY STATEMENT

Approved for public release; distribution unlimited.

12b. DISTRIBUTION CODE

13. ABSTRACT (*Maximum 200 words*)

This report presents a predicted link analysis for the operational characteristics of a retroreflector array designed, built, and space-qualified by the Naval Research Laboratory for Low Earth Orbiting spacecraft. The predictions rest on the combination of numerical analysis and direct laboratory measurements of the retroreflector array's optical properties. The report also describes the assumptions we used for link analysis as they pertain to passes over Midway Research Center. The report includes a description and photo of the array itself, as well as the test and levels used to space qualify the array.

14. SUBJECT TERMS

Satellite laser ranging
SLR
Retroreflectors
Retroreflector
Orbit determination

15. NUMBER OF PAGES

70

16. PRICE CODE

17. SECURITY CLASSIFICATION OF REPORT	18. SECURITY CLASSIFICATION OF THIS PAGE	19. SECURITY CLASSIFICATION OF ABSTRACT	20. LIMITATION OF ABSTRACT
UNCLASSIFIED	UNCLASSIFIED	UNCLASSIFIED	UL

NSN 7540-01-280-5500

Standard Form 298 (Rev. 2-89)
Prescribed by ANSI Std 239-18
298-102

INTRODUCTION AND OVERVIEW

This Report covers recent NRL research and development related to the AEC laser-pellet fusion program. The work covered in this report was primarily carried out under AEC Contract No. AT(04-3)-878 between July, 1973 and June, 1974. In some cases, for the sake of clarity, work not performed during this period has been included. In addition, the report discusses the large complementary program supported by the Defense Nuclear Agency at NRL on the study of laser produced plasmas in high atomic number materials. A significant part of the soft x-ray experimental studies (Chapter V) and all of the numerical modelling studies (Chapter VIII and Chapter IX) were supported by the DNA program. This work has been included in the present report for the sake of completeness and since many of the results obtained are of direct benefit to the AEC laser-fusion effort.

There is some overlap in time, with the period covered by the last NRL report, which was presented to the Laser-Fusion Coordinating Committee in November, 1973. However, it was felt useful to establish the precedent of fiscal year reporting starting with this Annual Report. In the future, a report on the AEC supported laser-fusion studies at NRL will appear on a semi-annual basis.

Studies of laser produced plasmas began at NRL in 1968. Development of a large Q-switched glass laser facility was carried out under ARPA sponsorship. Additional support for laser development was received as part of a DNA-supported program to study the interactions between an expanding laser-produced plasma and an ambient magnetized plasma background. The DNA program also provided NRL with the genesis of its expertise in the study of laser plasma generation and interactions. The glass laser system was developed under joint ARPA and DNA sponsorship to the point where, by FY 72, it represented the state-of-the-art in high power short pulse lasers. The system included an NRL designed mode-locked YAG oscillator system and a disc amplifier which became a prototype for those now in use and under development in the laser-fusion program.

When a large AEC supported laser-fusion effort began in FY 72, NRL was a logical place to turn to for support in building up the programs of the AEC laboratories. Shortly after the start of AEC-supported work at NRL, a DNA program at NRL was initiated to study laser produced high atomic number plasmas. The aim of this program was to develop a new source of soft x-rays for weapons effect simulation. The combined AEC and DNA supported programs have been known within NRL as the Laser-Matter Interaction (LMI) Program and Dr. John Stamper has served as Program Manager since its inception. The LMI Program has included contributions from a number of divisions at NRL and has involved both experimental and theoretical studies. The funding of the program during FY 74 consisted of $500,000 from the AEC for laser-fusion studies as well as additional funding from DNA for x-ray source investigations.

One of the unique features of the NRL laser-fusion program has been the availability of a reliable Nd:glass laser system which produces exceptionally clean pulses (i.e., spatially, temporally and spectrally pure) at sufficient power levels ($\lesssim$ 0.5 TW) for many studies of interest to laser fusion. Over 1500 laser shots were put on target in FY 74 for our AEC

CONTENTS

EXECUTIVE SUMMARY E-1

1 INTRODUCTION 1

2 SATELLITE LASER RANGING SYSTEM CHARACTERISTICS 2

2.1 Return Pulse Detection and System Trade-offs 3
2.2 Ground Station Specifications and LEO Orbit Characteristics 4
2.3 Target Diffraction Effects and σ_{LRCS} 5
2.4 Satellite Velocity Aberration 6

3 NRL LEO RETROREFLECTOR ARRAY 7

4 NUMERICAL COMPUTATION OF SATELLITE LASER RANGING PERFORMANCE 8

4.1 Single Circular Retroreflector Far Field Diffraction Patterns and σ_{LRCS} 8
4.1.1 Normal Incidence 8
4.1.2 Off-axis Incidence 10
4.1.3 Bevel Losses 12
4.2 Retroreflector Array Far Field Diffraction Patterns and σ_{LRCS} 15
4.3 Computation of Orbital Performance 16

5 PREDICTED ORBITAL PERFORMANCE 16

5.1 NRL LEO Array Performance in Orbit 16
5.2 NRL LEO Array and Single Retroreflector Performance Comparison 20
5.3 Optical Phase Center and Timing Precision 23
5.4 Further Comparison of Single Retroreflectors and Retroreflector Arrays 26

6 EXPERIMENTAL DETERMINATION OF σ_{LRCS} 28

6.1 Procedure 28
6.2 Calibration 29
6.2.1 Spatial Calibration 29
6.2.2 Radiometric Intensity Calibration 29
6.3 Results and Comparison to Numerical Computation 30

7 SPACE QUALIFICATION OF THE NRL LEO RETROREFLECTOR ARRAY 33

7.1 Random Vibration Tests 33
7.2 Thermal Vacuum Tests 34
7.3 Pyroshock Tests 34

8 CONCLUSIONS **34**

ACKNOWLEDGMENTS **34**

ACRONYMS **35**

REFERENCES **35**

Appendix A - DIFFRACTION PATTERN AND PASS GEOMETRY CALCULATIONS **37**

A.1 Circular Retroreflector Far Field Diffraction Patterns 37
A.2 Converting Pass Geometry to $k_x k_y$ Space 43

Appendix B - SCILAB LISTINGS **46**

B.1 Circular Retroreflector Directly Overhead Without Bevels 46
B.2 Circular Retroreflector Off Normal Incidence Without Bevels 46
B.3 Circular Retroreflector Off Normal Incidence With Bevels 47
B.4 Conversion to $k_x k_y$ 49

Appendix C - SPACECRAFT ENGINEERING DEPARTMENT SPACE QUALIFICATION REPORT **53**

C.1 Test Report for the Retroreflector Array 53
C.2 Test Procedure for the Retroreflector Array 57
C.3 Final Acceptance Test Report of the Retroreflector Array 58

EXECUTIVE SUMMARY

This report presents a full characterization of an optical retroreflector array designed for use with satellite laser ranging on low Earth orbit (LEO) spacecraft. The array was designed to provide a robust optical link from spacecraft in a circular orbit of about 1,100 km using typical NASA-like ground stations, including the small transportable laser ranging systems. The array will provide unambiguous returns for elevation angles above 20° for daytime and nighttime ranging. Consistent with requirements for precision position estimation, the optical configuration will provide phase errors no greater than those equivalent to a centimeter in ranging errors. The nominal site location for the analysis was Midway Research Center (MRC) in Quantico, Virginia.

Based on the analysis and experimental verification presented in this report, we show that the NRL LEO retroreflector array will meet these operational bounds well within margin. Furthermore, the array will also close a link for a system as modest as the field-transportable laser radar station (FTLRS) 13-cm aperture system on Capraia Island off the Tuscan coast. This latter analysis supports the potential of configuring a compact, transportable laser radar to obtain sub-meter, near real-time, satellite ephemerides.

In the course of the analysis and design, a suite of tools was developed to analyze performance for single cubes and retroreflector arrays of any size and configuration. The tools include numerical models that predict a given configuration's optical characteristics in terms of laser radar cross section (LRCS or σ_{LRCS}). A second part of the tool set combines LRCS with ground station characteristics, atmospheric properties, and orbit dynamics to yield the numbers of both photons and photoelectrons for a given orbit over a specific ground site.

The array itself is compact and lightweight; it employs 22 1-cm retroreflectors mounted on a hemisphere to provide a σ_{LRCS} of greater than 10^4 m^2 for all elevation angles above 20° with 108° field of view (FOV). It weighs 221 grams and measures 82 mm in diameter by 43 mm in height.

Analysis was verified experimentally by using a compact far field test bed. Comparison showed good agreement between the array's numerically modeled and measured optical characteristics. Manufacturing defects in the wave front quality of the retroreflectors direct energy to a slight extent into sidelobes (less than 2%). This redirection of energy into the sidelobes actually improves the link's performance by providing some compensation for velocity aberration.

Results were compared to the predicted performance of a single retroreflector. The comparison showed that the FOV would be severely restricted by using the single retroreflector, hence, orbital sampling would be significantly reduced. The number of passes as a function of elevation over a LEO ground repeat track is shown and illustrates quantitatively how limiting FOV in this manner impacts pass yield.

Predicted performance in the near-infrared at 1064 nm is also presented. Advantages of this wavelength include better transmission through the atmosphere and covertness due to transmission in the nonvisible region of the spectrum.

The array was space-qualified and testing specifications are given in Appendix C.

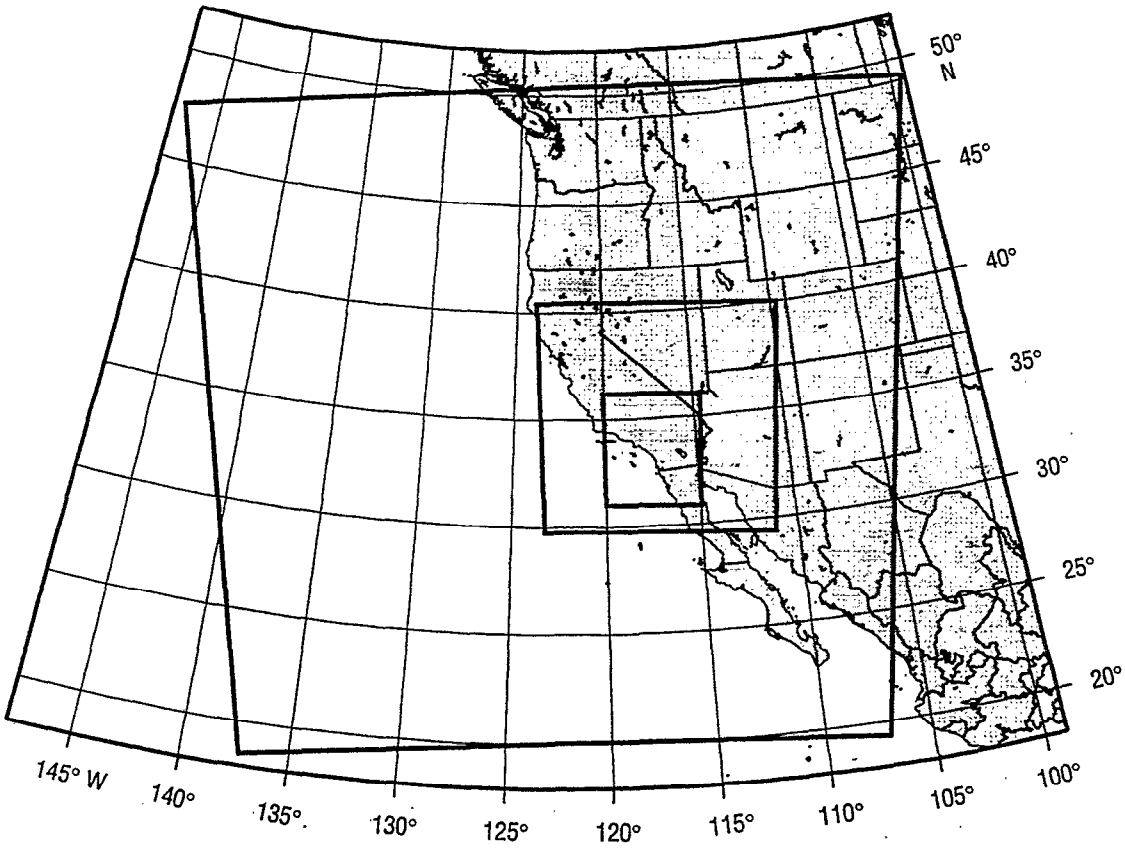

Fig. 1 — COAMPS triple-nested grid with resolutions of 45/15/5 km

to couple a nonhydrostatic, fully compressible atmospheric model to a hydrostatic, incompressible multilevel ocean model. The atmospheric model includes predictive equations for the momentum, nondimensional pressure perturbation, potential temperature, and mixing ratios of water vapor, clouds, rain, ice, and snow. Although the oceanic model is not included in the current version of COAMPS, the surface fluxes of momentum, heat, and moisture are parameterized and computed based on static oceanic fields.

The domain for COAMPS consists of a triple-nested grid, as shown in Fig. 1. While this grid has a 45/15/5-km mesh, the operational version of COAMPS will have a 81/27/9-km mesh. A COAMPS model run consists of an analysis step followed by a forecast run of user-specified length. For the analysis step, all available observations of wind conditions are blended with modeled data from the Navy Operational Global Atmospheric Prediction System (NOGAPS). This provides the initial guess field for COAMPS. Subsequent COAMPS runs obtain an initial guess field from the 12-h forecast of the previous run. All observations are taken from the Fleet Numerical Meteorology and Oceanography Command (FNMOC) operational data base and are quality controlled prior to use by COAMPS. Time-dependent boundary conditions for the inner meshes are provided by the next outer mesh.

A series of *special* COAMPS runs were performed in support of the MEL Integrated Synthetic Scenario Task (Allard 1996). COAMPS was run at 3-h increments for two 2-wk periods: 2 Jan 1995 00Z to 16 Jan 1995 12Z and 11 Aug 1995 00Z to 25 Aug 00Z. Figure 2 depicts the 10-m surface

PERFORMANCE CHARACTERISTICS OF A RETROREFLECTOR ARRAY OPTIMIZED FOR LEO SPACECRAFT

1 INTRODUCTION

This report presents a full characterization of an optical retroreflector array designed for use with satellite laser ranging (SLR) on low Earth orbit (LEO) spacecraft. The array was designed to provide a robust optical link from a spacecraft in a circular orbit of about 1,100 km using typical NASA-like ground stations, including a small transportable laser ranging system (TLRS). The optical configuration was to provide phase errors no greater than those equivalent to a centimeter in ranging errors. The nominal site location for the analysis was Midway Research Center (MRC) in Quantico, Virginia.

Satellite laser ranging provides a powerful data type for precise orbit determination. Position estimation based on direct detection SLR can have performance comparable to a differential global positioning system (GPS) estimation and is used as the referenced "truth" by the scientific community for geoscience and navigation. Although SLR data can generate a highly precise orbit estimator, it is weather-dependent. Therefore, this data type is uniquely suited for independent system performance validation of onboard spacecraft systems and for periodic calibration [1].

Significant information given in this report includes:

1. Link analyses providing the expected on-orbit performance of the NRL LEO array for two different ground site telescope configurations at MRC;
2. Link analyses of a single retroreflector and the NRL LEO array for a TOPEX/Poseidon pass over the Tuscan island of Capraia using a 13-cm aperture SLR system;
3. Supporting analyses including the direct numerical computation of a single retroreflector and the NRL LEO array's optical properties;
4. Pass yield as a function of elevation angle and the impact of field of view (FOV);
5. Laboratory measurements of the array's optical properties that validate numerical analyses; and
6. Space qualification results of the array's mechanical properties.

The report opens with a review of SLR systems establishing general terminology. As part of the review, the specific assumptions relevant to the link analyses are stated in Section 2.2. Section 3 describes the basic mechanical properties of the array. Section 4 covers the numerical computations required in the link analyses; notably, Section 4.1 considers single retroreflector optical properties and Section 4.2 extends the methods for a retroreflector array. The core results of this report are the on-orbit performance predictions in Section 5. In Section 6, the report presents experimental

Manuscript approved November 25, 1997

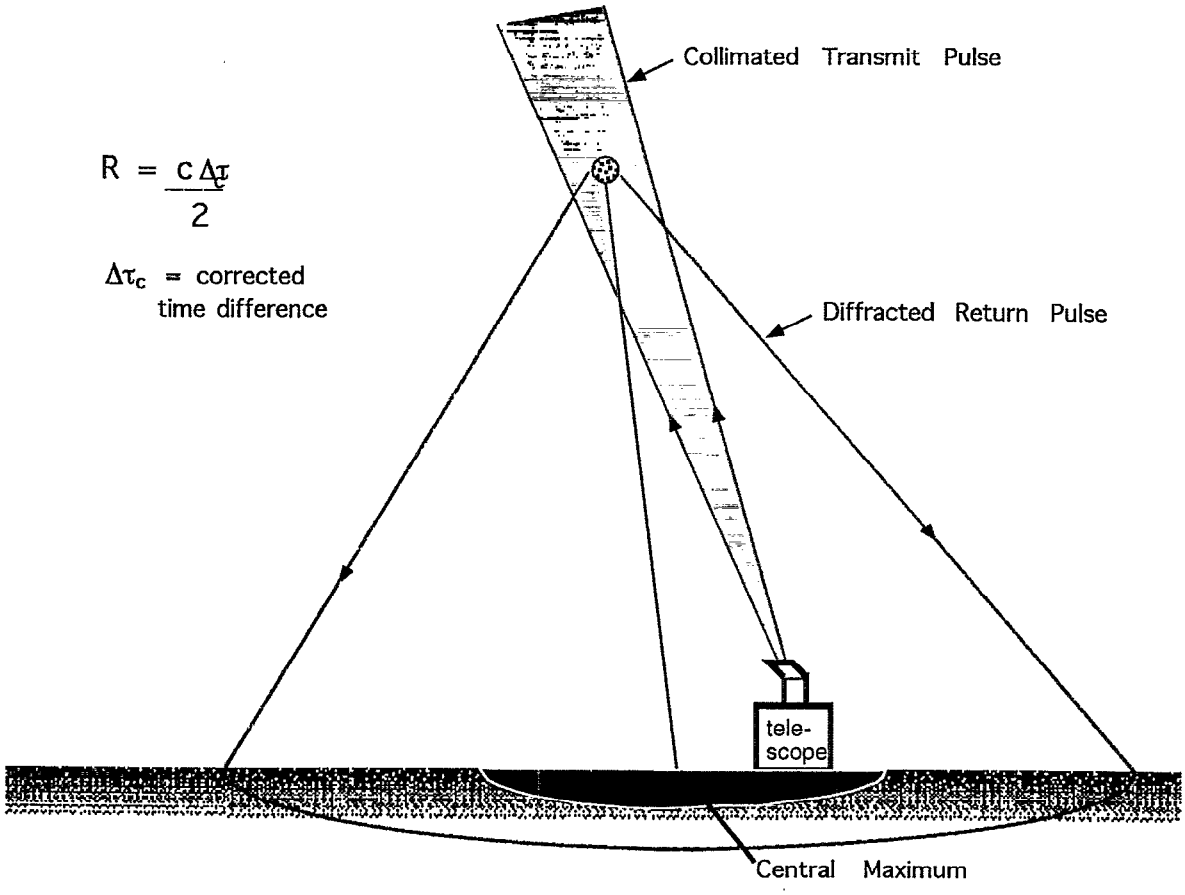

Fig. 1 - Satellite laser ranging (SLR) illustrating time-tagged round trip time of flight of the optical pulses used to determine range to spacecraft. The intensity distribution on the ground is the far field diffraction pattern generated by the size and shape of the target's aperture. The satellite's apparent orbital velocity determines the offset between the central maximum of the diffraction pattern and the ground station.

results that validate the numerical models for optical properties. Section 7 summarizes the space qualification testing of the retroreflector array; Section 8 is the conclusion. Three appendices follow that cover the analytic details of the numerical methods, the full space qualification report, and source code listings. An acronym list is provide at the end of the main text.

2 SATELLITE LASER RANGING SYSTEM CHARACTERISTICS

In the context of this report, satellite laser ranging is direct-detection radar in the optical wavelength regime. When an orbit is properly sampled with a well-calibrated SLR data acquisition system, residuals and accuracies on the order of centimeters are routinely obtained [2].

Figure 1 illustrates basic aspects of the technique. Time-tagged time-of-flight differences are recorded, corrected for system delays, and converted to ranges. These ranges then provide input to an orbit determination model that is used to generate a three-dimensional estimate of the spacecraft's orbit and position.

2.1 Return Pulse Detection and System Trade-offs

The number of photoelectrons generated by an SLR system is given by the laser radar link equation

$$N_{\mathrm{pe}} = \eta_D E_0 \left(\frac{\lambda}{hc}\right) \eta_T G_T \sigma_{\mathrm{LRCS}} \left(\frac{1}{4\pi R^2}\right)^2 A_R \eta_R T_a^2 T_c^2 \quad . \tag{1}$$

The factors in Eq. (1) are:

η_D	detector quantum efficiency	σ_{LRCS}	laser radar cross section
E_0	transmit energy	R	slant range
λ	wavelength	A_R	receiver telescope area
h	Planck's constant	η_R	receiver efficiency
c	speed of light	T_a	one-way atmospheric transmission
η_T	transmission efficiency	T_c	one-way cirrus cloud transmission
G_T	transmitter gain		

A requirement of $N_{\mathrm{pe}} \geq 10$ is a conservative standard for link closure and is used in this report. Although transfer efficiencies along telescope optical paths have been relatively stable over the last few decades, detector efficiency continues to improve. Consequently, it is useful to have the return pulse photons reaching the detector N_γ as a system figure of merit:

$$\begin{aligned} N_\gamma &= \frac{N_{\mathrm{pe}}}{\eta_D} \\ &= E_0 \left(\frac{\lambda}{hc}\right) \eta_T G_T \sigma_{\mathrm{LRCS}} \left(\frac{1}{4\pi R^2}\right)^2 A_R \eta_R T_a^2 T_c^2 \quad . \end{aligned} \tag{2}$$

The link closure requirement for photons is $N_\gamma \geq 100$. Equation (2) depends on the telescope aperture A_R. If the photon flux itself is needed for ground station trade studies, it is given by

$$\mathrm{flux}_\gamma = \frac{N_{\mathrm{pe}}}{A_R \eta_R \eta_D} \quad . \tag{3}$$

Based on the ground station specification in Section 2.2, the results of this report are given in terms of N_{pe} and N_γ for a 28-cm aperture and a 1-m aperture, as well as a 13-cm aperture for an extreme limiting case.

The factors in Eq. (1) determine the SLR trade-space and can be grouped into four categories: transfer efficiencies, transmitted pulse magnitude, environmental/orbit parameters, and geometric factors. The three transfer efficiencies, η_D, η_T, and η_R, are fixed by the technology of the ground station. The initial number of photons, $E_0\left(\frac{\lambda}{hc}\right)$, is determined by the laser source. The three environmental/orbital parameters in Eq. (1), R, T_a, and T_c, are usually fixed boundary conditions beyond the experimenters' control. Two of the geometric factors, G_T and A_R, are associated with transmitting and receiving the laser ranging pulse at the ground station. For a Gaussian beam profile, the transmitter gain is

$$G_T = \left(\frac{8}{\theta_T^2}\right) e^{-2(\theta_{\mathrm{point}}/\theta_T)^2} \quad , \tag{4}$$

where θ_T is the divergence half-angle and θ_{point} is the pointing uncertainty. The remaining geometric factor, σ_{LRCS}, is determined by the SLR target and is a primary focus of this report's analyses. It is this factor that can most effectively compensate for the range loss that goes as R^{-4}. Degnan's review [2] provides an extended treatment of each of the parameters in Eq. (1).

Table 1 - Transmitter-Receiver Configurations

	NASA/TLRS@MRC	NRL@MRC	FTLRS@Capraia
Wavelength (nm)	532	532 or 1064	532
Average Energy (mJ)	100	300	100
Pulse Width (ps)	100 at 5 Hz	250 at 10 Hz	100 at 5 Hz
Transmission Path Efficiency	66%	55%	50%
Receiver Path Efficiency	54%	26% day 50% night	—
Detector Efficiency	16%	16%	—
Combined Reciver Path/ Detector Efficency	—	—	20%
Full Angle Beam Divergence (μrad)	100	100	100
Pointing Accuracy (arcsec)	5.4	$1 \rightarrow 2$	5.4

2.2 Ground Station Specifications and LEO Orbit Characteristics

To maximize opportunities for ranging and orbital sampling over the site, the NRL LEO retroreflector array was designed to provide a robust return margin for elevation angles down to the Federal Aviation Administration (FAA) operation limit. Specifically, the NRL LEO retroreflector array design provides a $\sigma_{\mathrm{LRCS}} \geq 10^4$ m^2 throughout the arc above an elevation angle of 20° during a pass, for the limiting case of a TLRS link.

The link analyses presented in this report are grouped into two categories. The primary results for the NRL LEO retroreflector array were computed using a ground station at MRC and a typical LEO orbit, nominally circular, with an altitude of 1,100 km and a 63.5° inclination. The MRC site location is latitude 38°29′52.0770″ N; longitude 75°22′13.4726″ W at 30.3 m above sea level. We have also compared link margins for a single retroreflector and the retroreflector array using the field transportable laser radar station (FTLRS) and a TOPEX/Poseidon orbit. The ground station assumed for this second set of link analyses is located on Capraia Island, latitude 43°0′ N, longitude 9°45′ E. This telescope has a 13-cm aperture and represents one of the extreme limiting cases in the international SLR network. TOPEX/Poseidon satellite and orbit is of interest because the satellite flies in a circular orbit at an altitude of 1,330 km with a 66.0° inclination. The spacecraft itself has a GPS receiver onboard as well as a ring of retroreflectors. These payloads enable independent orbit determination using differential GPS as well as the SLR data type [3].

The MRC link analyses are based on two different transmitter-receiver configurations (Table 1). The first set used the parameters characteristic of NASA's TLRS. The second link was computed based on the NRL Mobile Optical Data Collection Site, which is anticipated to see "first light" in mid-2000. The performance figures for this link should match the NRL SLR system deployed at the Starfire Optical Range (SOR) scaled from SOR's 3.5 m to a 1-m aperture telescope [4]. FTLRS link analyses parameters are also shown in Table 1.

The atmospheric transmission T_a was determined as a function of elevation using MODTRAN. Figure 2 compares atmospheric transmission as a function of elevation at a midlatitude low-elevation coastal site for both 532 nm and 1064 nm wavelengths. As can be seen from this graph, transmission

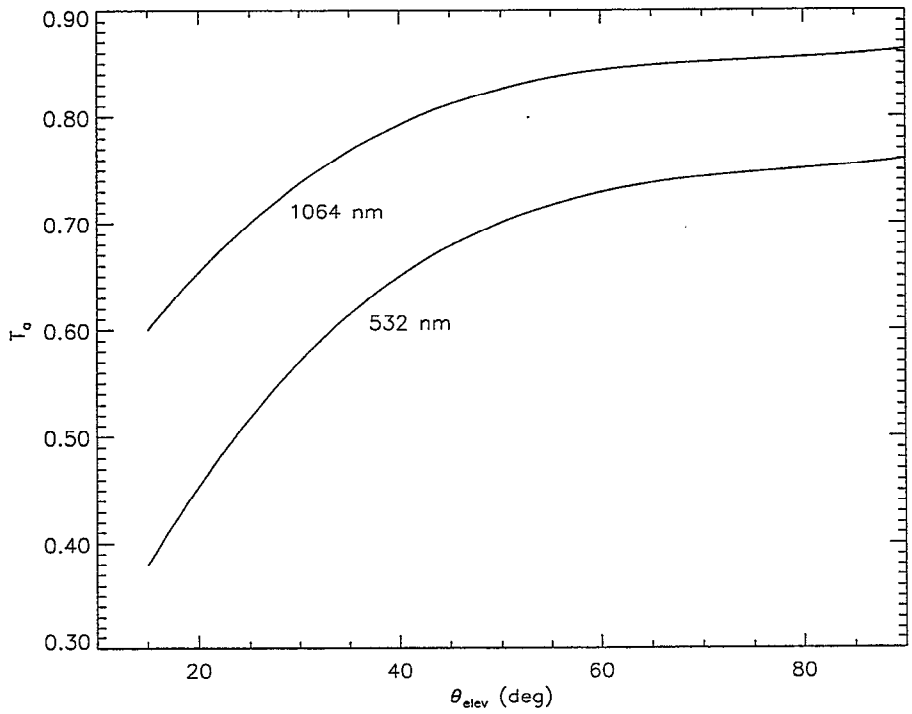

Fig. 2 - MODTRAN estimates for atmospheric transmission T_a as a function of elevation angle θ_{elev} for a clear sky at 532 nm (green) and 1064 nm (near infrared) for a typical midlatitude coastal site

at 1064 nm is better than at 532 nm. Although the NASA SLR system does not use 1064 nm, this wavelength could be available in the NRL@MRC 1-m system. Furthermore, 1064 nm is not visible to the naked eye; it is not likely to disturb neighboring households and is potentially more covert. However, internal gains for detectors in the near-infrared regime are significantly lower than those in the visible (about a factor of 10^3). Therefore, signal amplification in the voltage regime may be required and the related signal-to-noise issues considered. For all link analyses, we assume that no cirrus clouds are present and, hence, $T_c = 1$. All links can detect returns in the daytime, at the day/night terminator boundary, and at night.

2.3 Target Diffraction Effects and σ_{LRCS}

The typical target for an SLR application uses one or more retroreflectors. A corner cube retroreflector is made of three mutually perpendicular reflective flats. The configuration returns light along the path of incidence, and therefore, avoids a requirement for precise orientation of the target with respect to the ground site. However, because the retroreflector's aperture is of finite size, the reflected light is spread by diffraction. The transmitted pulse travels multiple kilometers, and over the retroreflector's aperture the wave fronts are indistinguishable from a plane wave. When combined with the return path, the geometry satisfies the Fraunhofer limit. Consequently, the spatial distribution of the return pulse is the aperture's far field diffraction pattern (FFDP). Furthermore, the FFDP follows standard diffraction scaling in which a smaller aperture retroreflector generates a broader FFDP. The FFDP's breadth is of particular importance since, in combination with the satellite velocity aberration, it plays a significant role in overall SLR system performance.

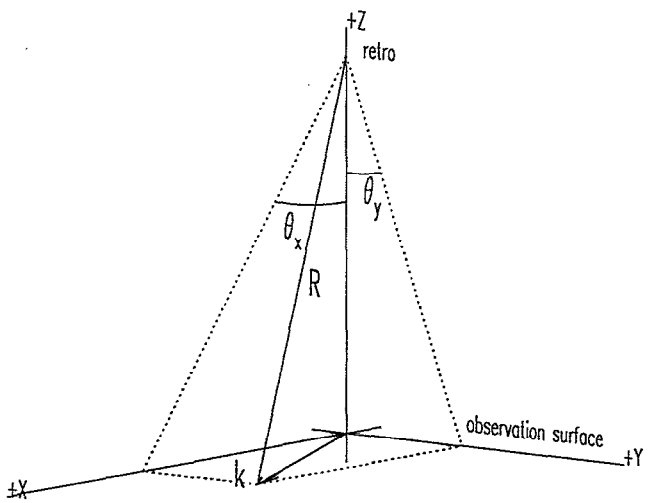

Fig. 3 - Relation between $\vec{k}$ and the angles θ_x and θ_y.

In Eq. (1), the SLR target's diffraction characteristics are carried by σ_{LRCS}. Denoting the FFDP by $\tilde{a}(k_x, k_y)$, the relationship between the two quantities [5, 6] is

$$\sigma_{\mathrm{LRCS}}(k_x, k_y) = \frac{4\pi}{\lambda^2}|\tilde{a}(k_x, k_y)|^2 \quad , \tag{5}$$

where

$$k_x = \frac{2\pi}{\lambda}\sin\theta_x \tag{6}$$

and

$$k_y = \frac{2\pi}{\lambda}\sin\theta_y \quad . \tag{7}$$

The angles θ_x and θ_y define the observation direction. If an FFDP is observed at x_o and y_o from a range R, then $\sin\theta_x = x_o/R$ and $\sin\theta_y = y_o/R$, respectively. One is equally free to use a position and a distance, but for general work it is more convenient to use angles. The results of this report are given in terms of angular measure. Figure 3 shows the relation between $\vec{k}$ and the angles θ_x and θ_y. Equation (5) assumes perfect reflectivity. A more realistic description of a real retroreflector is

$$\sigma_{\mathrm{LRCS}}(k_x, k_y) = \rho\frac{4\pi}{\lambda^2}|\tilde{a}(k_x, k_y)|^2 \quad , \tag{8}$$

where ρ is a reflectivity. In the computations supporting this report, $\rho = 0.75$, which is a conservative estimate that includes manufacturing errors as well the reflectivity loss itself.

2.4 Satellite Velocity Aberration

The terms "velocity aberration," "relativistic effect," and "Bradley effect" all refer to the same physical process. When light signals are observed from a system moving with respect to the source,

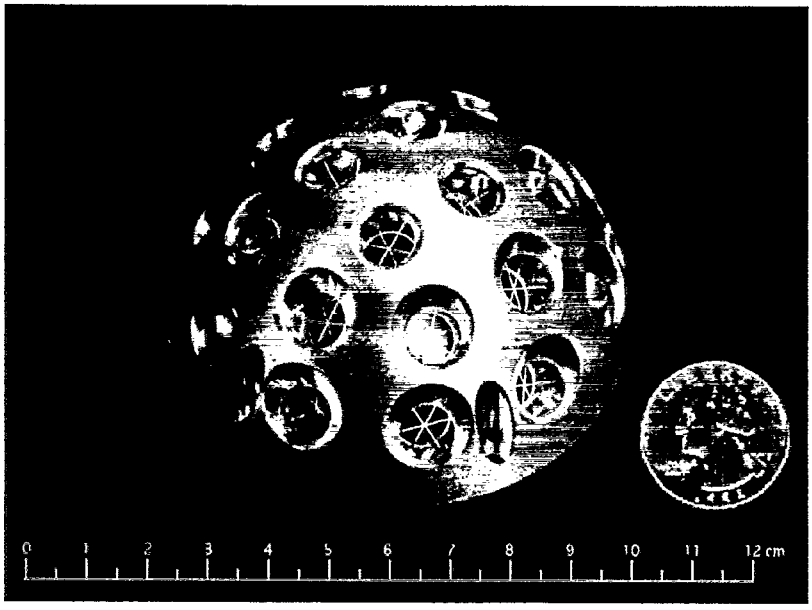

Fig. 4 - The NRL LEO retroreflector array using 22 individual retroreflectors on the surface of hemisphere. This array has a FOV of 108° and $\sigma_{\mathrm{LRCS}} \geq 10^4$ m^2 for $\theta_{elev} \geq 20°$.

their angular relationships change. In the case of SLR, the satellite's motion relative to the ground station causes the part of the intensity distribution from the return pulse that is observed at the ground station to be offset with respect to the central maximum of the diffraction pattern. In SLR parlance, the most common terms for this offset are satellite velocity aberration or the Bradley effect [5]. Figure 1 shows schematically the combined effects of the diffracted return pulse and the velocity aberration. The velocity aberration expressed as a displacement vector in the far field diffraction pattern (or σ_{LRCS}) is given by

$$\vec{\mathrm{k}} = \left(\frac{2\pi}{\lambda}\right)\left(\frac{2\vec{\mathrm{v}}_{\perp}}{c}\right) \quad , \tag{9}$$

where $\vec{\mathrm{v}}_{\perp}$ is the satellite's apparent perpendicular velocity. The displacement vector $\vec{\mathrm{k}}$ selects which value of the instantaneous σ_{LRCS} from Eq. (8) is used in Eq. (1) at each point in time during a satellite's pass over a ground station.

3 NRL LEO RETROREFLECTOR ARRAY

The NRL LEO array comprises 22 1-cm retroreflectors specifically oriented in a 82-mm diameter hemisphere held in an aluminum mount 43 mm in height yielding a total mass, with bolts, of 221 grams. The flight-qualified retroreflectors have 0.004-in. bevels. The retroreflectors are inset slightly, which results in some vignetting (i.e., $c \neq 0$ in Eq. (A8)). The qualification unit has 0.008-in. bevel retroreflectors and is the basis for the analyses and experiments in this report. Figure 4 is a photograph of the array.

The placement of the retroreflectors in an array is determined primarily by its effect on the spatial distribution of return pulse optical energy, rather than strictly mechanical properties. In other words, the location of the retroreflectors should be likened to placement of the elements of an RF antenna. If the retroreflectors are placed incorrectly, it is possible for the array's diffraction

pattern to combine with the velocity aberration and generate a null at the ground station. The NRL LEO array's multiple retroreflectors are specifically placed to provide a field of view (FOV) of 108°, while neither generating such a null nor impacting timing (see Section 5.3). Figure 5 is a mechanical drawing of the array. The retroreflectors are in three rings. The first ring is at 16° with four retroreflectors placed at 0°, 90°, 180°, and 270° in azimuth. The second is at 32° with eight retroreflectors placed at 22.5°, 67.5°, 112.5°, 157.5°, 202.5°, 247.5°, 292.5°, and 337.5° in azimuth. The third is at 48° with 10 retroreflectors placed at 18°, 54°, 90°, 126°, 162°, 198°, 234°, 270°, 306°, and 342° in azimuth.

To compute predicted on-orbit SLR performance for this array, both far field diffraction effects and velocity aberration must be taken into account. Our numerical approach required, as a building block, that we first develop a method to predict the on-orbit SLR performance of a single retroreflector. Consequently, we can compare the predicted performance between the NRL LEO array with that of a single retroreflector. To foreshadow Section 5.2, the returns from the array's multiple retroreflectors for a given pulse mitigates nulls of a single retroreflector σ_{LRCS} and permit a much larger FOV.

4 NUMERICAL COMPUTATION OF SATELLITE LASER RANGING PERFORMANCE

We have developed a set of numerical techniques to predict on-orbit SLR performance. The three basic problems addressed are:

1. computing the σ_{LRCS} of a single retroreflector;
2. combining several single retroreflector σ_{LRCS} values to determine an array's overall σ_{LRCS}; and
3. using orbit dynamic data with the σ_{LRCS} values to compute the actual link analysis.

This section sketches the physical basis for the numerical methods and the relative impact of different SLR properties on performance. The underlying analytic expressions and numerical implementation are presented in detail in Appendix A and Appendix B respectively. The experimental validation of results from these routines is discussed in Section 6.

4.1 Single Circular Retroreflector Far Field Diffraction Patterns and σ_{LRCS}

This section discusses spatial distribution of a pulse return from a single retroreflector caused by diffraction. The section covers the results from our numerical computation of σ_{LRCS} for four cases beginning with the highest symmetry: normal incidence without bevels; tilted incidence without bevels; normal incidence with bevels; and tilted incidence with bevels. Each case serves as a limiting test for the numerical routines of the succeeding cases.

4.1.1 Normal Incidence

When a plane wave pulse hits the retroreflector, it is exactly reversed in direction along the path of incidence. As discussed in Section 2.3, the retroreflector's finite aperture modifies the incidence plane wave pulse and returns a diffracted pulse. At the ground station, the return

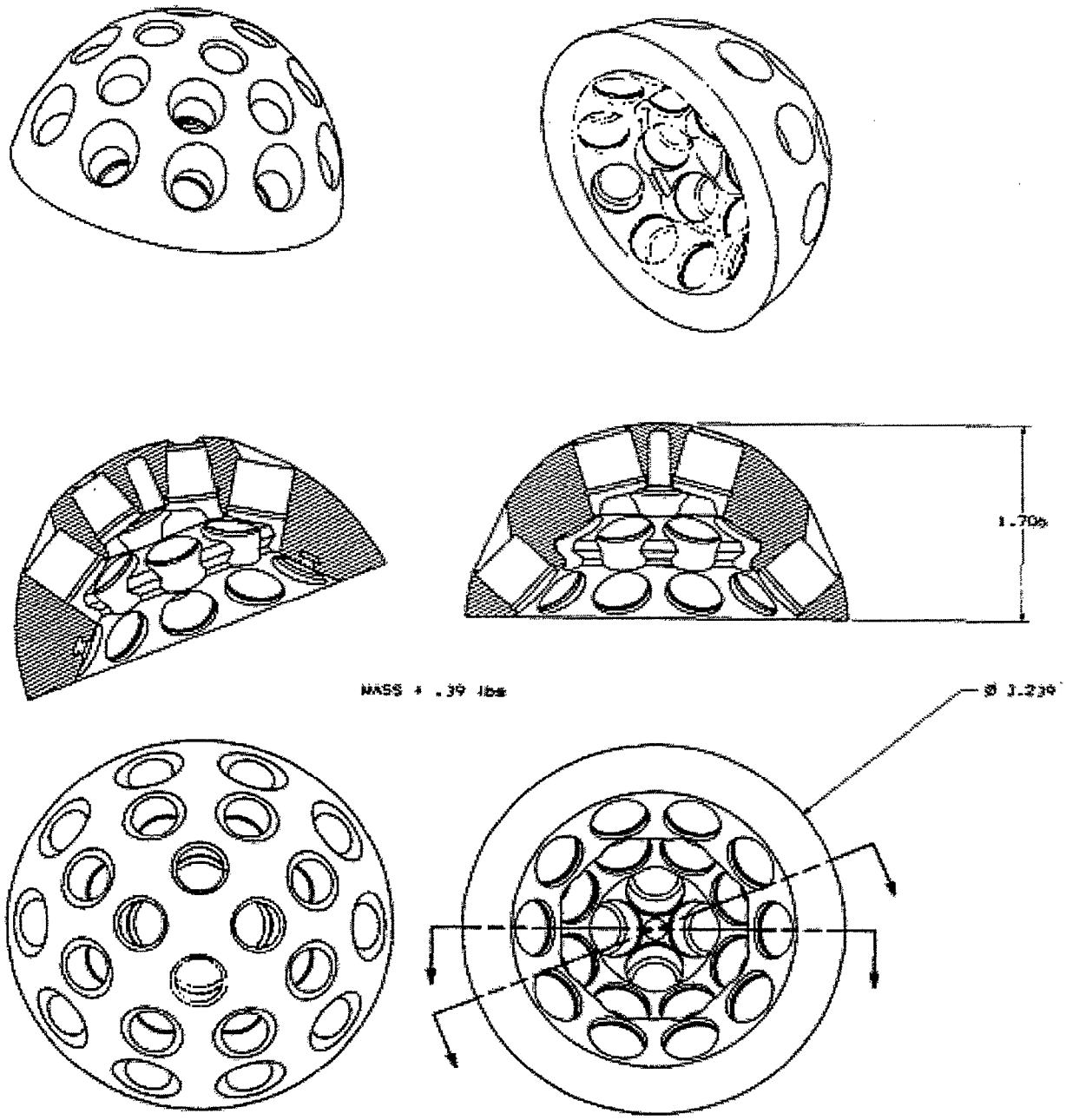

Fig. 5 - NRL LEO retroreflector array

pulse has the spatial distribution of the aperture's far field diffraction pattern. A single circular retroreflector without bevel losses observed at normal incidence provides a geometry with sufficiently high symmetry that an analytic expression exists for the FFDP. The FFDP is the Airy function [7, 8]; hence, from Eq. (5),

$$\sigma_{\mathrm{LRCS}}(k) = \frac{4\pi A^2}{\lambda^2}\left(\frac{2J_1(rk)}{rk}\right)^2 \quad , \tag{10}$$

where A is the area of the retroreflector, r is the retroreflector radius, and

$$k = \frac{2\pi}{\lambda}\sin\theta \quad . \tag{11}$$

At normal incidence, σ_{LRCS} has azimuthal symmetry and Eq. (10) is a function of the single magnitude variable k only. Note that in Eq. (11), θ is the interior angle between the $+Z$-axis and the observation direction in Fig. 3. It is also more convenient to plot σ_{LRCS} in terms the equivalent θ. Even for a σ_{LRCS} form that lacks azimuthal symmetry, k_x and k_y arguments can be specified in terms of a pair of equivalent angles θ_x and θ_y.

Figure 6 shows σ_{LRCS} as function of k (a radial slice in k_x, k_y) for 2.54-cm and 1-cm aperture sizes. Both curves were computed numerically with the FFDP routines described in Appendix A.1 and agree with Eq. (10) to machine precision. The correct geometry required for normal incidence can occur only when the satellite is directly above the ground station and the retroreflector normal is aligned with the nadir direction. The velocity aberration magnitude varies approximately over the range 39 to 49 μrad for a 1,100-km circular orbit (typical LEO spacecraft) and over 38 to 48 μrad for a 1,330-km circular orbit (TOPEX/Poseidon). Thus, as can be seen in Fig. 6, although σ_{LRCS} for the 2.54-cm retroreflector is significantly larger at $k = 0$, the broader FFDP of the 1-cm retroreflector can have a greater LRCS over the critical regions and certainly has greater constancy (less variation) throughout the pattern. Figure 7 is a contour plot of σ_{LRCS} for a 1-cm circular retroreflector as a function of k_x and k_y in terms of μrad.

While Fig. 7 shows σ_{LRCS} over a sizable angular region of the far field, the observation of return pulse is made at a single k_x, k_y point. The velocity aberration given by Eq. (9) selects this single k_x, k_y point and, consequently, the σ_{LRCS} value used in Eq. (1) during the link margin computation. To provide a scale length, for an 1,100-km orbit, the corner points of Fig. 7 at ± 240 μradians correspond to ± 0.264-km distances.

4.1.2 Off-axis Incidence

At all other points in an orbital pass, the retroreflector tips away from normal incidence, so its projected aperture changes in shape and decreases in area. Figure 8 shows how both the shape of the projected aperture and the area changes as a function of incidence angle θ_{inci}. Note that the projected aperture decreases in size along both axes. The decrease in projected aperture size increases the angular extent of the FFDP proportionally and decreases its overall magnitude. The change in aperture shape eliminates azimuthal symmetry so an analytic closed-form expression for the FFDP (e.g., Airy function) is no longer possible. Appendix A.1 describes a method to numerically compute the FFDP.

Figure 9 shows σ_{LRCS} of a tilted 1-cm circular retroreflector computed numerically without bevel losses. The azimuthal symmetry present for normal incidence has been reduced to a two-fold rotational symmetry as seen from the ellipticity of the contours. The central maximum around $k_x = k_y = 0$ remains smoothly rounded. For observations made away from the central maximum,

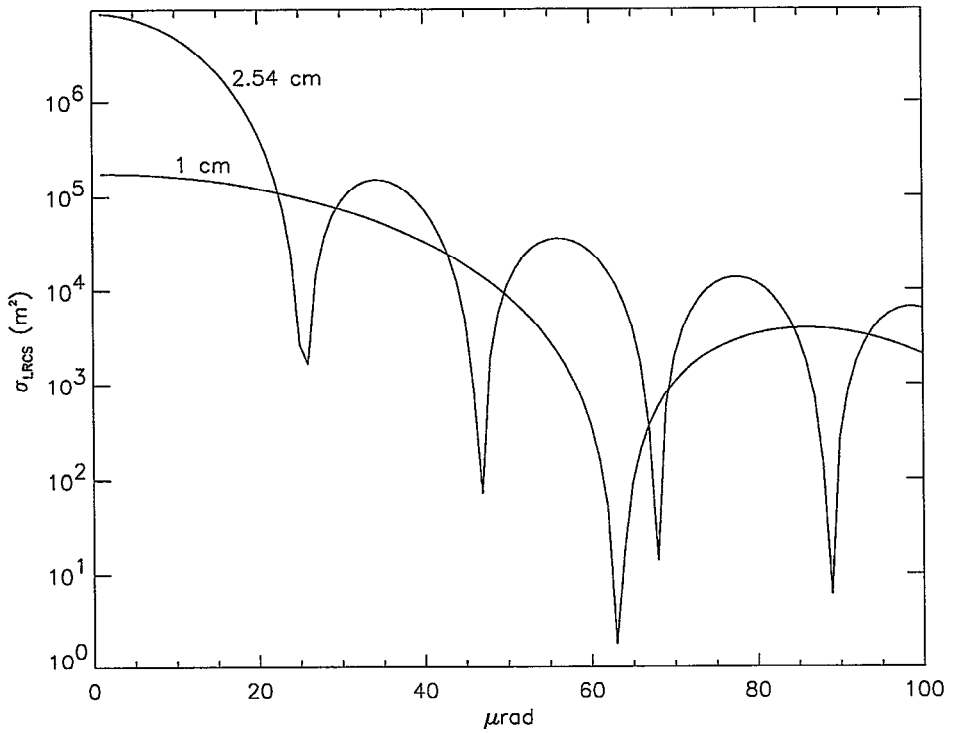

Fig. 6 - σ_{LRCS} at normal incidence for a 2.54-cm (1-in.) and 1-cm circular retroreflectors as a function of k in terms of μrad. For a velocity in the range 39 to 49 μrad, the 1-cm retroreflector has much less variation in σ_{LRCS} than does a 2.54-cm retroreflector.

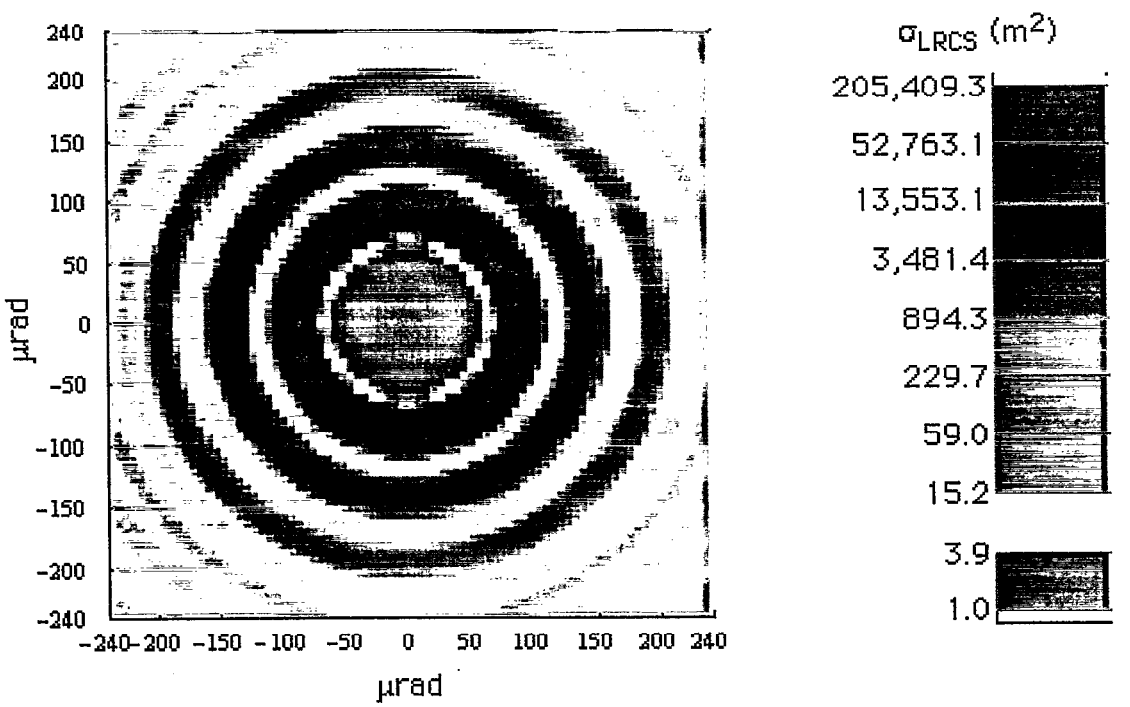

Fig. 7 - σ_{LRCS} at normal incidence for a 1-cm circular retroreflector without bevels as a function of k_x and k_y given in terms of μrad.

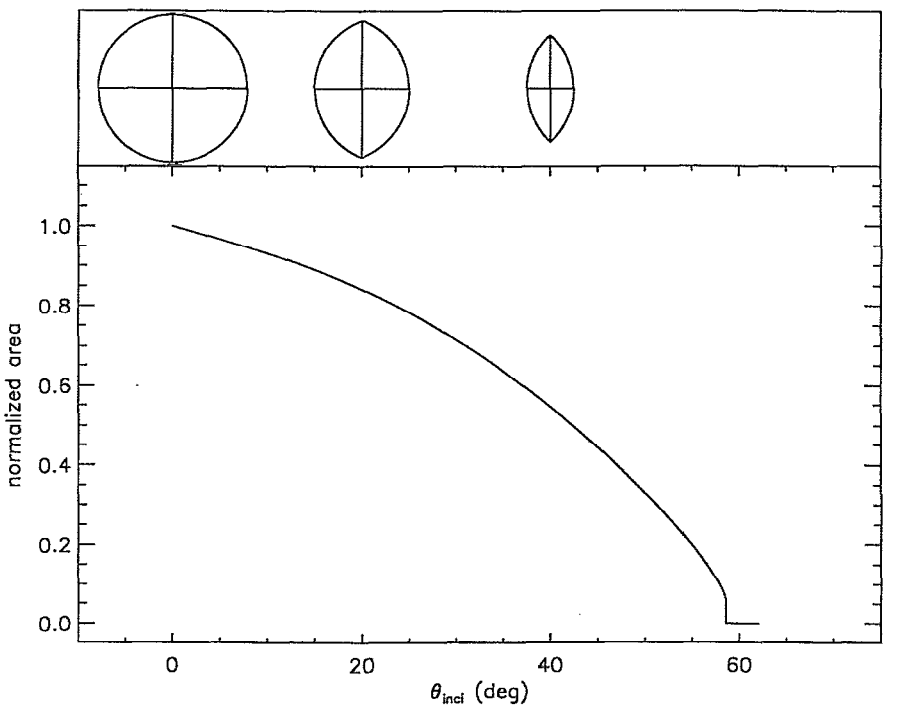

Fig. 8 - (Top) Retroreflector aperture shape: (left to right) Normal incidence; 20° from normal incidence; 40° from normal incidence. (Bottom) Normalized retroreflector aperture area as a function of incidence angle θ_{inci}. FOV cutoff is $\theta_{inci} = 58.579°$, which places a significant limitation on orbit sampling. See Section 5.2.

however, there is a sizable variation in σ_{LRCS} as one holds the magnitude of $\vec{k}$ fixed and sweeps around in k_x, k_y. Physically, this corresponds to tilting the retroreflector axis to a fixed orientation while sweeping the observation direction around the surface of a cone. Figure 10 shows this variation in σ_{LRCS} for a 10° tilt from normal incidence and $|\vec{k}|$ equivalent to 50 μrad as a function of observation direction angle. Note that 50 μrad is approximately the maximum LEO velocity aberration. For smaller velocity aberrations, these variations in σ_{LRCS} are correspondingly smaller as well.

4.1.3 Bevel Losses

Beveled edges are required at the reflecting face plane intersections during the polishing of real retroreflector cubes. Adding bevels introduces narrow loss regions within the aperture. More general versions of our numerical simulations include these losses for both normal incidence and off-normal incidence cases (Sections A.1.3 and A.1.4). At normal incidence, the three bevel loss regions and their reflections generate a six-fold rotation symmetry in diffraction pattern and σ_{LRCS}. Since the bevels are relatively narrow, the six-fold symmetry is more pronounced at larger values of $|\vec{k}|$ beyond the first diffraction minimum. Figure 11 shows σ_{LRCS} at normal incidence of a circular retroreflector computed numerically with losses from 0.008-in. bevels. Figure 12 show the variation in σ_{LRCS} as one sweeps around in k_x, k_y for 0.008-in. bevels at $|\vec{k}|$ equivalent to 50 μrad. The variation in Fig. 12 is only 0.25%.

Comparing Figs. 10 and 12 shows that the effect of tilting the retroreflector is much more significant than adding the bevels. Although our numerical computation treats the bevel's effect

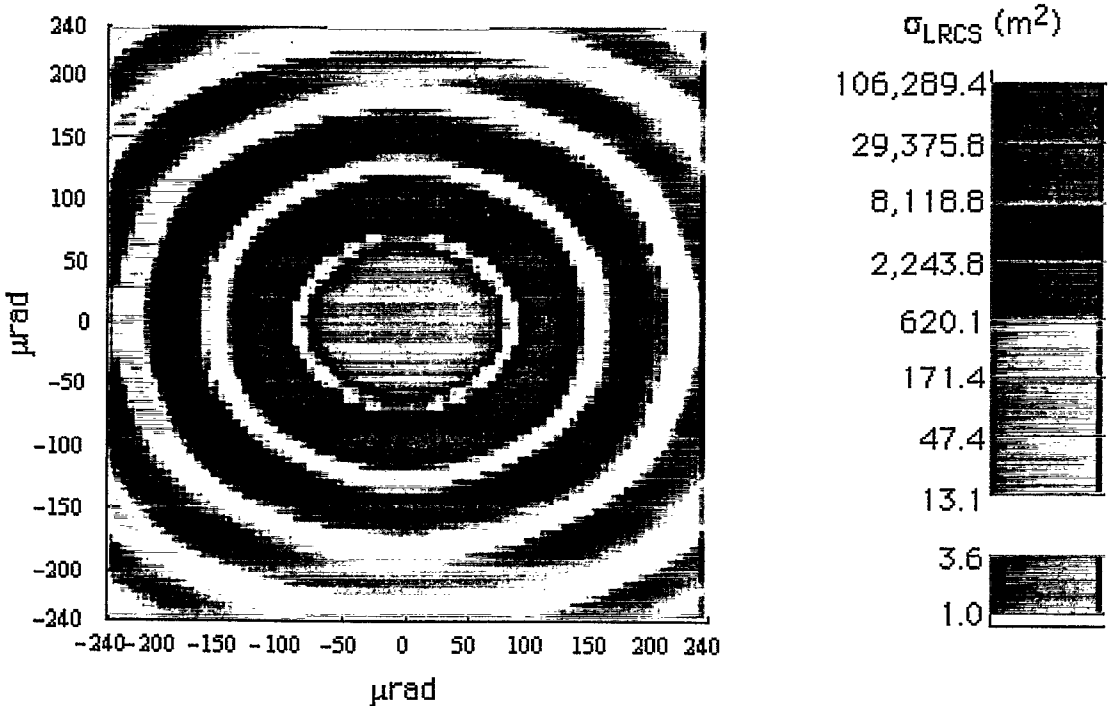

Fig. 9 - σ_{LRCS} of a 1-cm circular retroreflector as a function of k_x and k_y given in terms of μrad, with 10° tilt. Ellipticity of the contours is the result.

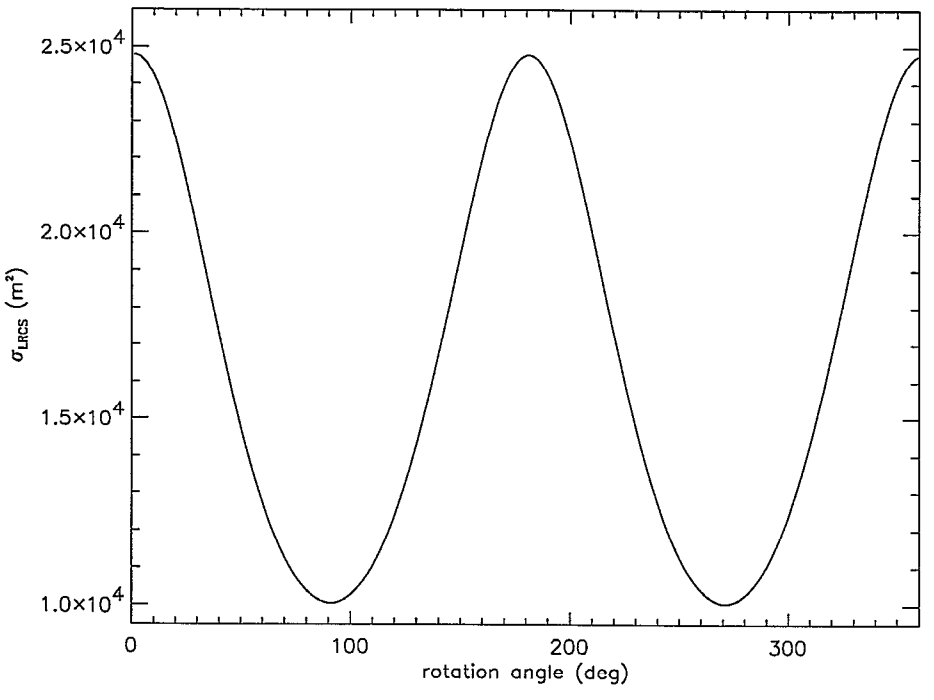

Fig. 10 - Variation in σ_{LRCS} at 10° off-axis from normal incidence of a 1-cm circular retroreflector at $|\vec{k}|$ equivalent to 50 μrad. The variation in σ_{LRCS} from its average caused by a fixed 10° tilt by a rotation of the observation direction is 42%. At the instant of pulse reflection, a satellite's apparent perpendicular velocity determines the observation direction.

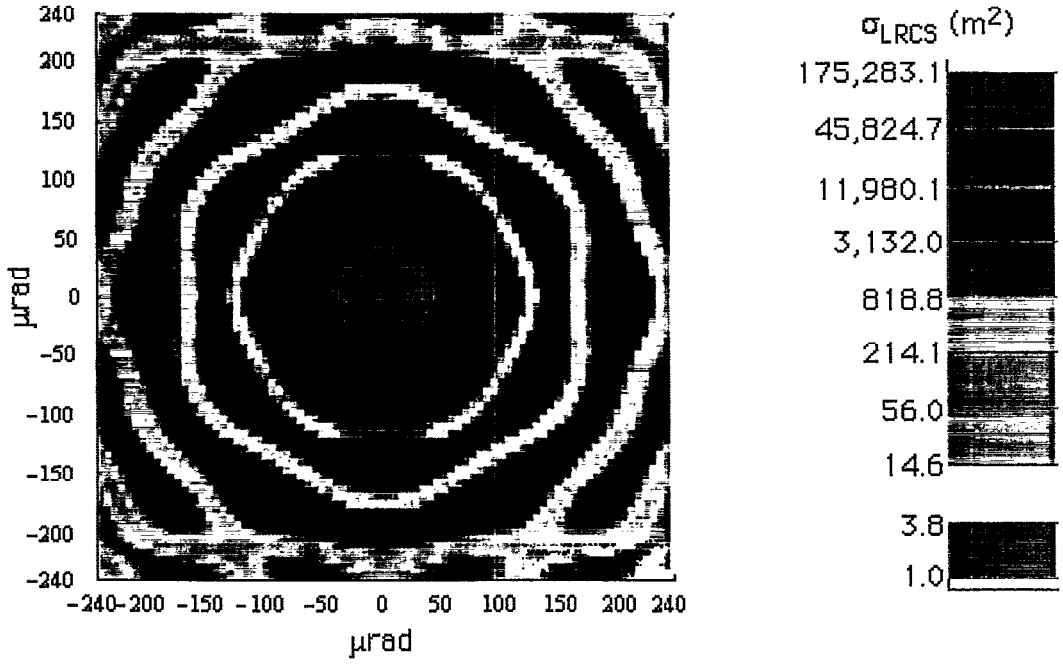

Fig. 11 - σ_{LRCS} of a 1-cm circular retroreflector with 0.02032-cm (or 0.008-in.) bevels as a function of k_x and k_y given in terms of μrad for normal incidence.

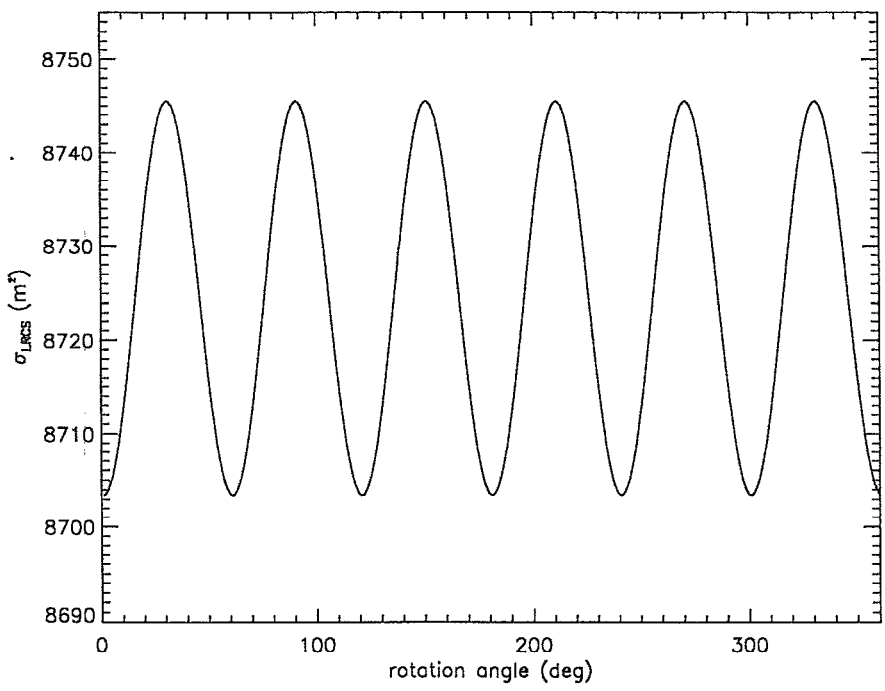

Fig. 12 - Variation in σ_{LRCS} at normal incidence of a 1-cm circular retroreflector at $|\vec{k}|$ equivalent to 50 μrad with 0.02032-cm (or 0.008-in.) bevels. Variation from average σ_{LRCS} caused by bevels is 0.25%

exactly, to first order, the bevels could also be considered as simply a scalar loss of reflecting area combined with a slightly reduced FOV. The combination of both retroreflector tilt and bevel losses requires a slightly more complex numerical simulation, but it does not introduce any qualitatively new features to the FFDP or σ_{LRCS}.

4.2 Retroreflector Array Far Field Diffraction Patterns and σ_{LRCS}

The return pulse is the sum of the contributions from several retroreflectors in the array. The total FFDP $\tilde{a}$ for the array of L retroreflectors at a given instant of time is

$$\tilde{a} = \sum_{l=1}^{L} \tilde{a}_l e^{i\alpha_l} \quad , \tag{12}$$

where the α_ls are the phase angles for each retroreflector for a given incidence direction. From Eq. (8), the instantaneous LRCS is

$$\sigma_{\mathrm{LRCS}} = \rho \frac{4\pi}{\lambda^2} |\tilde{a}\tilde{a}^*| \quad . \tag{13}$$

Upon substitution:

$$\sigma_{\mathrm{LRCS}} = \rho \frac{4\pi}{\lambda^2} \left| \left(\sum_{m=1}^{L} \tilde{a}_m e^{i\alpha_m} \right) \left(\sum_{n=1}^{L} \tilde{a}_n^* e^{-i\alpha_n} \right) \right| \tag{14}$$

$$= \rho \frac{4\pi}{\lambda^2} \left| \sum_{m=1}^{L} \sum_{n=1}^{L} \tilde{a}_m \tilde{a}_n^* e^{i(\alpha_m - \alpha_n)} \right| \quad . \tag{15}$$

During a brief interval τ, variations of phase angle relationships between individual retroreflectors can occur. Provided the statistical correlation between α_m and α_n over τ is small, one is free to treat resulting phase factors as essentially random fluctuations. Consequently, a time-averaged LRCS will simplify to:

$$\overline{\sigma_{\mathrm{LRCS}}} = \rho \frac{4\pi}{\lambda^2} \left| \sum_{m=1}^{L} \sum_{n=1}^{L} \frac{\tilde{a}_m \tilde{a}_n^*}{\tau} \int_0^{\tau} e^{i[\alpha(t)_m - \alpha(t)_n]} dt \right| \quad , \tag{16}$$

$$= \rho \frac{4\pi}{\lambda^2} \sum_{m=1}^{L} |\tilde{a}_m|^2 \quad . \tag{17}$$

For SLR measurements with precisions significantly tighter than ± 1 cm, τ may be become small enough that the phase integral cannot be considered as a Kronecker delta function δ_{mn}. For the LEO application, however, using a random phase approximation is sufficient, and the array's LRCS can be evaluated using the incoherent sum of the contributions in Eq. (17).

Equation (17) is a convenient form for numerical evaluation. The routines developed and tested in the single retroreflector can be used directly to compute the $\tilde{a}_m$s. The primary addition is a routine that combines an incidence direction with respect to the array's axis with individual retroreflector directions to determine which retroreflectors are illuminated within their FOV limits and at what angles. It is then straightforward to compute the relevant $\tilde{a}_m$s and to sum to obtain $\overline{\sigma_{\mathrm{LRCS}}}$. Figure 13 shows $\overline{\sigma_{\mathrm{LRCS}}}$ of the array (using retroreflectors with 0.008-in. bevels) as computed numerically when viewed along the array's axis. (Note that array σ_{LRCS} values used in Section 5 are time-averaged. Unless there is a specific reason to do otherwise, explicit notation of the time-averaging is suppressed for the balance of this report.)

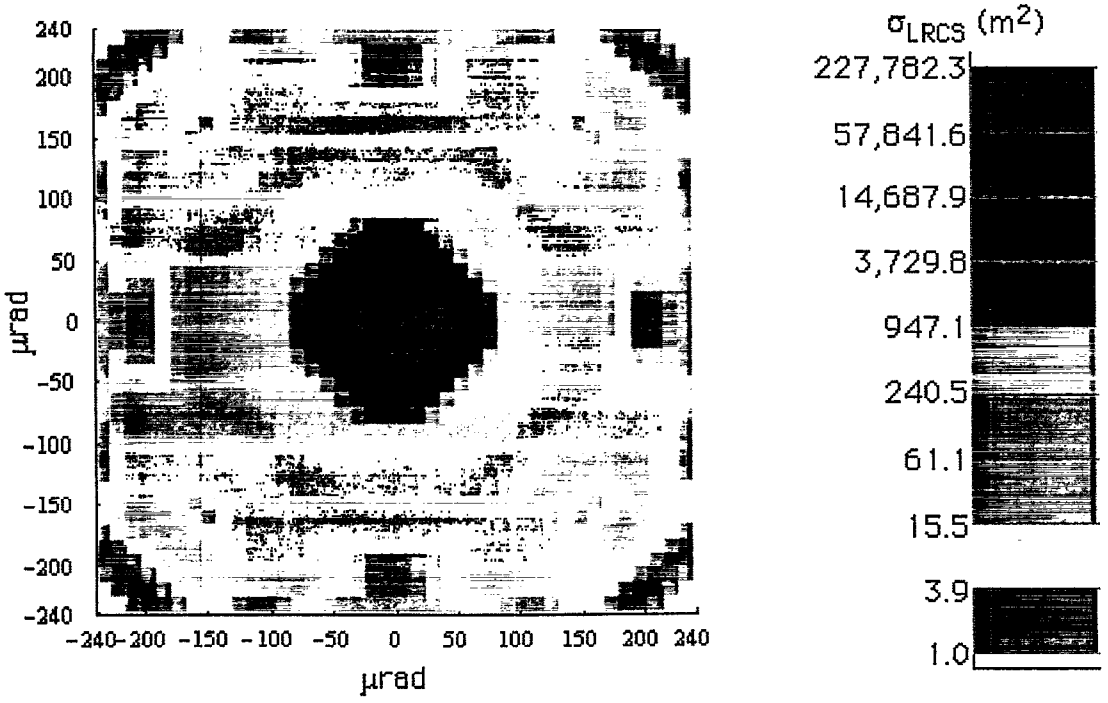

Fig. 13 - NRL LEO retroreflector array $\overline{\sigma_{\mathrm{LRCS}}}$ with 0.008-in. bevels and on-axis incidence

4.3 Computation of Orbital Performance

The local geometry at the satellite and apparent velocity for a given ground station must be used to drive the σ_{LRCS} routines to compute the performance expected for a either the NRL LEO retroreflector array or a single retroreflector on orbit. The range vector, apparent velocity vector, and local elevation angle from nadir are sufficient to determine the k_x, k_y point and the form of σ_{LRCS} that will occur at a given point in time during a satellite's orbital pass. (See Section A.2 for the detailed development.) The SLR performance can then determined with Eq. (1) at each point in time during a pass for which the satellite's attitude and apparent velocity are known.

Computation of a spacecraft's orbital dynamics sufficient to determine the instantaneous attitude and apparent velocity is a separate and specialized task. The ephemeris and attitude data used in this report were supplied by NRL's Electro-Optics Technology Section and Mathematics & Orbit Dynamics Section (Codes 8123 and 8233).

5 PREDICTED ORBITAL PERFORMANCE

5.1 NRL LEO Array Performance in Orbit

As previously discussed, the local geometry and velocity aberration combine to determine σ_{LRCS} at any given instant. Equation (1) can then be used to determine N_{pe} as a function of time during a pass over the ground site. For a nadir-facing array, the local angle from nadir is the angle between the incidence direction and the array's axis. The apparent velocity vector is similarly common to the entire array. As noted in Section 4.2, this information is first converted to the coordinate system of each illuminated retroreflector in the array and then used with Eq. (17) to compute σ_{LRCS}.

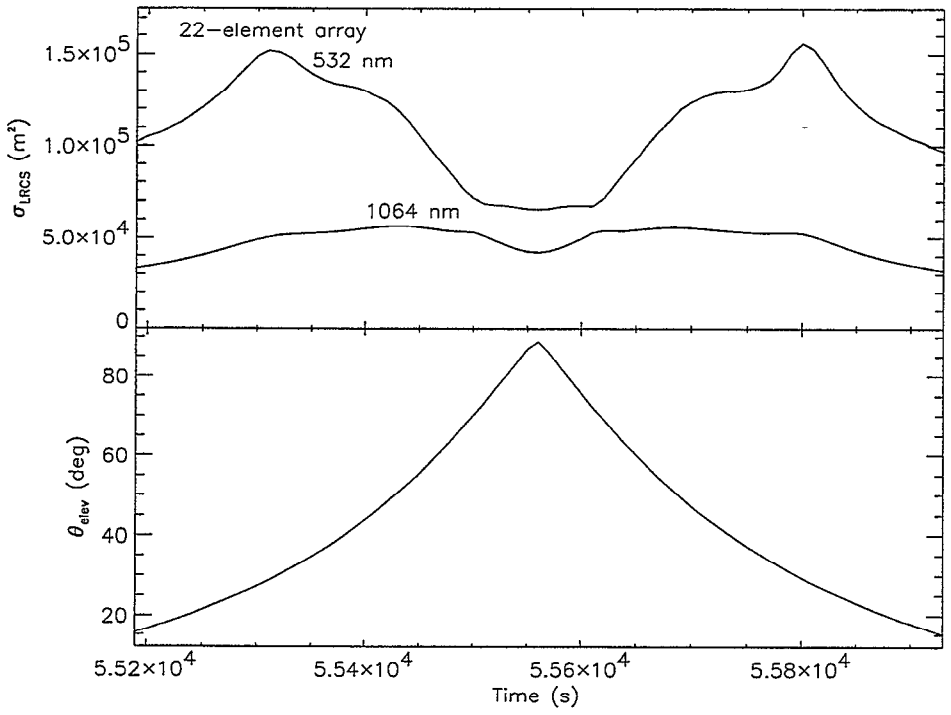

Fig. 14 - σ_{LRCS} of the 22-element NRL LEO retroreflector array at 532 and 1064 nm (top) and θ_{elev} (bottom) as a function of time; this is a near-zenith pass over MRC with $\theta_{elev} = 88°$ at PCA

Figures 14–23 show the NRL LEO retroreflector array's performance on orbit from the MRC ground site. These computations are based on the link parameters for the TLRS and the NRL@MRC system described in Section 2.2, as well as the MODTRAN atmospheric transmission values as a function of pass elevation shown in Fig. 2. We analyzed the link for two typical passes over the MRC site: one that has a near-zenith elevation angle of 88° at point-of-closest approach (PCA), and a second, much lower, pass with $\theta_{elev} = 39°$ at PCA. This comparison determined the impact of low pass geometries and velocity aberration on link closure using the retroreflector array.

Figure 14 shows σ_{LRCS} at 532 and 1064 nm vs time as well as θ_{elev} vs time for the near-zenith pass over MRC. Figure 15 shows the equivalent three curves of 532 and 1064 nm σ_{LRCS} and θ_{elev} vs a common time axis for the low elevation off-zenith pass. As can be seen from Fig. 14, although there is a drop at PCA, σ_{LRCS} remains greater than 10^4 m^2 throughout the entire pass. For the low elevation pass, Fig. 15 shows $\sigma_{\mathrm{LRCS}} \geq 10^4$ m^2 occurring even at the lowest elevation angles. The asymmetry apparent in σ_{LRCS} during the pass is produced by variations in satellite attitude and velocity aberrations. These effects are more pronounced than in a zenith pass. The σ_{LRCS} values plotted in Figs. 14 and 15 were used in Eqs. (1) and (2) for the link analyses shown in Figs. 16–23.

In Figs. 16 and 17, the number of return photons N_γ generated at 532 nm reaching the TLRS telescope's detector are shown during high and low passes, respectively. Figures 18 and 19 show the number of photoelectrons N_{pe} generated as a function of time for these passes at 532 nm using a photomultiplier tube with a quantum efficiency of 16% and an internal gain of 10^6, which is standard technology. Figure 19 clearly shows that the NRL LEO array can close the link with $N_{\mathrm{pe}} \geq 10$ at the low elevations, even with the 28-cm TLRS telescope.

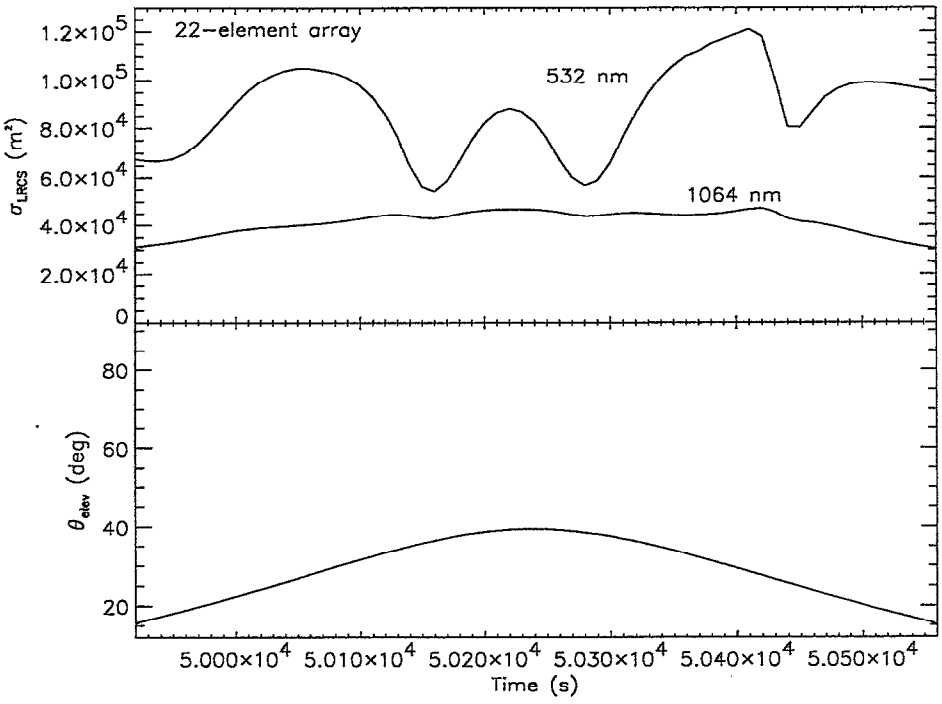

Fig. 15 - σ_{LRCS} of the 22-element NRL LEO retroreflector array at 532 and 1064 nm (top) and θ_{elev} (bottom) as a function of time; this is a low-elevation pass over MRC with $\theta_{elev} = 39°$ at PCA

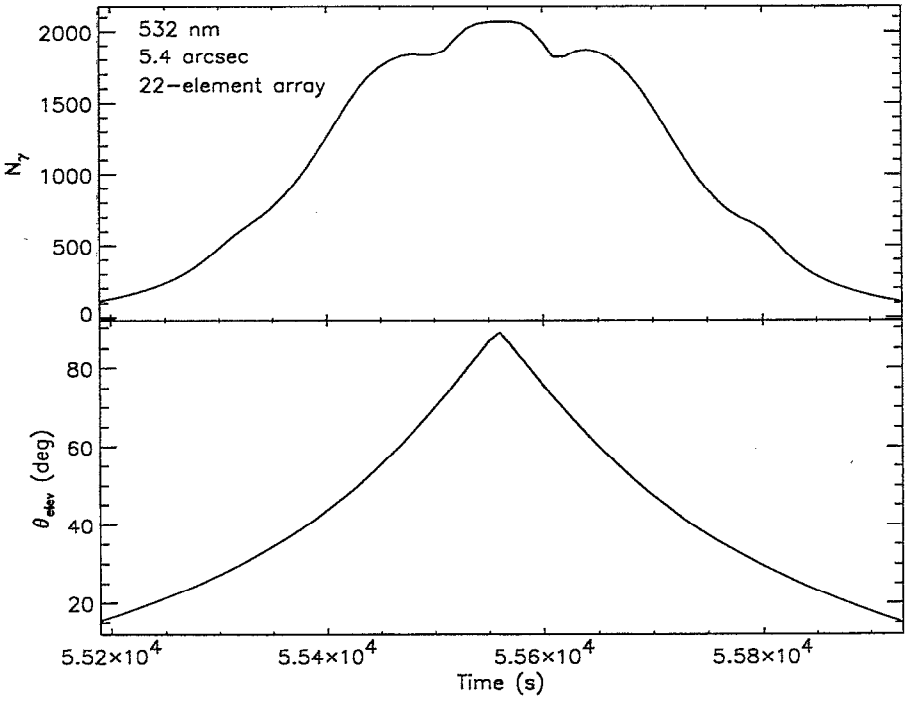

Fig. 16 - N_γ at 532 nm for a 28-cm diameter aperture TLRS telescope and the NRL LEO retroreflector array at MRC (top) and θ_{elev} (bottom) as a function of time during a near-zenith pass

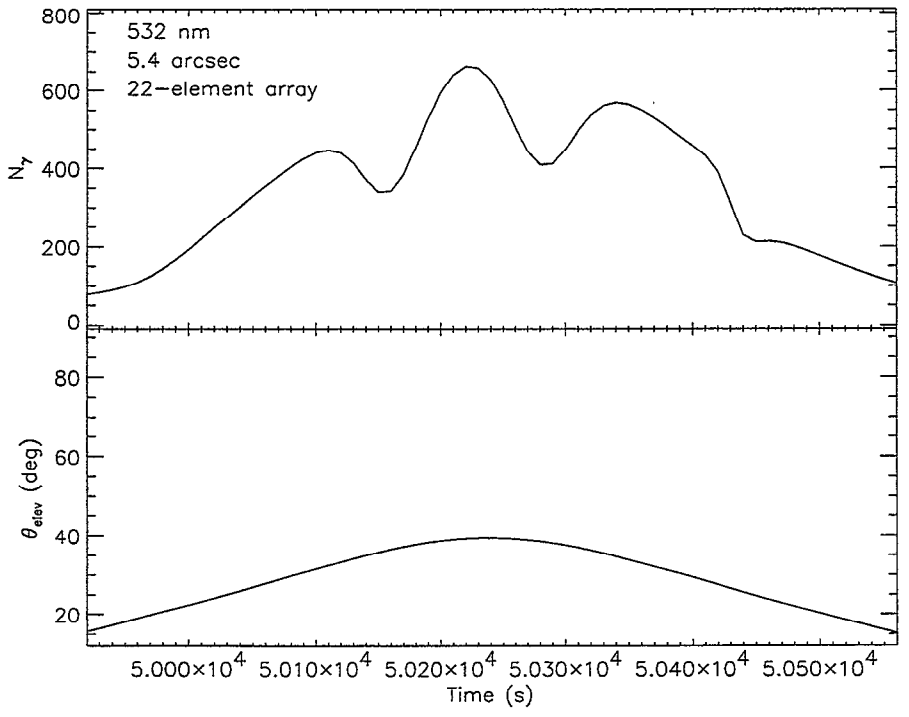

Fig. 17 - N_γ at 532 nm for a 28-cm diameter aperture TLRS telescope and the NRL LEO retroreflector array at MRC (top) and θ_{elev} (bottom) as a function of time during a low pass

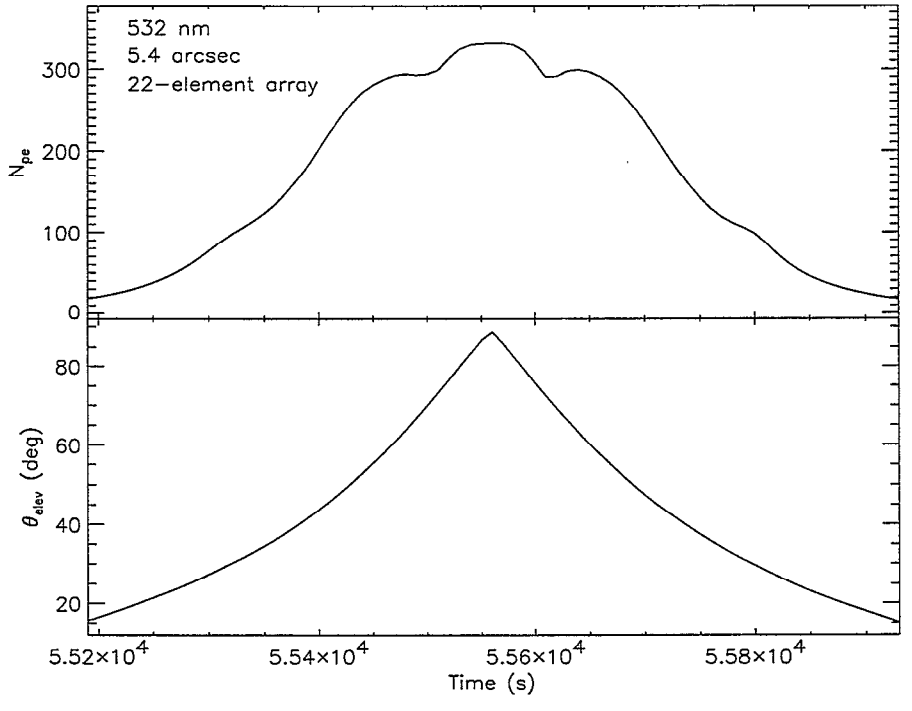

Fig. 18 - N_{pe} at 532 nm for a 28-cm diameter aperture TLRS telescope and the NRL LEO retroreflector array at MRC (top) and θ_{elev} (bottom) as a function of time during a near-zenith pass

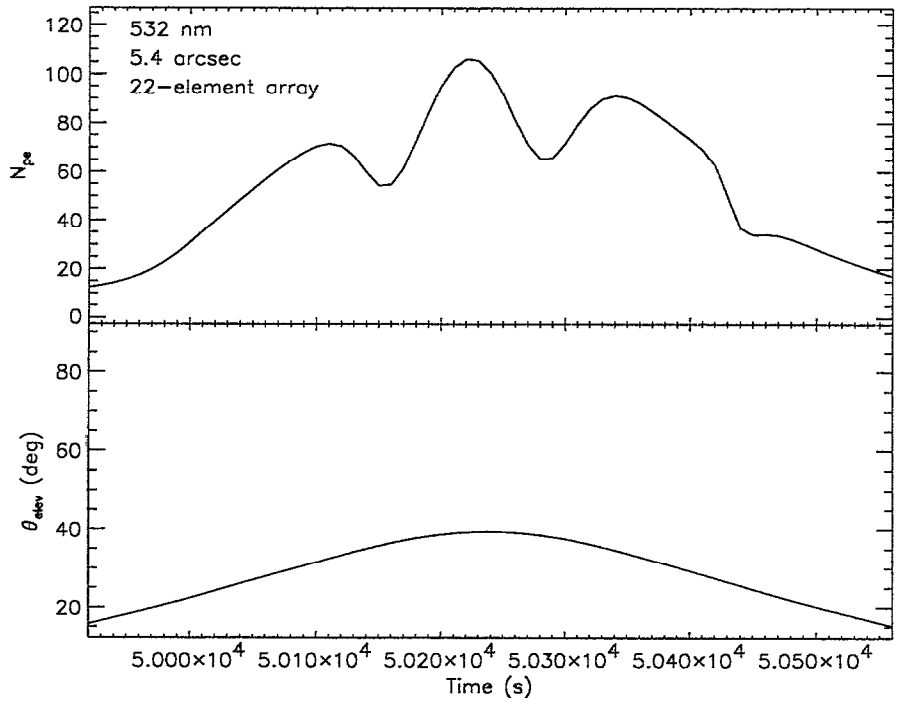

Fig. 19 - N_{pe} at 532 nm for a 28-cm diameter aperture TLRS telescope and the NRL LEO retroreflector array at MRC (top) and θ_{elev} (bottom) as a function of time during a low pass

For the NRL mobile meter class system to be situated at MRC, the link closures for day and night at 532 nm are shown in Figs. 20 and 21, again for high and low passes. Because this telescope system will be under NRL control, the daylight filter can be added or removed as required. Hence, the number of received photoelectrons can be increased during terminator and at night. The advantage of this clearly more robust link is that more unambiguous yield is possible throughout a pass, particularly at the lower elevation angles and daytime operation. This yield is sufficiently high that a postdetector amplifier is not required, and the associated amplifier noise can be eliminated. Thus, orbital sampling over the site is maximized and precision is improved.

Transmission through the atmosphere at 1064 nm is better than at 532 nm as previously discussed (see Fig. 2). Since near-infrared detector technology can be expected to show significant changes, N_γ is a more appropriate figure of merit. Figures 22 and 23 show the N_γ curves for daytime 1064 nm observations at MRC. As discussed, comparable internal gains are not available for detectors in the near-infrared. Furthermore, signal-to-noise issues become significant at 1064 nm. However, quantum efficiencies can be higher (20% to 40%). Operation at 1064 nm does have the additional inherent advantage of being well outside the range of human vision.

5.2 NRL LEO Array and Single Retroreflector Performance Comparison

To directly compare of performance between a single retroreflector and the NRL LEO array, we considered a specific pass with TOPEX/Poseidon orbital parameters as the test case. Note that a different midlatitude ground station is assumed. The links are predicted for a FTLRS (13-cm telescope aperture) located on Capraia. The major result from the standpoint of orbit sampling capability is apparent directly from the σ_{LRCS} plots shown in Figs. 24 and 25. The NRL LEO

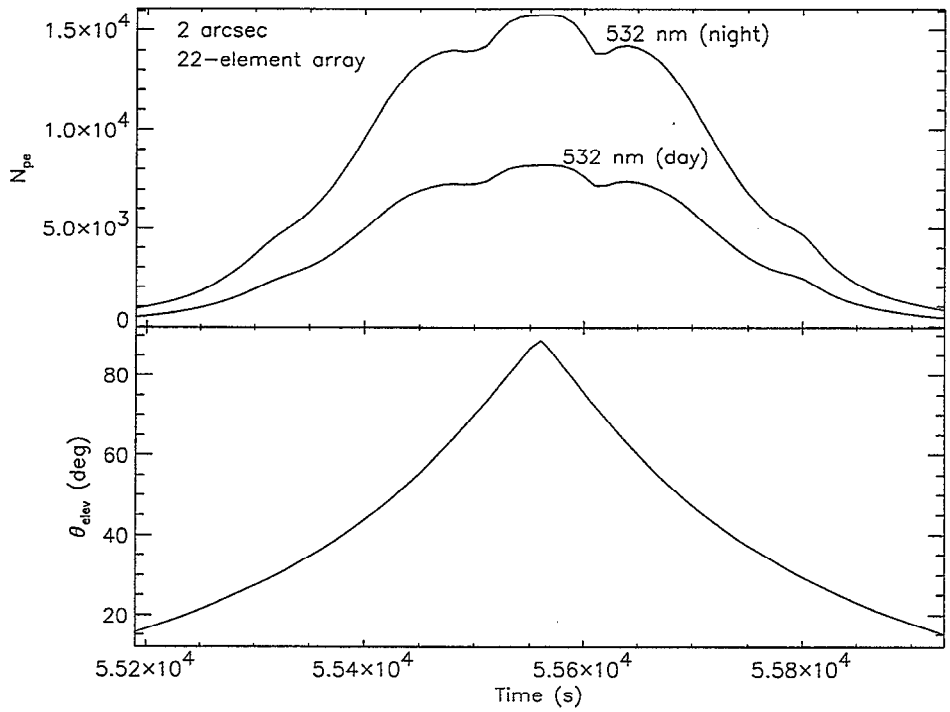

Fig. 20 - N_{pe} at 532 nm for a 100-cm diameter aperture telescope and the NRL LEO retroreflector array at MRC (top) and θ_{elev} (bottom) as a function of time during a near-zenith pass

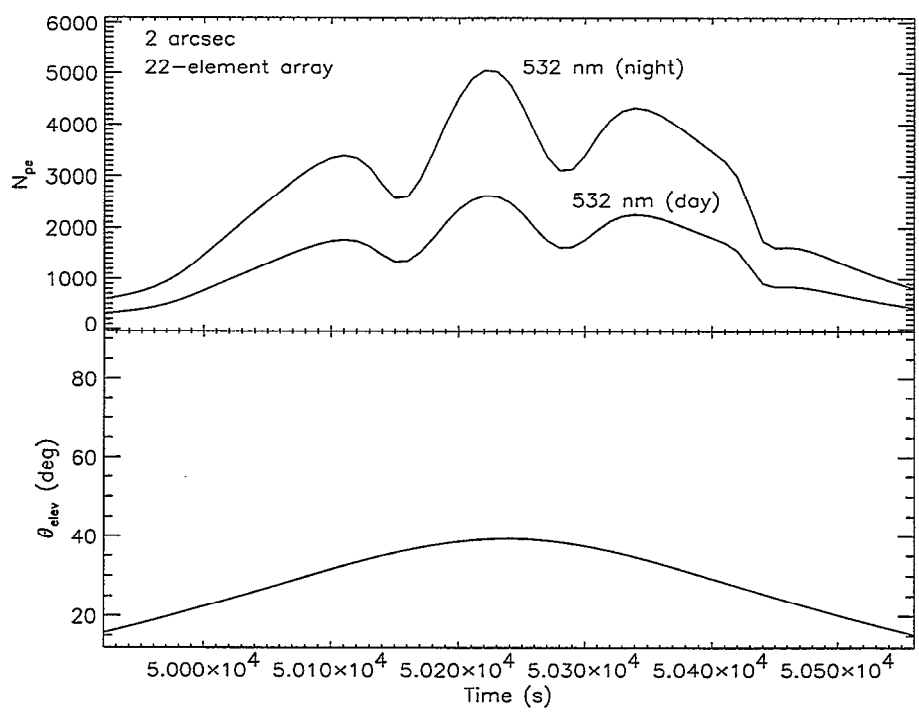

Fig. 21 - N_{pe} at 532 nm for a 100-cm diameter aperture telescope and the NRL LEO retroreflector array at MRC (top) and θ_{elev} (bottom) as a function of time during a low pass

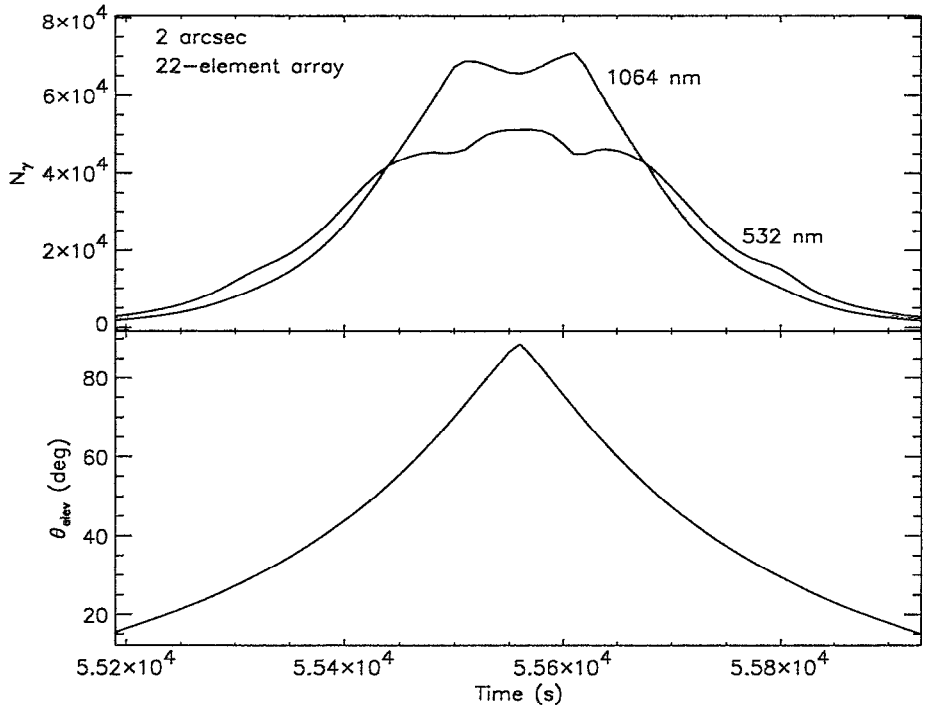

Fig. 22 - N_γ at 532 nm and 1064 nm for a 100-cm diameter aperture telescope and the NRL LEO retroreflector array at MRC (top) and θ_{elev} (bottom) as a function of time during a near-zenith pass

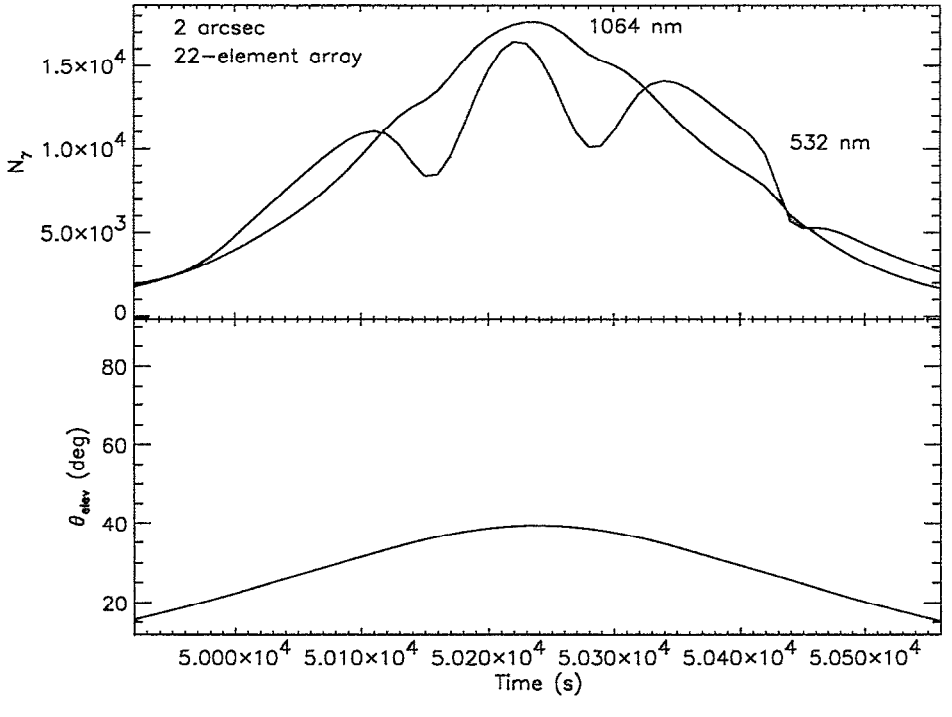

Fig. 23 - N_γ at 532 nm and 1064 nm for a 100-cm diameter aperture telescope and the NRL LEO retroreflector array at MRC (top) and θ_{elev} (bottom) as a function of time during a low pass

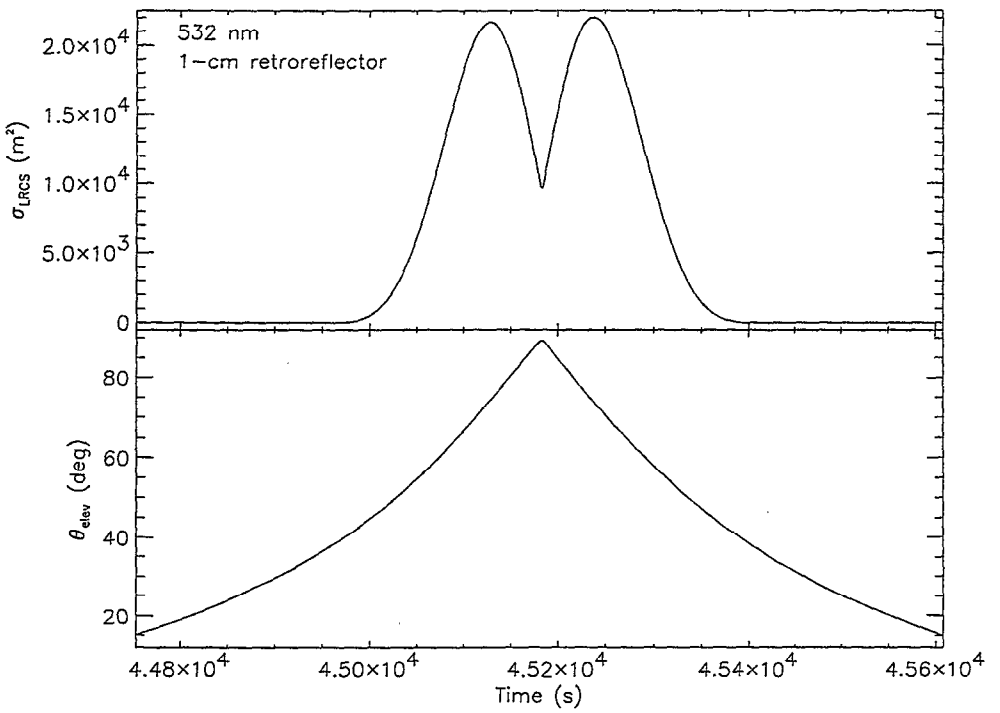

Fig. 24 - σ_{LRCS} at 532 nm for a 1-cm circular retroreflector (top) and θ_{elev} (bottom) as a function of time. For Pass 44 at PCA, $\theta_{elev} = 89.38°$ so this is effectively a zenith pass. Note the impact of retroreflector FOV on σ_{LRCS}

array prevents the drop-out in orbit sampling that occurs with the single retroreflector whenever its narrow FOV drives σ_{LRCS} to zero. For completeness, N_{pe} as function of time for a single 1-cm retroreflector with 0.008-in. bevels and the NRL LEO array are shown in Figs. 26 and 27. The performance is evaluated based on 5.4 arcsec pointing uncertainty and transmitter/receiver parameters described in Gilbreath et al. [9]. These results clearly show how the array closes the link throughout a pass by opening up the FOV well beyond the 57° window that constrains a single retroreflector.

5.3 Optical Phase Center and Timing Precision

The orbital estimation precision using the SLR data type is on the order of a ±1 cm rms. Therefore, knowledge of the offset of the retroreflector's location with respect to the spacecraft center of mass (COM) is important. This fixed offset is called the range correction and exists whether a single retroreflector or an array is used.

In the case of an array, the timing precision of the return signal can also be affected if more than one retroreflector is illuminated by a pulse. The placement of retroreflectors defines an optical phase center (OPC) as the common origin of all the retroreflector outward normals. To the extent the array retroreflectors lack a common OPC, a direction-dependent offset will be introduced into the system. Consequently, to achieve centimeter-level precision and accuracy, the retroreflectors in a multi-element array must be aligned with respect to a comparable tolerance to a common surface.

The OPC of the NRL LEO array is centered on the vertical axis 6 mm inside the array. Centered about this phase center is a surface of reflection. The advantage of a hemisphere of many

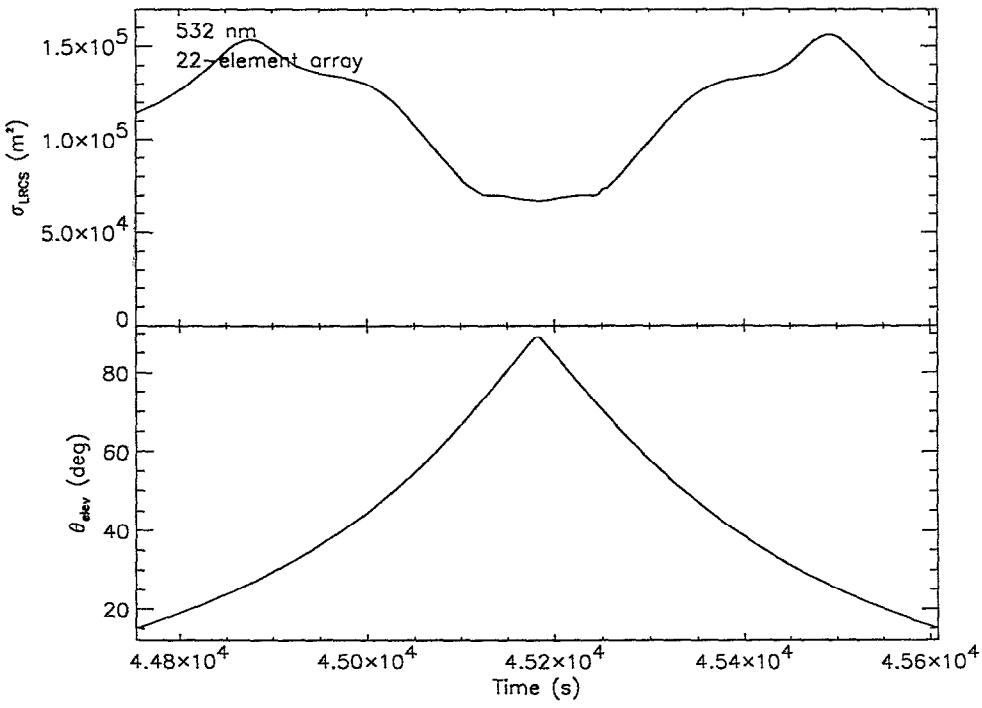

Fig. 25 - σ_{LRCS} at 532 nm for the NRL LEO retroreflector array (top) and θ_{elev} (bottom) as a function of time for Pass 44, at PCA, $\theta_{elev} = 89.38°$

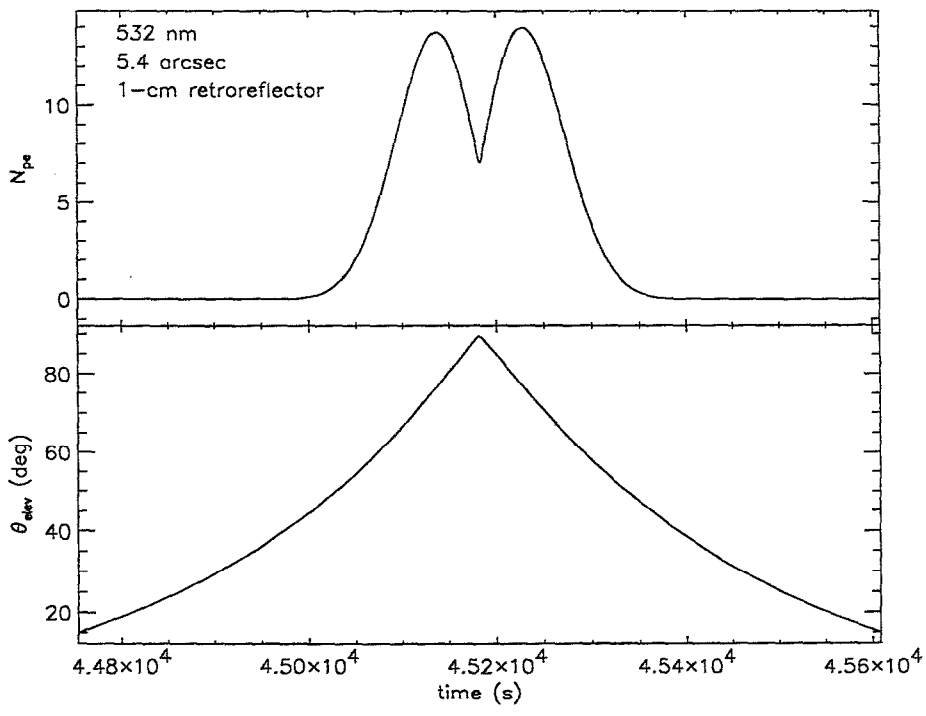

Fig. 26 - N_{pe} at 532 nm for a 13-cm diameter aperture FTLRS telescope and a 1-cm circular retroreflector at Capraia (top) and θ_{elev} (bottom) as a function of time during Pass 44; a 5.4 arcsec pointing precision is assumed

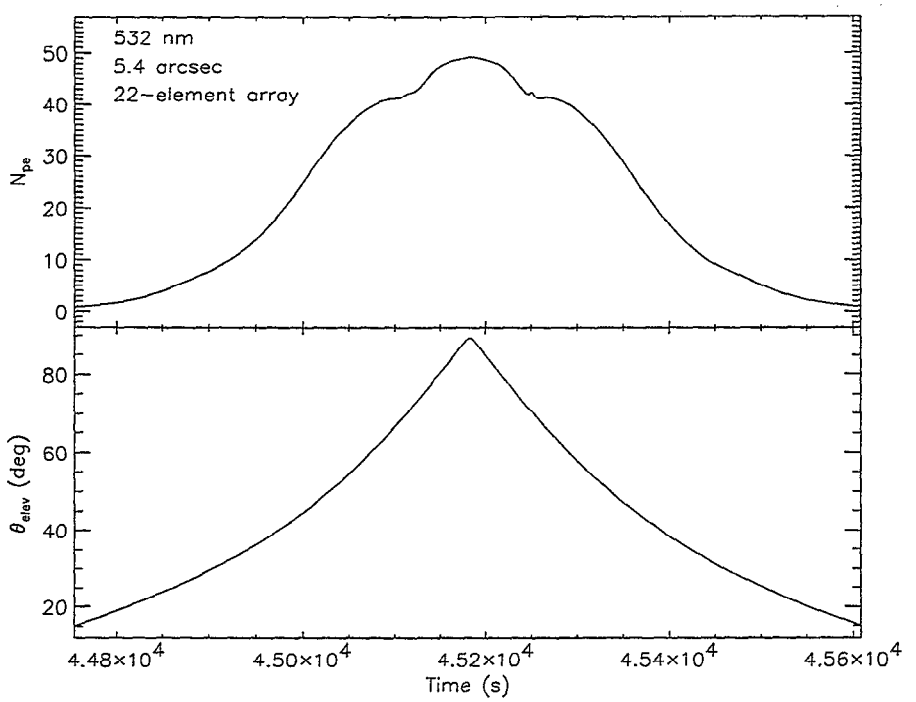

Fig. 27 - N_{pe} at 532 nm for a 13-cm diameter aperture FTLRS telescope and the NRL LEO retroreflector array at Capraia (top) and θ_{elev} (bottom) as a function of time during Pass 44; a 5.4 arcsec pointing precision is assumed

small reflectors is that for any incidence direction there is a retroreflector in close proximity. This condition allows a relatively smooth surface of reflection overall. The radius of this surface was determined by examining 585 angles and calculating the point on this surface for each angle. The surface can be approximated by a sphere with a radius of 2.505 cm. The standard deviation from this sphere is only 0.086 cm. This radius is the largest contributor to the range correction.

The range correction also must consider any pulse broadening due to the multiple retroreflectors. Using small retroreflectors allows for a very compact arrangement. The small size limits the possible pulse broadening. The broadening results from retroreflectors at different locations on the array having a delayed return. In the nadir direction, for example, the ring of 4 retroreflectors in the center is closer to the ground than is the middle ring of 8 retroreflectors. The time delay is 66 ps. The return from the middle ring is smaller because of the larger angle. Combining the returns from the two rings broadens the return pulse. The ring of 4 has an average σ_{LRCS} of $52,000$ m^2 and the ring of 8 has an average σ_{LRCS} of $16,000$ m^2, for nadir. Figure 28 shows the incoherent sum of the two sets of returns for an incident pulse with a full width at half maximum (FWHM) of 100 ps (typical for TLRS). The return pulse is broadened to 117 ps FWHM with a 7 ps (1 mm) delay in the peak amplitude. The extra 17 ps of width contributes to the range error. A 1-mm two way range correction is required to correct for pulse broadening. Longer pulses typical of the NRL@MRC system (250 ps) would have smaller effects.

The range correction error for the time of flight is the combination of the size of the sphere error and the pulse broadening. The increase in the total standard deviation error of the two is ± 0.86 mm and ± 2.6 mm. Using Gaussian statistics results in a total error of ± 2.74 mm. This analysis shows that the timing error of the array is within the ± 1 cm specification. A more accurate

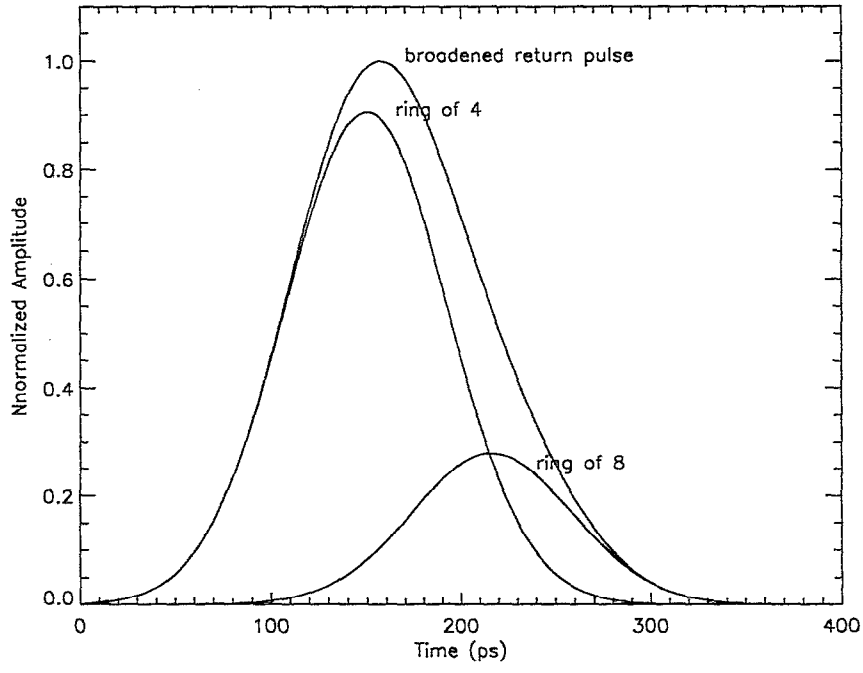

Fig. 28 - Array pulse timing effects

error analysis for millimeter-level range precision will require detailed information, including the nonlinear behavior of the receiver detector and electronics.

It should be noted that multiple retroreflectors interfere due to the coherence of the laser beam. This effect is termed *satellite scintillation.* An incoherent sum over the array's retroreflectors generates the average return signal, but a coherent sum is required for determining the standard deviation of the return signal. Having more than two retroreflectors in the FOV reduces the deviation. Since the location of each retroreflector at a given moment in time is not known, random phases are assigned to each retroreflector. This is equivalent to moving each retroreflector less than 1 μm. This was done analytically for the σ_{LRCS} at each point in the pass and was repeated for 100 random phases for each retroreflector. The resulting standard deviation of the σ_{LRCS} was less than 12% of the average return signal for all 855 samples of Pass 44 over Capraia (Fig. 29). This deviation is small compared to atmospheric scintillation [10].

5.4 Further Comparison of Single Retroreflectors and Retroreflector Arrays

Using an array eases the minimum pass geometry requirements significantly. As has been shown, an array can provide viable returns at much lower elevation angles. The quantitative improvement in available passes can be determined by sorting all pass geometries from the 10-day repeat cycle over ground stations in the Washington, D.C. area by θ_{elev} at PCA. Figure 30 shows the number of passes that exceed a given value of θ_{elev} at PCA as a function θ_{elev} for the repeat cycle. From Fig. 24, the single retroreflector σ_{LRCS} places lower limit of $\theta_{elev} > 40°$, assuming perfect atmospheric seeing. Scintillation and other effects will likely restrict sampling to $\theta_{elev} > 50°$. For an array, the additional tracking passes as low as the 20° FAA limit can used and, consequently, a better orbit solution becomes available.

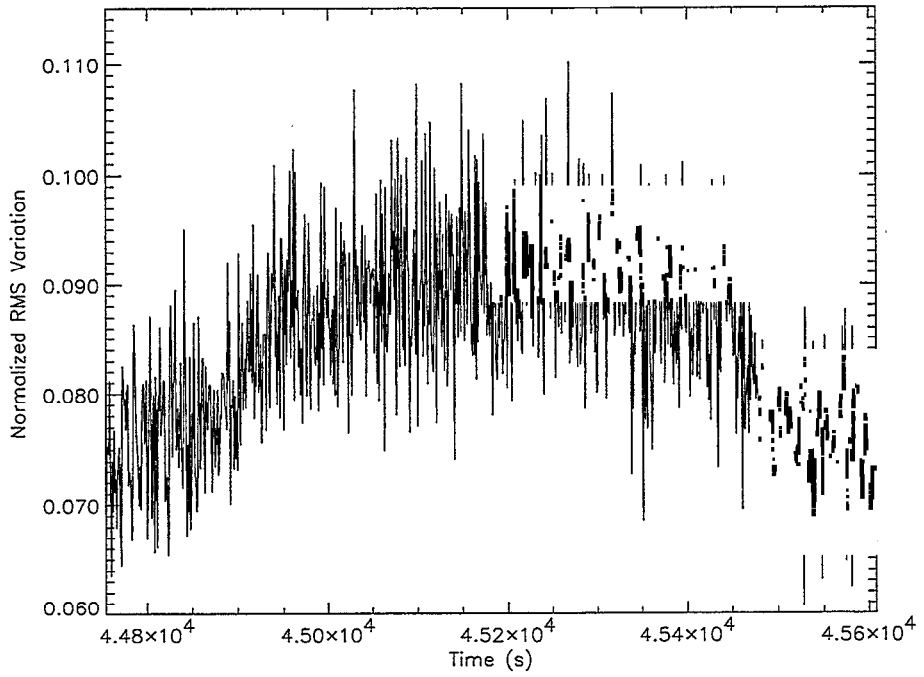

Fig. 29 - Normalized amplitude fluctuations of the NRL LEO array; rms variation in average return signal is 12%

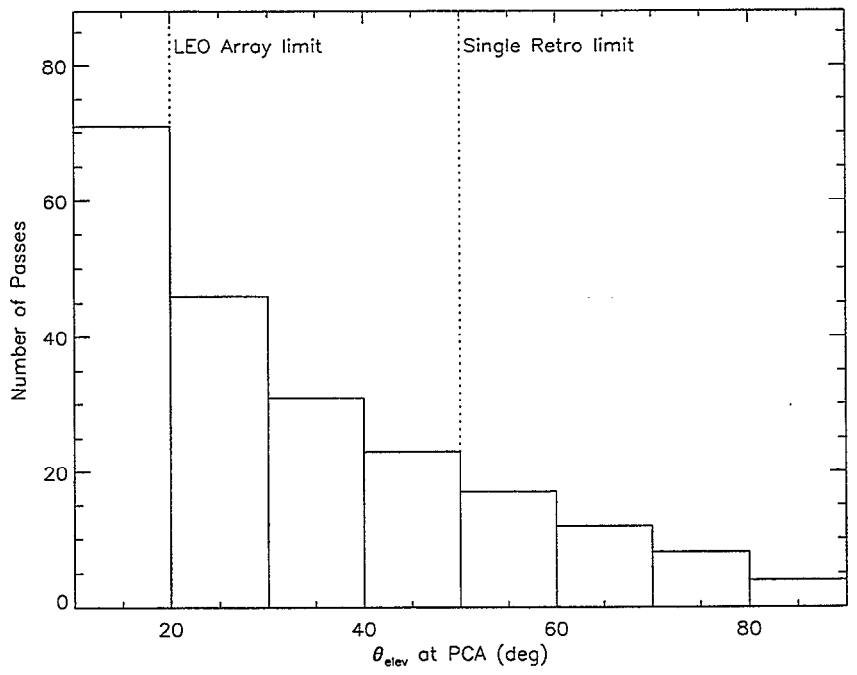

Fig. 30 - Number of passes vs elevation angle at PCA over a Washington, D.C. area ground station for a typical 1,100-km LEO orbit during a 10-day ground repeat track; dotted lines at 20° and 50° are conservative observation limits for the NRL LEO array and single 1-cm retroreflector respectively

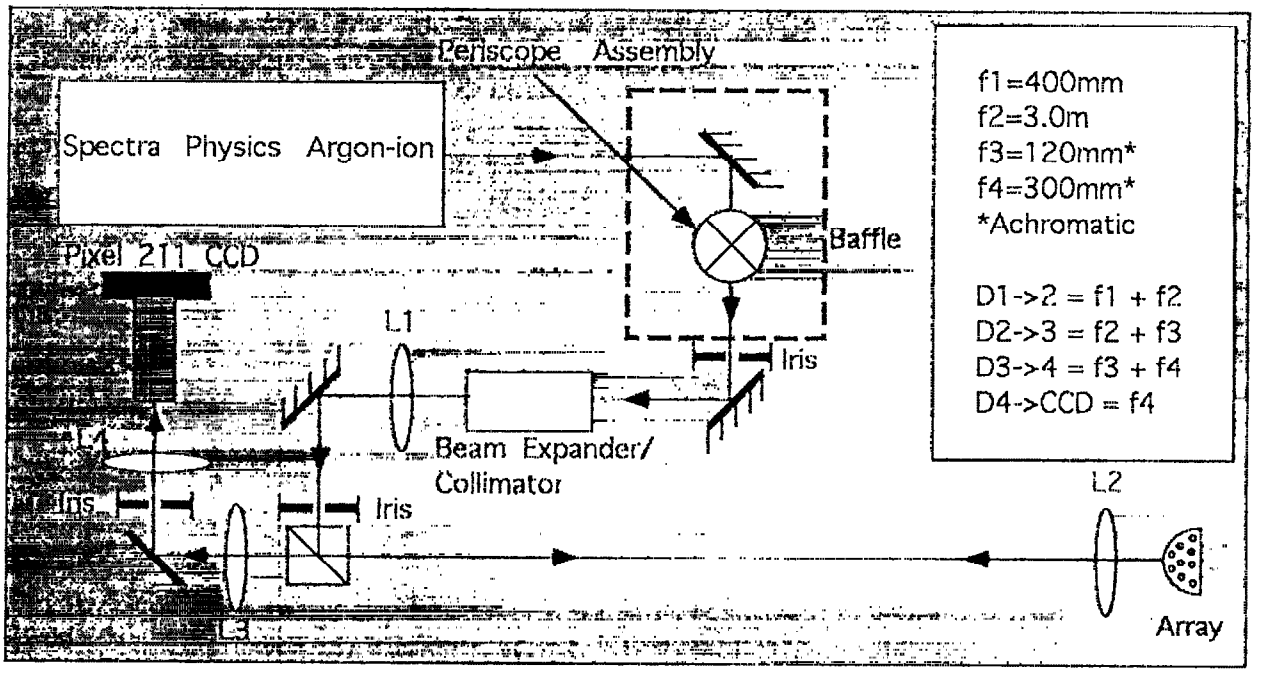

Fig. 31 - Optical bench layout for far-field characterization of the retroreflector array

6 EXPERIMENTAL DETERMINATION OF σ_{LRCS}

The NRL LEO retroreflector array's σ_{LRCS} was measured in the laboratory to validate the numerical computations. This subsection describes the experimental configuration and sensor calibration procedure. Then, the array's instantaneous intensity distribution is compared to the time-averaged distribution. Finally, differences between experimental and numerical results are discussed, with particular attention to the increased energy directed into sidelobes from retroreflector imperfections.

6.1 Procedure

The performance of the NRL LEO retroreflector array was experimentally characterized with a far-field test bed in the laboratory. Figure 31 shows the optical bench configuration. Light from an argon-ion laser at 514 nm was directed through partially baffled optics to present a collimated beam at the retroreflector array (RA). The returns from the RA were reflected back through the lens system, and the array's far-field intensity distribution was recorded by a Pixel 211 digitizing CCD camera as shown. The Pixel 211 has 12-bit sampling, a 192 × 165 format, and a 2.46 × 2.46 mm active area. As can be seen in Fig. 31, the Fourier plane of the array was located 3.0 m away from L2. This image plane was then magnified 2.5 times onto the CCD's active area by L3 and L4, which are achromatic lenses selected to reduce aberrations.

Three far-field intensity distributions were captured as digitized images with the CCD camera. Optimum exposure time was set to 5.25 s. The output from the laser was 85 mW and was attenuated using neutral density filters to prevent saturation of the CCD. The first FFDP data set was generated with a mask that exposed only one retroreflector in the 16° incidence angle ring. The

second and third data sets were obtained for the full RA instantaneous FFDP and time-averaged FFDP respectively.

6.2 Calibration

The CCD camera provided a digitized image of the FFDP. However, to relate the distribution from raw pixel values to angular position in μrad and σ_{LRCS} in m^2, the sensor has to be calibrated and conversion constants generated.

6.2.1 Spatial Calibration

For the spatial calibration, the optical layout shown in Fig. 31 was used with the retroreflector array replaced by a circular aperture followed by a flat mirror. A circular aperture/flat mirror combination observed at normal incidence has the same high symmetry geometry as a normal incidence single retroreflector, and the FFDP follows the Airy function form [Eq. (10)]. The known angular dependence of an Airy function served as the basis of the spatial calibration. With the mirror's normal aligned to the L2/L3 optical axis, an Airy pattern was projected onto the CCD. Images of the projected Airy pattern were recorded with the CCD for 12 apertures with radius from 7 to 18 mm in 1-mm steps. The weighted χ^2 difference between the observed intensity distribution on the CCD and an Airy intensity distribution, Eq. (10), was then determined as a function of the scaling parameter ξ along a radial slice across the image. The scaling parameter ξ converts the CCD pixel number to an angle. The minimum weighted χ^2 value then determines the best fit Airy pattern for a given aperture, and consequently, relates a pixel's number on the CCD x_i to angular position from

$$\xi x_i = r\frac{2\pi}{\lambda}\sin\theta \quad . \tag{18}$$

Based on this procedure, the resulting spatial scaling coefficient S is 0.156 μrad/μm, with a 5.6% standard deviation. S also has a detectable systematic variation with aperture size believed to be due the optical system's point spread function, which was measured to be $\sim$ 70 μm in width.

6.2.2 Radiometric Intensity Calibration

The CCD camera flat field correction and intensity calibration were determined by imaging an integrating sphere at several power levels. Light from the 514-nm laser was directed into an integrating sphere. A UDT S370 Optometer measured the power exiting a perpendicular port. The UDT was then replaced with the CCD camera, and an image was recorded. To assure stability of laser output, a second UDT monitored secondary scatter from one of the mirrors in the optical train leading to the integrating sphere. Initially, the laser light intensity was set so that the pixels in the CCD camera all read close to their maximum value but were not saturated. The light was then attenuated in steps to the UDT's detection range limit. Images and UDT readings of the sphere were recorded for 23 different attenuations.

For each of the CCD camera's 31,680 pixels, a linear least-squares fit yielded

$$\text{Pixel Value}(i,j) = g\left[i_d(i,j) + \mathcal{R}(i,j)(\text{UDT Reading})\right] \quad , \tag{19}$$

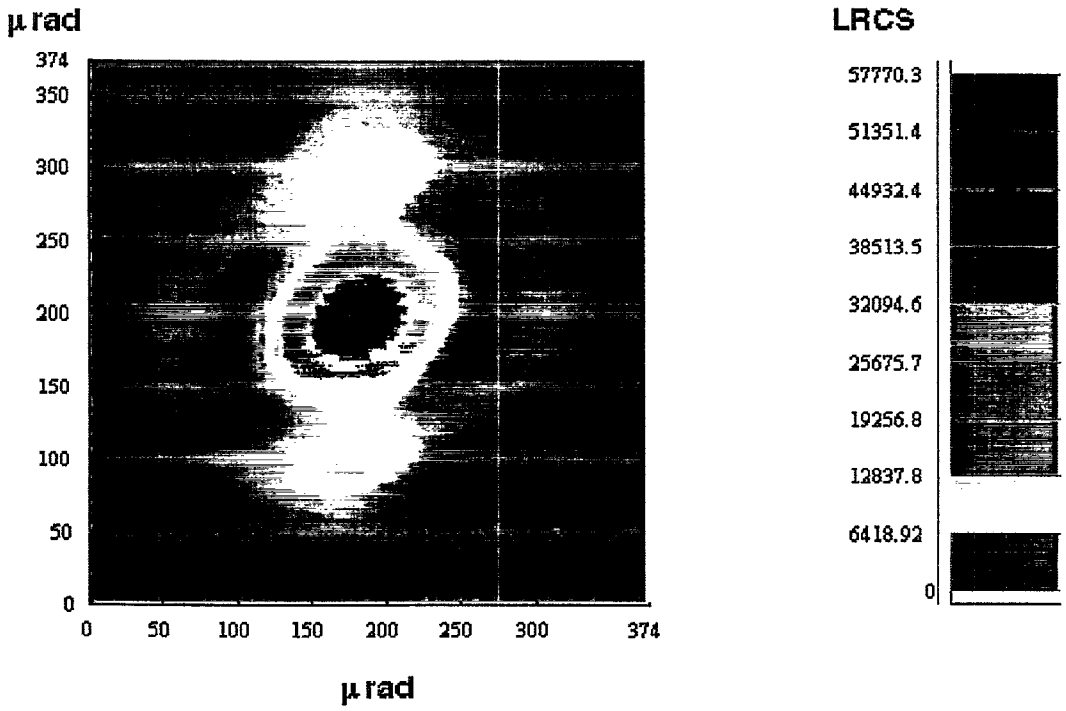

Fig. 32 - Experimental σ_{LRCS} for a single retroreflector at a 16° tilt from normal

where g is the analog to digital gain and $i_d(i,j)$ and $\mathcal{R}(i,j)$ are the dark current and responsivity of the i,j pixel, respectively. Equation (19) can be inverted to convert the raw 12-bit data into images with units of $\mathrm{W/cm^2}$.

The relation $\sigma_{\mathrm{LRCS}} = \frac{4\pi}{\lambda^2}A^2$ holds on the optical axis. This determines the coefficient C that scales the calibrated CCD output in $\mathrm{W/cm^2}$ to σ_{LRCS} in $\mathrm{m^2}$. The coefficient C has a mean value of 0.00056, with a standard deviation of 22% for six different aperture diameters.

6.3 Results and Comparison to Numerical Computation

The constants derived from the calibration and bit map conversion discussed above were used to plot the FFDP distributions (Figs. 32–34). In Fig. 32, the recorded far field distribution of the off-axis single retroreflector shows the expected Airy pattern elongated to some extent by the 16° tilt (see Figs. 7 and 9). Figure 33 is an instantaneous view of the entire array. The FFDP is highly structured as the result of interfering contributions from the array's multiple retroreflectors. Atmospheric turbulence and other effects cause time-averaging, hence, a "smoothing" of the pattern's distribution. Figure 34 shows a more realistic FFDP for the retroreflector in space when pulsed at repetition rates lower than the rate of change of the atmosphere. This figure shows the time-averaged FFDP of the array and corresponds to Eq. (17). This figure shows how the complex interference structure "washes out" and an averaged overall Airy-like distribution prevails.

Profile slices through the experimental and numerical values of σ_{LRCS} for a single retroreflector are compared in the top panel of Fig. 35. The model locates the first nulls at ± 79 μrad. When corrected for system effects, the experimentally measured separation between nulls is 166 μrad, which represents a 4.8% difference from the computed value. The difference between numerically

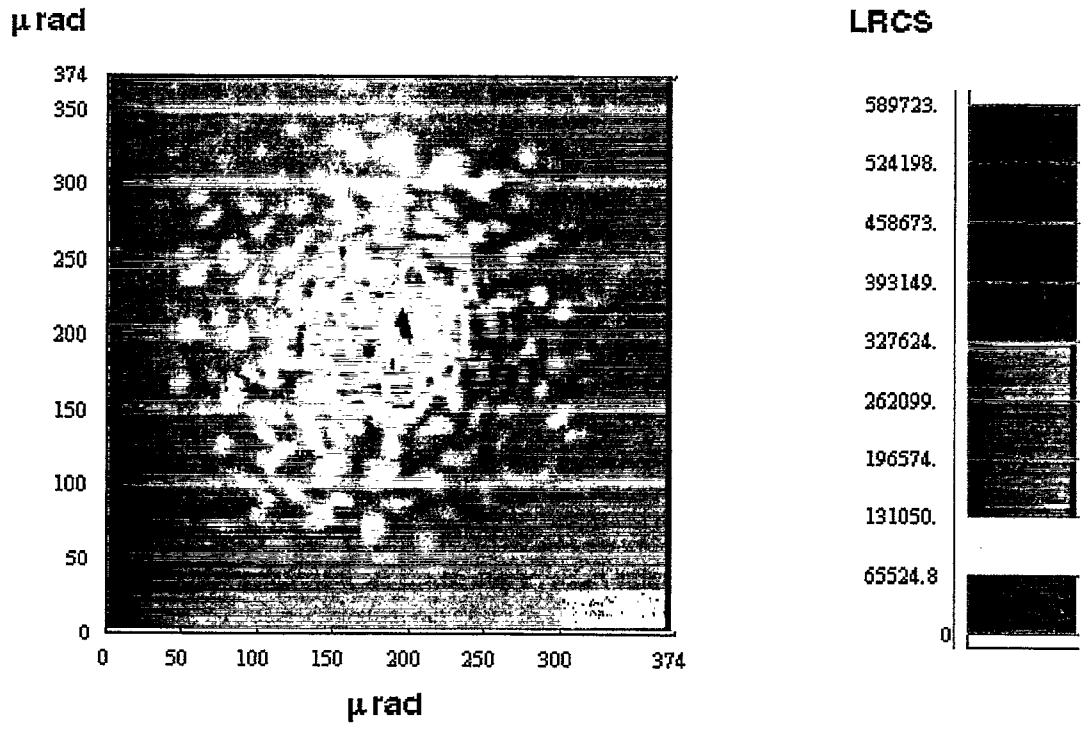

Fig. 33 - Instantaneous experimental σ_{LRCS} for the NRL LEO array at normal incidence

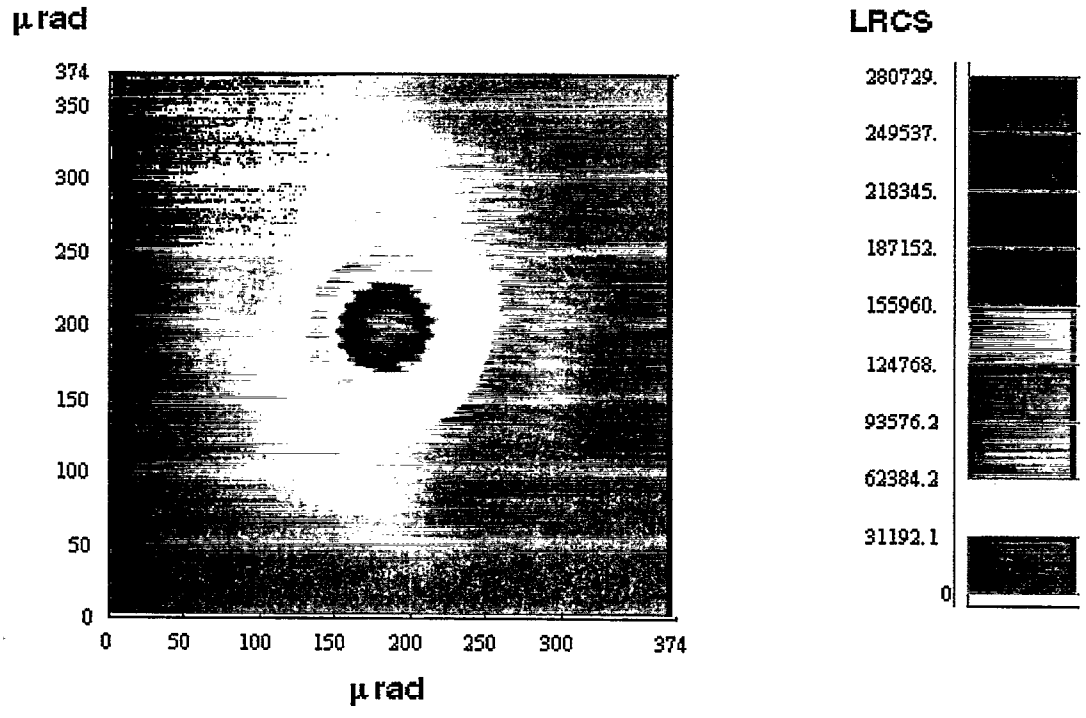

Fig. 34 - Time-averaged experimental σ_{LRCS} for the NRL LEO array at normal incidence (compare to Fig. 13)

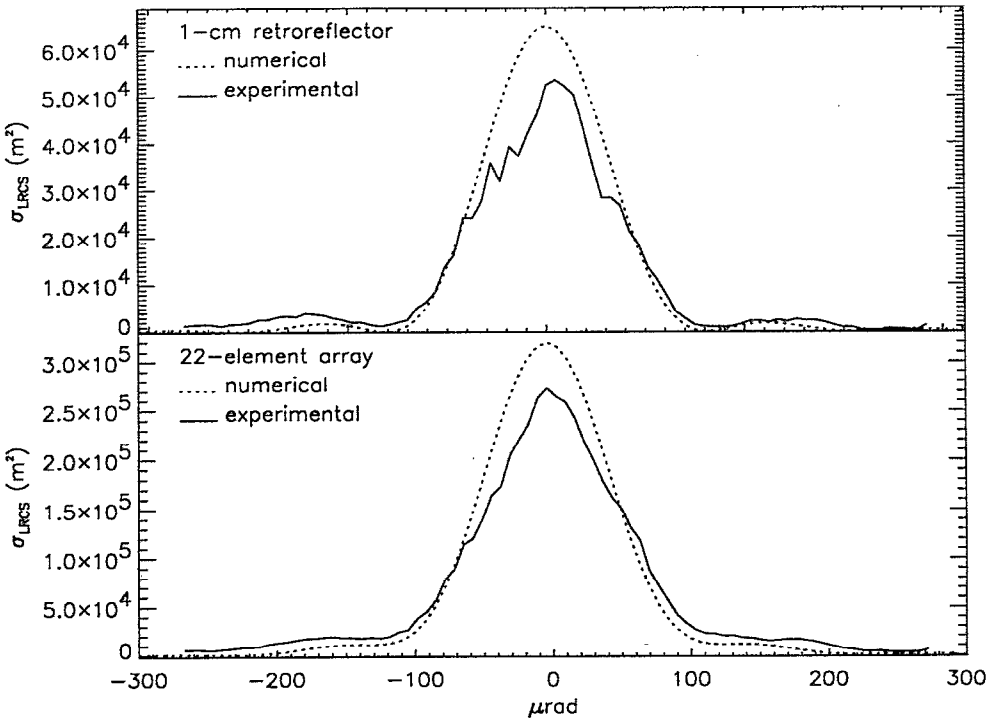

Fig. 35 - Experimental and numerical values of σ_{LRCS} for single retroreflector (top) at a 16° tilt and the NRL LEO array (bottom) at normal incidence

predicted and experimentally measured σ_{LRCS} was also determined. The model predicts 65078m^2 and the experimental σ_{LRCS} is 52384m^2. The experimental value at the peak is less than the numerical value by 21.6%.

For the array, the same trends in spread and magnitude of σ_{LRCS} occur. As seen in the bottom panel of Fig. 35, the time-averaged array has no clear minimum, but the width of the experimental central maximum is wider. Also, the experimental central maximum magnitude is lower than in the model. Furthermore, the wings of the experimental σ_{LRCS} profile are higher than the numerical prediction. The experimental maximum for the time-averaged array σ_{LRCS} is 272944 m^2 while the model's maximum is 319460 m^2. The difference is 15%. At 42 μrad off center, the experimental σ_{LRCS} again exceeds the numerical model. The measured σ_{LRCS} is 122749 m^2 and the model's σ_{LRCS} is 124719 m^2, with a difference of 1.6%.

In the context of operational SLR this deviation from predicted peak values actually helps. That is, the model calculation of σ_{LRCS} for a retroreflector does not include wave front distortion. It does, as noted, include the width of the beveled edges, the depth that the retroreflector is recessed into the array, and a scalar ρ for reflectivity losses. The effect of wave front distortions is to diffract light from the center maximum into relatively large angles. This enhanced diffraction manifests as a lower maximum with higher sidelobes. Wave front distortion has been intentionally included in the past for larger retroreflectors (e.g., 2.5 cm) and is commonly termed "spoiling." Due to the velocity aberration, the region from 39 to 49 μrad is of particular engineering significance. Here, the model is very close to the experimental values (Fig. 36).

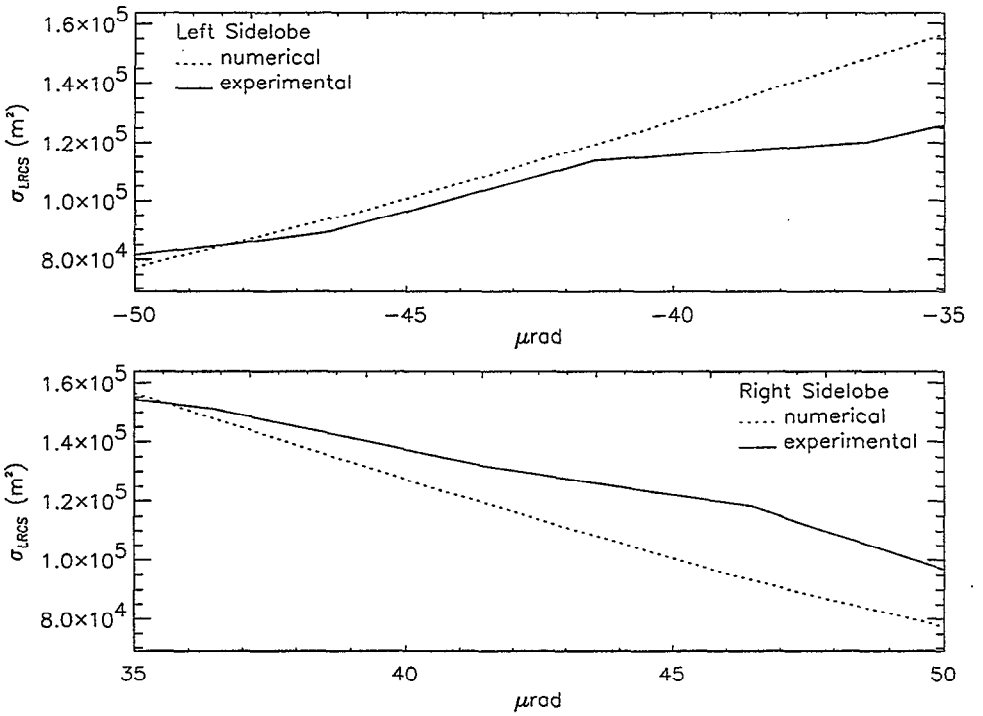

Fig. 36 - Time-averaged array experimental and numerical values of σ_{LRCS} for left wing (top) and right wing (bottom) of NRL LEO array at normal incidence

7 SPACE QUALIFICATION OF THE NRL LEO RETROREFLECTOR ARRAY

The NRL LEO retroreflector array was qualified for space flight with a number of tests. The qualification unit is identical to the flight articles except that the bevels do not satisfy the 0.004-in. specification on the retroreflectors. Because slight variations in retroreflector bevel size will have no effect on the mechanical properties of the array, substitution of retroreflectors will not alter the flight qualification. The flight-qualified retroreflectors were qualified separately by Zygo.

Data taken from the tests described below were analyzed. No thermal-related problems were detected, and no negative margins of safety for strength or fatigue were found. A more complete description of the qualification results can be found in Appendix C.

The unit weighs 7.82 oz (221 grams), including glass, mount assembly, and bolts for mounting.

7.1 Random Vibration Tests

To conduct the random vibration tests, the unit was mounted on an electrodynamic shaker. The axial and lateral axes were shaken independently. Each vibration was 2 min. in duration. The axial level was 13.92 G, rms. The lateral level was also 13.92 G, rms.

7.2 Thermal Vacuum Tests

The unit was mounted on a thermally controlled heat sink, and thermocouples were used to monitor and control temperature. The vacuum was less than 0.00001 torr. The unit was tested through 6 cycles from −100° C to +71° C.

7.3 Pyroshock Tests

The unit was mounted on an electrodynamic shaker and again the two axes where shocked independently in axial and lateral dimensions. The peak levels of shock were 6,000 Gs.

8 CONCLUSIONS

Based on the analysis and experimental verification presented in this report, we conclude that the NRL LEO retroreflector array will robustly close a link from a standard 1,100-km circular orbit using an SLR system comparable to NASA's TLRS above a 20° elevation angle for daytime and nighttime ranging. The array will also close a link for a system as modest as the FTLRS 13-cm aperture system in Caparia. In addition, when analyzed for the meter-class system to be installed at MRC in 2000, the link will be robust enough to support unambiguous ranging at even the lowest elevation angles, day and night, without the aid of an amplifier.

The array itself comprises 22 1-cm diameter retroreflectors situated on a hemisphere to produce a far field diffraction pattern that provides a laser radar cross section of greater than 10^4 m^2 for elevation angles above 20° with a 108° FOV. It has a mass of 221 grams and measures 82 mm in diameter by 43 mm in height.

Analysis was verified by bench experiments and showed that manufacturing defects in the wave front quality of the retroreflector direct energy to a small extent into sidelobes. It was shown that these enhanced sidelobes help the link by compensating for velocity aberration.

Results were compared to the predicted performance of a single cube. It was shown that the FOV would be severely restricted when using one cube, hence orbital sampling would be significantly reduced.

Predicted performance in the near-infrared at 1064 nm was also presented. Advantages of this wavelength include better transmission through the atmosphere and covertness due to transmission in the nonvisible region of the spectrum.

The array was space-qualified, and testing specifications are detailed in Appendix C.

ACKNOWLEDGMENTS

Mark Davis (NRL Code 8123/Allied Signal) provided the ephemeris and attitude data for all passes above the Washington, D.C. area. Data for the TOPEX/Poseidon passes over Capraia are the work of Jim Barnds (NRL Code 8233). We gratefully acknowledge both of their efforts in support of this report.

ACRONYMS

APD avalanche photodiode

COM center of mass

FAA Federal Aviation Administration

FFDP far field diffraction pattern

FOV field of view

FTLRS field-transportable laser radar station

FWHM full-width at half maximum

LEO low Earth orbit

LRCS laser radar cross section (or σ_{LRCS})

MOBLAS mobile laser ranging system

MRC Midway Research Center

NRL Naval Research Laboratory

OPC optical phase center

PCA point-of-closest approach

SLR satellite laser ranging

SOR Starfire Optical Range, Kirtland AFB, New Mexico

TLRS transportable laser ranging system

REFERENCES

[1] G.C. Gilbreath, P.W. Schumacher Jr., M.A. Davis, E.D. Lydick, and J.M. Anderson, "Calibrating the Naval Space Surveillance "Fence" Using Satellite Laser Ranging Data," *Proceedings of the 1997 AAS/AIAA Astrodynamics Specialist Conference* **97**, 1997.

[2] J.J. Degnan, "Millimeter Accuracy Satellite Laser Ranging A Review," *Contributions of Space Geodesy to Geodynamics Technology* **25**, 133–162 (1993).

[3] A.R. Peltzer, G.C. Gilbreath, G.E. Price, and W.J. Barnds, "Ephemeris Estimation of a Well-Defined Platform Using Satellite Laser Ranging from a Reduced Number of Ground Sites," NRL Report NRL/FR/8120–96-9800, April 1996.

[4] G.C. Gilbreath, M.A. Davis, P.B. Rolsma, R. Eichinger, T. Meehan, and J.M. Anderson, "Naval Research Laboratory at Starfire Optical Range: Satellite Laser Ranging with Robust Links," *SPIE Aerosense 97*, **SPIE 3065-51**, 1997.

[5] P.O. Minott, "Design of Retrodirector Arrays for Laser Ranging of Satellites," NASA TM-X-723-74-122, Goddard Space Flight Center, Greenbelt, Md., March 1974.

[6] P.O. Minott, "Measurement of the Lidar Cross Sections of Cube Corner Arrays for Laser Ranging of Satellites," NASA TM-X-722-74-301, Goddard Space Flight Center, Greenbelt, Md., September 1974.

[7] M. Born E. Wolf, *Principles of Optics*, 6th ed. (Pergamon Press, Oxford, 1985), pp. 395–398.

[8] J.W. Goodman, *Introduction to Fourier Optics*, 2nd ed. (McGraw-Hill, New York, 1996), pp. 63–78.

[9] G.C. Gilbreath, P.B. Rolsma, and R. Kessel, "Analysis of SLR Targets for JASON," NRL Memorandum Report 7971, August 1997.

[10] J.H. Churnside, "Turbulence Effects on the Geodynamics Laser Ranging System," NOAA Technical Memorandum ERL WPL-218, January 1992.

Appendix A

DIFFRACTION PATTERN AND PASS GEOMETRY CALCULATIONS

A.1 Circular Retroreflector Far Field Diffraction Patterns

A convenient method to develop the analytic basis for the numerical determination of far field diffraction patterns begins with the simplest case and then adds refinements. With this approach, numerical implementation of each stage can serve as a limiting test case for the next stage. Our starting case is normal incidence without bevel losses; we finish with tilted incidence with bevel losses. As has been noted in the body of this report, introducing a tilt in the incidence direction is a much larger effect than are the bevel losses.

A.1.1 Normal Incidence Without Bevel Losses

Consider a circular retroreflector with bevel loss regions directly overhead. The two-dimensional Fourier transform of the complex reflectance of the aperture, effectively the retroreflector's far field diffraction pattern $\tilde{A}(x,y)$ is given by

$$\tilde{a}(k_x,k_y) = \iint_{\text{aperture}} dxdy\tilde{A}(x,y)e^{-ik_x x}e^{-ik_y y} \quad . \tag{A1}$$

Using the function $c(x)=\sqrt{r^2-x^2}$, which defines the top half of the circular aperture, the double integral can be rewritten as

$$\begin{aligned}
\tilde{a}(k_x,k_y) &= \int_{-r}^{r} dx e^{-ik_x x}\int_{-c(x)}^{c(x)} e^{-ik_y y}dy & \text{(A2)}\\
&= \int_{-r}^{r} e^{-ik_x x}\frac{1}{-ik_y}\left[e^{-ik_y c(x)}-e^{ik_y c(x)}\right]dx \quad . & \text{(A3)}\\
&= \int_{-r}^{r} e^{-ik_x x}\frac{1}{ik_y}\left[e^{ik_y c(x)}-e^{-ik_y c(x)}\right]dx & \text{(A4)}\\
&= \frac{1}{k_y}\int_{-r}^{r} e^{-ik_x x}\left[\frac{1}{i}2i\sin k_y c(x)\right]dx & \text{(A5)}\\
&= \frac{2}{k_y}\int_{-r}^{r}\left[\cos k_x x - i\sin k_x x\right]\sin k_y c(x)dx & \text{(A6)}\\
&= \frac{2}{k_y}\int_{-r}^{r}\cos k_x x\sin\left(k_y\sqrt{r^2-x^2}\right)dx \\
&\quad -\frac{2i}{k_y}\int_{-r}^{r}\sin k_x x\sin\left(k_y\sqrt{r^2-x^2}\right)dx \quad . & \text{(A7)}
\end{aligned}$$

When Eq. (A7) is integrated numerically, the absolute magnitude of $\tilde{a}(k_x, k_y)$ determined, and then converted to a cross section, the result is the azimuthally symmetric Airy function of Fig. 6. (See Section B.1 for the numerical implementation of Eq. (A7).) The numerical routine that implements this geometry serves as a limit test case for the tilted and normal incidence with bevel losses routines.

A.1.2 Tilted Incidence Without Bevel Losses

When a circular retroreflector is tilted, the aperture changes shape to the overlap region of two offset circles. The tilt away from normal incidence can be related to the circles' offset x_0 from the center of the retroreflector. For a retroreflector of depth d with a face recessed by distance c and index of refraction n, the expression relating x_0 to the angle θ_{inci} between the surface normal and the incidence direction is

$$x_0 = c \sin \theta_{inci} + d \sin \theta_n \quad , \tag{A8}$$

where

$$\theta_n = \arcsin \left(\frac{\sin \theta_{inci}}{n} \right) \quad . \tag{A9}$$

For a circular retroreflector of radius r, $d = \sqrt{2}r$. The retroreflector's field of view (FOV) is limited by the requirement that $x_0 < r$. For a 1-cm diameter retroreflector with $n = 1.46$ and $c = 0.1016$ cm (or 0.040 in.), the FOV cut off is at $\theta_{inci} = 58.579°$. The aperture boundary for the tilted retroreflector is defined by $c(x) = \pm\sqrt{r^2 - (x - x_0)^2}$ for $x < 0$ and $c(x) = \pm\sqrt{r^2 - (x + x_0)^2}$ for $x \geq 0$. The aperture's shape is that of a cat's iris or an American football profile shown in the upper panel of Fig. 8.

Integrating each side of the aperture separately yields a two-dimensional Fourier transform for tilted incidence with four integrals given by

$$\begin{aligned} \tilde{a}(k_x, k_y) \;=\; & \frac{2}{k_y} \left[\int_{-(r-x_0)}^{0} \cos k_x x \sin \left(k_y \sqrt{r^2 - (x - x_0)^2} \right) dx \right. \\ & \left. + \int_{0}^{(r-x_0)} \cos k_x x \sin \left(k_y \sqrt{r^2 - (x + x_0)^2} \right) dx \right] \\ & - \frac{2i}{k_y} \left[\int_{-(r-x_0)}^{0} \sin k_x x \sin \left(k_y \sqrt{r^2 - (x - x_0)^2} \right) dx \right. \\ & \left. + \int_{0}^{(r-x_0)} \sin k_x x \sin \left(k_y \sqrt{r^2 - (x + x_0)^2} \right) dx \right] \quad . \end{aligned} \tag{A10}$$

Equation (A10) yields a reasonable transform and limits to an Airy function as $x_0 \to 0$. (See Section B.2 for the numerical implementation of Eq. (A10).) Figure 10 shows the sizable variation in the laser radar cross section of a tilted circular retroreflector as one sweeps k_x and k_y with a constant magnitude of k of 50 μrad (i.e., roughly a satellite's velocity aberration for a 1,100-km high orbit).

A.1.3 Normal Incidence With Bevel Losses

Consider a circular retroreflector with bevel loss regions directly overhead. There are six regions, symmetric about the x-axis, that can be used to compute the two-dimensional Fourier transform for the aperture. These regions are shown in Fig. A1.

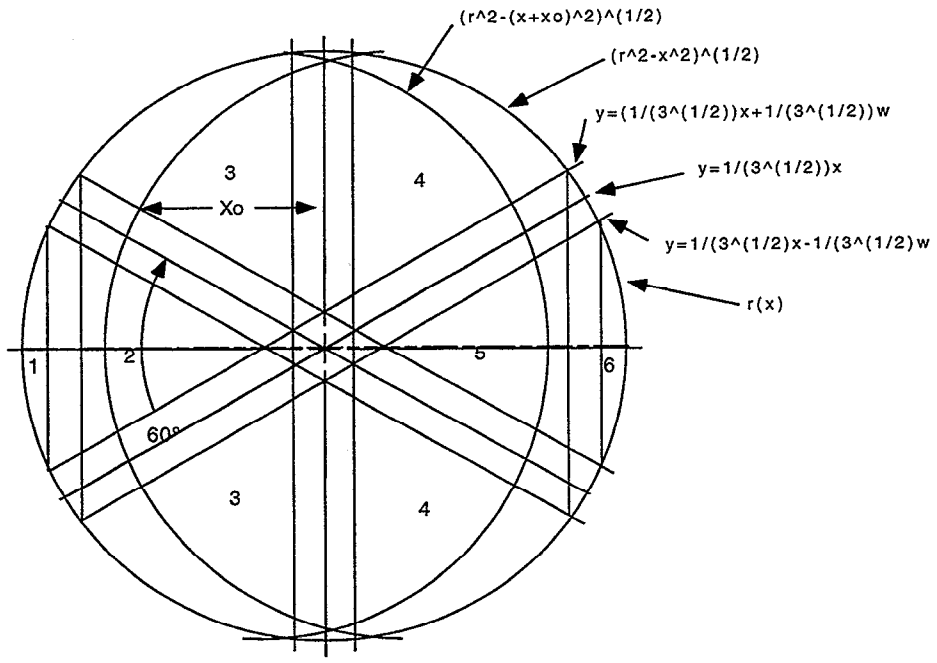

Fig. A1 - On-axis retroreflector with bevel geometry (the six regions are numbered left to right; regions 3 and 4 are each made of two pieces)

The two-dimensional Fourier transform of the complex reflectance of the aperture $\tilde{A}(x,y)$ is now given by

$$\begin{aligned}
\tilde{a}(k_x,k_y) = & \\
& \int_{-r}^{-x_2} dx e^{-ik_x x} \int_{-c(x)}^{c(x)} e^{-ik_y y} dy + \int_{-x_2}^{-w} dx e^{-ik_x x} \int_{l^+(x)}^{-l^+(x)} e^{-ik_y y} dy \\
& + \int_{-x_1}^{-w/2} dx e^{-ik_x x} \left[\int_{-c(x)}^{l^-(x)} e^{-ik_y y} dy + \int_{-l^-(x)}^{c(x)} e^{-ik_y y} dy \right] \\
& + \int_{w/2}^{x_1} dx e^{-ik_x x} \left[\int_{-c(x)}^{-l^+(x)} e^{-ik_y y} dy + \int_{l^+(x)}^{c(x)} e^{-ik_y y} dy \right] \\
& + \int_{w}^{x_2} dx e^{-ik_x x} \int_{-l^-(x)}^{l^-(x)} e^{-ik_y y} dy + \int_{x_2}^{r} dx e^{-ik_x x} \int_{-c(x)}^{c(x)} e^{-ik_y y} dy \quad ,
\end{aligned} \tag{A11}$$

where

$$l^+(x) = \frac{1}{\sqrt{3}}(x+w) \tag{A12}$$

and

$$l^-(x) = \frac{1}{\sqrt{3}}(x-w) \quad . \tag{A13}$$

The two integration limits along x determined by the intersection of $l^+(x)$ and $l^-(x)$ and the circular aperture are given by $x_1 = \frac{1}{4}\left(-w + \sqrt{12r^2 - 3w^2}\right)$ and $x_2 = \frac{1}{4}\left(w + \sqrt{12r^2 - 3w^2}\right)$, respectively.

Rather than working with all six terms in Eq. (A11) at once, the forms are reduced to be convenient for numerical integration individually. The six terms are:

$$\tilde{a}_1(k_x,k_y) = \int_{-r}^{-x_2} dx e^{-ik_x x} \int_{-c(x)}^{c(x)} e^{-ik_y y} dy \quad , \tag{A14}$$

$$\tilde{a}_2(k_x,k_y) = \int_{-x_2}^{-w} dx e^{-ik_x x} \int_{l^+(x)}^{-l^+(x)} e^{-ik_y y} dy \quad , \tag{A15}$$

$$\tilde{a}_3(k_x,k_y) = \int_{-x_1}^{-w/2} dx e^{-ik_x x} \left[\int_{-c(x)}^{l^-(x)} e^{-ik_y y} dy + \int_{-l^-(x)}^{c(x)} e^{-ik_y y} dy \right] \quad , \tag{A16}$$

$$\tilde{a}_4(k_x,k_y) = \int_{w/2}^{x_1} dx e^{-ik_x x} \left[\int_{-c(x)}^{-l^+(x)} e^{-ik_y y} dy + \int_{l^+(x)}^{c(x)} e^{-ik_y y} dy \right] \quad , \tag{A17}$$

$$\tilde{a}_5(k_x,k_y) = \int_{w}^{x_2} dx e^{-ik_x x} \int_{-l^-(x)}^{l^-(x)} e^{-ik_y y} dy \quad , \tag{A18}$$

and

$$\tilde{a}_6(k_x,k_y) = \int_{x_2}^{r} dx e^{-ik_x x} \int_{-c(x)}^{c(x)} e^{-ik_y y} dy \quad . \tag{A19}$$

Both $\tilde{a}_1(k_x,k_y)$ and $\tilde{a}_6(k_x,k_y)$ have upper and lower limits defined by the circular aperture, as in Eq. (A2) for the integration along y. Hence, these two terms can be immediately simplified to the same form as Eq. (A7), yielding

$$\begin{aligned} \tilde{a}_1(k_x,k_y) &= \frac{2}{k_y} \int_{-r}^{-x_2} \cos k_x x \sin\left(k_y \sqrt{r^2 - x^2}\right) dx \\ &\quad - \frac{2i}{k_y} \int_{-r}^{-x_2} \sin k_x x \sin\left(k_y \sqrt{r^2 - x^2}\right) dx \quad , \end{aligned} \tag{A20}$$

and

$$\begin{aligned} \tilde{a}_6(k_x,k_y) &= \frac{2}{k_y} \int_{x_2}^{r} \cos k_x x \sin\left(k_y \sqrt{r^2 - x^2}\right) dx \\ &\quad - \frac{2i}{k_y} \int_{x_2}^{r} \sin k_x x \sin\left(k_y \sqrt{r^2 - x^2}\right) dx \quad . \end{aligned} \tag{A21}$$

Note, of course, that the x integration limits in Eqs. (A20) and (A21) are different than those in Eq. (A7). Similarly, $\tilde{a}_2(k_x,k_y)$ and $\tilde{a}_5(k_x,k_y)$ can be reduced to integrals over x of the form

$$\begin{aligned} \tilde{a}_2(k_x,k_y) &= -\frac{2}{k_y} \int_{-x_2}^{-w} \cos k_x x \sin\left(k_y \frac{1}{\sqrt{3}}(x+w)\right) dx \\ &\quad + \frac{2i}{k_y} \int_{-x_2}^{-w} \sin k_x x \sin\left(k_y \frac{1}{\sqrt{3}}(x+w)\right) dx \quad , \end{aligned} \tag{A22}$$

and

$$\begin{aligned} \tilde{a}_5(k_x,k_y) &= \frac{2}{k_y} \int_{w}^{x_2} \cos k_x x \sin\left(k_y \frac{1}{\sqrt{3}}(x-w)\right) dx \\ &\quad - \frac{2i}{k_y} \int_{w}^{x_2} \sin k_x x \sin\left(k_y \frac{1}{\sqrt{3}}(x-w)\right) dx \quad . \end{aligned} \tag{A23}$$

Note the sign change of the real and imaginary parts of Eq. (A22).

Simplifying $\tilde{a}_3(k_x, k_y)$ and $\tilde{a}_4(k_x, k_y)$ can be done with the same approach. For $\tilde{a}_4(k_x, k_y)$,

$$\tilde{a}_4(k_x, k_y) =$$

$$\int_{w/2}^{x_1} dx e^{-ik_x x} \left[\int_{-c(x)}^{-l^+(x)} e^{-ik_y y} dy + \int_{l^+(x)}^{c(x)} e^{-ik_y y} dy \right] \tag{A24}$$

$$= \int_{w/2}^{x_1} e^{-ik_x x} \frac{1}{-ik_y} \left[e^{ik_y l^+(x)} - e^{ik_y c(x)} + e^{-ik_y c(x)} - e^{-ik_y l^+(x)} \right] dx \tag{A25}$$

$$= \int_{w/2}^{x_1} e^{-ik_x x} \frac{1}{ik_y} \left[e^{ik_y c(x)} - e^{-ik_y c(x)} - e^{ik_y l^+(x)} + e^{-ik_y l^+(x)} \right] dx \tag{A26}$$

$$= \frac{1}{k_y} \int_{w/2}^{x_1} e^{-ik_x x} \left[\frac{1}{i} 2i \sin k_y c(x) - \frac{1}{i} 2i \sin k_y l^+(x) \right] dx \tag{A27}$$

$$= \frac{2}{k_y} \int_{w/2}^{x_1} [\cos k_x x - i \sin k_x x] \sin k_y c(x) dx$$

$$- \frac{2}{k_y} \int_{w/2}^{x_1} [\cos k_x x - i \sin k_x x] \sin k_y l^+(x) dx \tag{A28}$$

$$= \frac{2}{k_y} \left\{ \int_{w/2}^{x_1} \cos k_x x \sin \left(k_y \sqrt{r^2 - x^2} \right) dx \right.$$

$$\left. - \int_{w/2}^{x_1} \cos k_x x \sin \left(k_y \frac{1}{\sqrt{3}} (x + w) \right) dx \right\}$$

$$- \frac{2i}{k_y} \left\{ \int_{w/2}^{x_1} \sin k_x x \sin \left(k_y \sqrt{r^2 - x^2} \right) dx \right.$$

$$\left. - \int_{w/2}^{x_1} \sin k_x x \sin \left(k_y \frac{1}{\sqrt{3}} (x + w) \right) dx \right\} \quad . \tag{A29}$$

Finally, repeating these steps for $\tilde{a}_3(k_x, k_y)$ yields the similar form

$$\tilde{a}_3(k_x, k_y) = \int_{-x_1}^{-w/2} dx e^{-ik_x x} \left[\int_{-c(x)}^{l^-(x)} e^{-ik_y y} dy + \int_{-l^-(x)}^{c(x)} e^{-ik_y y} dy \right] \tag{A30}$$

$$= \frac{2}{k_y} \left\{ \int_{-x_1}^{-w/2} \cos k_x x \sin \left(k_y \sqrt{r^2 - x^2} \right) dx \right.$$

$$\left. + \int_{-x_1}^{-w/2} \cos k_x x \sin \left(k_y \frac{1}{\sqrt{3}} (x - w) \right) dx \right\}$$

$$- \frac{2i}{k_y} \left\{ \int_{-x_1}^{-w/2} \sin k_x x \sin \left(k_y \sqrt{r^2 - x^2} \right) dx \right.$$

$$\left. + \int_{-x_1}^{-w/2} \sin k_x x \sin \left(k_y \frac{1}{\sqrt{3}} (x - w) \right) dx \right\} \quad . \tag{A31}$$

The integrals in Eqs. (A20), (A21), (A22), (A23), (A29), and (A31) are to be evaluated numerically. Figure 12 shows the variation in the σ_{LRCS} of a beveled circular retroreflector as one sweeps

k_x and k_y with a constant magnitude of k of 50 μrad (i.e., roughly a satellite's velocity aberration). In comparison to the variation seen in Fig. 10, the bevels do not cause that much change in the magnitude, but they do introduce a six-fold symmetry.

A.1.4 Tilted Incidence With Bevel Losses

For a circular retroreflector with bevel loss regions, off-normal incidence angles tilted about the y-axis result in an aperture that is a combination of the cat's eye boundary and bevel loss regions. The position of the bevel loss regions is unchanged, and Eq. (A8) gives the correct offset in this case as well. Note that the FOV limit now becomes $x_0 < r - \frac{w}{2}$. For a 1-cm diameter retroreflector with $n = 1.46$, $c = 0.1016$ cm (or 0.040 in.), and $w = 0.01016$ cm (or 0.004 in.), the FOV cut off is at $\theta_{inci} = 57.63865°$. Because the normal incidence case with bevel losses required distinct integration regions on each side of the aperture, the same six regions used for Eq. (A11) can also be used in this case. The two integration limits along x determined by the intersection of $l^+(x)$ and $l^-(x)$ and the aperture change to $x_1 = \frac{3}{4}\left\{-\left(\frac{1}{3}w + x_0\right) + \sqrt{\frac{4}{3}r^2 - \frac{1}{3}(w - x_0)^2}\right\}$ and $x_2 = \frac{3}{4}\left\{\left(\frac{1}{3}w - x_0\right) + \sqrt{\frac{4}{3}r^2 - \frac{1}{3}(w + x_0)^2}\right\}$, respectively. The two-dimensional Fourier transform for tilted incidence can be expressed in an analogous form to Eq. (A11), where the resulting six terms are given by:

$$\begin{aligned}
\tilde{a}_1(k_x, k_y) &= \frac{2}{k_y}\int_{-(r-x_0)}^{-x_2} \cos k_x x \sin\left(k_y\sqrt{r^2 - (x - x_0)^2}\right) dx \\
&\quad - \frac{2i}{k_y}\int_{-(r-x_0)}^{-x_2} \sin k_x x \sin\left(k_y\sqrt{r^2 - (x - x_0)^2}\right) dx \quad , \qquad \text{(A32)}
\end{aligned}$$

$$\begin{aligned}
\tilde{a}_2(k_x, k_y) &= -\frac{2}{k_y}\int_{-x_2}^{-w} \cos k_x x \sin\left(k_y\frac{1}{\sqrt{3}}(x + w)\right) dx \\
&\quad + \frac{2i}{k_y}\int_{-x_2}^{-w} \sin k_x x \sin\left(k_y\frac{1}{\sqrt{3}}(x + w)\right) dx \quad , \qquad \text{(A33)}
\end{aligned}$$

$$\begin{aligned}
\tilde{a}_3(k_x, k_y) &= \frac{2}{k_y}\left\{\int_{-x_1}^{-w/2} \cos k_x x \sin\left(k_y\sqrt{r^2 - (x - x_0)^2}\right) dx\right. \\
&\quad \left. + \int_{-x_1}^{-w/2} \cos k_x x \sin\left(k_y\frac{1}{\sqrt{3}}(x - w)\right) dx\right\} \\
&\quad - \frac{2i}{k_y}\left\{\int_{-x_1}^{-w/2} \sin k_x x \sin\left(k_y\sqrt{r^2 - (x - x_0)^2}\right) dx\right. \\
&\quad \left. + \int_{-x_1}^{-w/2} \sin k_x x \sin\left(k_y\frac{1}{\sqrt{3}}(x - w)\right) dx\right\} \quad , \qquad \text{(A34)}
\end{aligned}$$

$$\begin{aligned}
\tilde{a}_4(k_x, k_y) &= \frac{2}{k_y}\left\{\int_{w/2}^{x_1} \cos k_x x \sin\left(k_y\sqrt{r^2 - (x + x_0)^2}\right) dx\right. \\
&\quad \left. - \int_{w/2}^{x_1} \cos k_x x \sin\left(k_y\frac{1}{\sqrt{3}}(x + w)\right) dx\right\} \\
&\quad - \frac{2i}{k_y}\left\{\int_{w/2}^{x_1} \sin k_x x \sin\left(k_y\sqrt{r^2 - (x + x_0)^2}\right) dx\right.
\end{aligned}$$

$$- \int_{w/2}^{x_1} \sin k_x x \sin\left(k_y \frac{1}{\sqrt{3}}(x+w)\right) dx \Bigg\} \quad , \tag{A35}$$

$$\tilde{a}_5(k_x, k_y) = \frac{2}{k_y} \int_{w}^{x_2} \cos k_x x \sin\left(k_y \frac{1}{\sqrt{3}}(x-w)\right) dx$$
$$- \frac{2i}{k_y} \int_{w}^{x_2} \sin k_x x \sin\left(k_y \frac{1}{\sqrt{3}}(x-w)\right) dx \quad , \tag{A36}$$

and

$$\tilde{a}_6(k_x, k_y) = \frac{2}{k_y} \int_{x_2}^{(r-x_0)} \cos k_x x \sin\left(k_y \sqrt{r^2 - (x+x_0)^2}\right) dx$$
$$- \frac{2i}{k_y} \int_{x_2}^{(r-x_0)} \sin k_x x \sin\left(k_y \sqrt{r^2 - (x+x_0)^2}\right) dx \quad . \tag{A37}$$

Equations (A32) to (A37) limit properly to the untilted case as $x_0 \to 0$. See Section B.3 for the numerical implementation of Eqs. (A32) to (A37).

A.2 Converting Pass Geometry to $k_x k_y$ Space

At a given instant, the orientation and velocity of the satellite with respect to the ground station determines the effective aperture of the retroreflector and the velocity aberration respectively.

For simplicity, consider a nadir-pointing retroreflector and use a fixed-Earth coordinate system. Hence, the ground station's location vector is a constant denoted by $\vec{\mathbf{G}}$, with fixed spherical coordinates of G, θ_{gs}, and ϕ_{gs}. Note that θ_{gs} is the ground station's colatitude measured down from the north pole rather than the latitude from the equator. The satellite's position is denoted by $\vec{\mathbf{S}}$, with spherical coordinates of S, $\theta_{s/c}$, and $\phi_{s/c}$. The satellite velocity v includes the effect of ground station motion. Finally, the range vector between satellite and ground station is $\vec{\mathbf{R}} = \vec{\mathbf{S}} - \vec{\mathbf{G}}$. Figure A2 illustrates the geometry and the local coordinate system at the satellite.

The angle of incidence θ_{inci}, which defines the aperture through Eq. (A8), is the angle between $\vec{\mathbf{S}}$ and $\vec{\mathbf{R}}$. Since $\vec{\mathbf{G}}$, $\vec{\mathbf{S}}$, and $\vec{\mathbf{R}}$ form a triangle, θ_{inci} can be related to the angular coordinates of $\vec{\mathbf{G}}$ and $\vec{\mathbf{S}}$ and the elevation angle θ_{elev} of the satellite at the ground site. The angle between $\vec{\mathbf{G}}$ and $\vec{\mathbf{S}}$ is given by

$$\cos\gamma = \cos\theta_{s/c}\cos\theta_{gs} + \sin\theta_{s/c}\sin\theta_{gs}\cos(\phi_{s/c} - \phi_{gs}) \quad . \tag{A38}$$

Hence,

$$\theta_{elev} + \frac{\pi}{2} + \gamma + \theta_{inci} = \pi \tag{A39}$$

or

$$\theta_{elev} + \gamma + \theta_{inci} = \frac{\pi}{2} \quad . \tag{A40}$$

In practice, the values of θ_{inci} and θ_{elev} as a function of time during the pass are computed directly by orbital dynamics software. When working with a retroreflector array, θ_{inci} is the angle between $\vec{\mathbf{R}}$ and the array's axis. Hence, one must do a little further computation to determine the angle of incidence for each retroreflector with respect to $\vec{\mathbf{R}}$.

The apparent velocity of the retroreflector can be expressed in terms of velocity, ground station position, and satellite position. Once the velocity components in a satellite local coordinate system are determined, the values of k_x and k_y that define the ground stations position in the far field

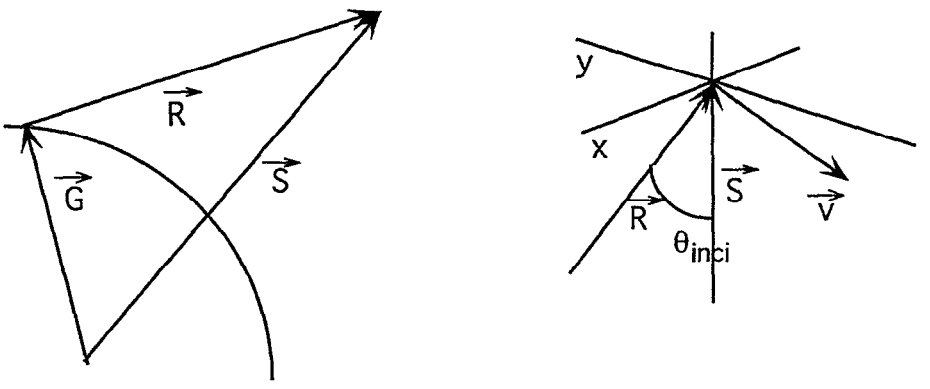

Fig. A2 - Left panel shows the global definitions of $\vec{G}$, $\vec{S}$, and $\vec{R}$; right panel show the coordinate system local to the satellite

diffraction pattern can be obtained immediately. The local coordinate system with $\hat{x}$ in the plane defined by $\vec{S}$ and $\vec{R}$ is

$$\hat{z} = -\hat{S} \ , \tag{A41}$$

$$\hat{y} = \frac{\vec{R} \times \vec{S}}{|\vec{R} \times \vec{S}|} \ , \tag{A42}$$

and

$$\hat{x} = \hat{y} \times \hat{z} \ . \tag{A43}$$

Hence

$$v_y = \frac{\vec{R} \times \vec{S}}{|\vec{R} \times \vec{S}|} \cdot \vec{v} \ , \tag{A44}$$

$$= \frac{(\vec{S} - \vec{G}) \times \vec{S}}{|(\vec{S} - \vec{G}) \times \vec{S}|} \cdot \vec{v} \ , \tag{A45}$$

$$= \frac{\vec{S} \times \vec{G}}{|\vec{S} \times \vec{G}|} \cdot \vec{v} \ . \tag{A46}$$

Similarly

$$v_x = \frac{\vec{R} \times \vec{S}}{|\vec{R} \times \vec{S}|} \times -\hat{S} \cdot \vec{v} \ , \tag{A47}$$

$$= \frac{\left[(\vec{S} - \vec{G}) \times \vec{S}\right]}{|(\vec{S} - \vec{G}) \times \vec{S}|} \times -\hat{S} \cdot \vec{v} \ , \tag{A48}$$

$$= \frac{\hat{S} \times \vec{S} \times \vec{G}}{|\vec{S} \times \vec{G}|} \cdot \vec{v} \ . \tag{A49}$$

Finally,

$$k_x = \left(\frac{2\pi}{\lambda}\right)\left(\frac{2v_x}{c}\right) \tag{A50}$$

and

$$k_y = \left(\frac{2\pi}{\lambda}\right)\left(\frac{2v_y}{c}\right) \quad . \tag{A51}$$

The numerical routine to determine k_x and k_y from the results provided by the orbital dynamics group is a distinct module to simplify testing. (See Section B.4 for the numerical routine that determines k_x and k_y from the results provided by the orbital dynamics group.)

Appendix B

SCILAB LISTINGS

B.1 Circular Retroreflector Directly Overhead Without Bevels

```
function [ z ] = curve( theda,phi )
erra=10^(-16)
errr=10^(-12)
theda=theda*10^(-6)
r=0.005
kl = 2*%pi/(0.532*10^(-6))
kx=kl*cos(phi)*theda
ky=kl*sin(phi)*theda
Ireal=2.0*integrate(['if abs(ky) > (10^(-6)) then cos(kx*x)*
          sin(ky*sqrt(r^2-x^2))/ky,';'else
          cos(kx*x)*sqrt(r^2-x^2),end'],'x',-r,r,erra,errr)
Iimg=2.0*integrate(['if abs(ky) > (10^(-6)) then sin(kx*x)*
          sin(ky*sqrt(r^2-x^2))/ky,';'else
          sin(kx*x)*sqrt(r^2-x^2),end'],'x',-r,r,erra,errr)
z=4.0*%pi*(Ireal^2+Iimg^2)/( (0.532*10^(-6))^2 )
```

B.2 Circular Retroreflector Off Normal Incidence Without Bevels

```
function [ z ] = lr(alpha,theda,phi )
erra=10^(-16)
errr=10^(-12)
theda=theda*10^(-6)
n=1.46
c=0.0001
alphan=asin(sin(alpha)/n)
r=0.005
r2=r^2
d=2*r*sqrt(2)
offset=c*tan(alpha)+d*tan(alphan)
kl = 2*%pi/(0.532*10^(-6))
kx=kl*cos(phi)*theda
ky=kl*sin(phi)*theda
lIreal=2.0*integrate(['if abs(ky) > (10^(-6)) then cos(kx*x)
          *sin(ky*sqrt(r2-(x-offset)^2))/ky,';'else
          cos(kx*x)*sqrt(r2-(x-offset)^2),end'],'x',-(r-offset),
          0.0,erra,errr)
```

```
uIreal=2.0*integrate(['if abs(ky) > (10^(-6)) then cos(kx*x)
          *sin(ky*sqrt(r2-(x+offset)^2))/ky,';'else
          cos(kx*x)*sqrt(r2-(x+offset)^2),end'],'x',0.0,(r-offset),
          erra,errr)
lIimg=2.0*integrate(['if abs(ky) > (10^(-6)) then sin(kx*x)
          *sin(ky*sqrt(r2-(x-offset)^2))/ky,';'else
          sin(kx*x)*sqrt(r2-(x-offset)^2),end'],'x',-(r-offset),
          0.0,erra,errr)
uIimg=2.0*integrate(['if abs(ky) > (10^(-6)) then sin(kx*x)
          *sin(ky*sqrt(r2-(x+offset)^2))/ky,';'else
          sin(kx*x)*sqrt(r2-(x+offset)^2),end'],'x',0.0,(r-offset),
          erra,errr)
z=4.0*%pi*((lIreal+uIreal)^2+(lIimg+uIimg)^2)/( (0.532*10^(-6))^2 )
```

B.3 Circular Retroreflector Off Normal Incidence With Bevels

```
function [ lrcs ] = kLRCS( theda,K,k)
// calculates the laser radar cross section for a retro, corner cube.
// The cube has a round aperture of radius r and beveled edges of
// width w. It is recessed a depth c in the holder. Its index is n.

// INPUT: theda in radians, k and K also.
// theda is the tilt angle and K and k are the x and y angles off the
// incident angle.

// This avoids k=0 singularity, k implicitly cancels if less than 10^(-6).
if abs(k) < (10^(-14)) then k=(10^(-14)), end

ka=1.1810498*10^7 // 2pi/532.0*10^(-9);
k=ka*k
K=ka*K
ro=3.33*10^(13) // 0.75*4*pi/(0.532*10^(-6))^2
r=0.005 ;     // cube aperture radius.
c=0.0015 // 1.0*10^(-3) ;     // depth of recess 10^-3 is about 40 mils
d=0.00707 ;     // distance to vertex, a*sqrt(2)
w=(1.016e-4)*2    // width of camfer on the cube's corner, 4 mills=1.016e-4
n=1.46 ;            // index of refraction
    thedan=asin(sin(theda)/n);
    offset=c*tan(theda)+d*tan(thedan);
      a=tan(%pi/6)
      b=w/(2*cos(%pi/6))
    x1=w/2;
    x2=w  // w/(2*sin(30degs))=w;
      alp=a^2+1
      bet=2*a*b+2*offset
      gam=b^2+offset^2-r^2
    x3=real(-bet+sqrt(bet^2-4*alp*gam))/(2*alp)
      bet=-2*a*b+2*offset
```

```
    x4=real(-bet+sqrt(bet^2-4*alp*gam))/(2*alp)
    x5=r-offset
if ( x2 < x4 ) & ( x1 < x5 ) & ( x4 < x5 ) & ( x1 < x3 )  then
kr=k*r;
z1=acos((x1+offset)/r);
z3=acos((x3+offset)/r);
z4=acos((x4+offset)/r);
z5=real(acos((x5+offset)/r));
y4=(x4+offset)/r;
y5=1.0 // (x5+offset)/r;
mz1=acos((-x1-offset)/r);
mz3=acos((-x3-offset)/r);
mz4=acos((-x4-offset)/r);
mz5=real(acos((-x5-offset)/r));
ak=a*k;
bk=b*k;
// Substitution: cos(z)=(x+offset)/r for even integrals above II. This
// helps the argument of the square root.
// It is written for better convergence.
err1=10^(-12);
err2=10^(-8);
// upper boundary of II
I1=integrate( 'sin(ak*x-bk)*cos(K*x)/k' ,'x',x2 , x4 ,err1,err2 ),

// upper boundary of III
I2=integrate( '-r*sin(kr*sqrt(1-y^2))*cos(K*(r*y-offset))/k' ,'y',y4,y5,
      err1,err2  ),

// lower boundary of I
I3=-integrate( 'sin(ak*x+bk)*cos(K*x)/k' ,'x',x1,x3,err1,err2  ),

// upper boundary of I
I4=integrate( 'r*sin(z)*sin(kr*sin(z))*cos(K*(r*cos(z)-offset))/k' ,'z',
      z1, z3,err1,err2  ),

// upper boundary of II
I5=integrate( 'sin(ak*x-bk)*sin(K*x)/k' ,'x',x2 , x4  ,err1,err2  ),

// upper boundary of III
I6=integrate( 'r*sin(z)*sin(kr*sin(z))*sin(K*(r*cos(z)-offset))/k' ,'z',
      z4,z5 ,err1,err2  ),

// lower boundary of I
I7=-integrate( 'sin(ak*x+bk)*sin(K*x)/k' ,'x', x1, x3,err1,err2  ),

// upper boundary of I
I8=integrate( 'r*sin(z)*sin(kr*sin(z))*sin(K*(r*cos(z)-offset))/k' ,'z',
      z1, z3,err1,err2  ),
```

```
// upper boundary of -II ; -II is the left mirror image of II
I9=integrate( 'sin(-ak*x-bk)*cos(K*x)/k' ,'x',-x4 ,-x2 ,err1,err2  ),

// upper boundary of -III
I10=integrate( 'r*sin(z)*sin(kr*sin(z))*cos(K*(r*cos(z)+offset))/k' ,'z',
      mz5,mz4,err1,err2  ),

// lower boundary of -I
I11=-integrate( 'sin(-ak*x+bk)*cos(K*x)/k' ,'x',-x3  , -x1   ,err1,err2  ),

// upper boundary of -I
I12=integrate( 'r*sin(z)*sin(kr*sin(z))*cos(K*(r*cos(z)+offset))/k' ,'z',
      mz3, mz1,err1,err2  ),

// upper boundary of -II
I13=integrate( 'sin(-ak*x-bk)*sin(K*x)/k' ,'x',-x4 , -x2  ,err1,err2  ),

// upper boundary of -III
I14=integrate( 'r*sin(z)*sin(kr*sin(z))*sin(K*(r*cos(z)+offset))/k' ,'z',
      mz5,mz4,err1,err2  ),

// lower boundary of -I
I15=-integrate( 'sin(-ak*x+bk)*sin(K*x)/k' ,'x', -x3, -x1,err1,err2  ),

// upper boundary of -I
I16=integrate( 'r*sin(z)*sin(kr*sin(z))*sin(K*(r*cos(z)+offset))/k' ,'z',
      mz3,mz1,err1,err2  ),

// combine all contributions
lrcs = (2)*(I1-I2+I3-I4+I9-I10+I11-I12-%i*(I5-I6+I7-I8+I13-I14+I15-I16) ),
else lrcs=0,end
lrcs=ro*abs(lrcs*conj(lrcs))
```

B.4 Conversion to $k_x k_y$

```
mode(-1)
// Program generates LRCS for passes found in sub directory passes.
//
// cube init, cnum is the number of cubes to be considered.
unix_w('date')
cnum=22;
print(%io(2),cnum)
// thada is the sperical angle from the z axis.
// phi is the angle from the x axis.
c=2.99*10^8
thada=2*%pi;

cub=zeros(cnum,3);
```

```
phi=16*%pi/180;
 for i=1:4,cub(i,1)=cos((i-1)*thada/4)*sin(phi);end
 for i=1:4,cub(i,2)=sin((i-1)*thada/4)*sin(phi);end
 for i=1:4,cub(i,3)=cos(phi);end
phi=32*%pi/180;
 for i=5:12,cub(i,1)=cos(%pi/8+(i-1)*thada/8)*sin(phi);end
 for i=5:12,cub(i,2)=sin(%pi/8+(i-1)*thada/8)*sin(phi);end
 for i=5:12,cub(i,3)=cos(phi);end
phi=48*%pi/180;
 for i=13:22,cub(i,1)=cos((i-1)*thada/10)*sin(phi);end
 for i=13:22,cub(i,2)=sin((i-1)*thada/10)*sin(phi);end
 for i=13:22,cub(i,3)=cos(phi);end

// klrcs returns LRCS for one cube kLRCS(theda,kxc,kyc),532nm
;getf("./klrcs.sci","c");

// Rot generates the rotation matrix to move the array coordinates
// to the cube coordinates.
// In function kLRCS from klrcs.sci the major axis of the cube aperture
// is always the y axis.
// Rxc normalized is the major axis and is pi/2+phi , phi the rotation axis.
// cos(pi/2+phi)=-sin(phi)
deff('[Rc]=Rot(R,c)',[
    'Rcr=[R(2)*c(3)-R(3)*c(2);R(3)*c(1)-R(1)*c(3);R(1)*c(2)-R(2)*c(1)]';
    'n=sqrt(Rcr(1)*Rcr(1)+Rcr(2)*Rcr(2)+Rcr(3)*Rcr(3))';
    'if n == 0 then Rc=[1,0;0,1],
      else Rc=[Rcr(2)/n,-Rcr(1)/n;Rcr(1)/n,Rcr(2)/n],end'
    ])
deff('[z]=cross(x,y)','z=[x(2)*y(3)-x(3)*y(2),x(3)*y(1)-x(1)*y(3),
      x(1)*y(2)-x(2)*y(1)]')

// macros to extract data from pass geometry found in a file in passes/
deff('[r]=r(i)','r=y(i,32)')
deff('[R]=R(i)','R=[y(i,18),y(i,19),y(i,20)]')
deff('[s]=S(i)','s=[y(i,6),y(i,7),y(i,8)]')
deff('[g]=G(i)','g=-[y(i,12),y(i,13),y(i,14)]')
deff('[v]=V(i)','v=-[y(i,9),y(i,10),y(i,11)]-[y(i,15),y(i,16),y(i,17)]')
deff('[ele]=el(i)','ele=y(i,31)')
deff('[t]=time(i)','t=y(i,3)*3600+y(i,4)*60+y(i,5)')
//
// LRCSA returns the LRCS for the 22 cube array
//
deff('[lra]=LRCSA(theda,kxa,kya,cub)',[ 'lra=0.0';
      'R=[sin(theda),0,cos(theda)]';
      'for i=1:cnum, c=[cub(i,1);cub(i,2);cub(i,3)]; kc=Rot(R,c)*[kxa;kya];
      lra=lra+kLRCS(acos(cub(i,3)),kc(1),kc(2)); end'] )
//
// get the data for passes
//
//
// Begin of main loop, reading in data from a different file
//
for p=1:1,// filnum(1,1), This was for multiple passes. Option is abandoned.
filename='lpm03234'
```

```
print(%io(2), filename)
load(filename)
// open file for output, time,lrcs,elevation
funit=file('open','array.dat','new')
ysize=size(y)
// creating arrays for storing data for future use.
lc=zeros(22,ysize(1,1))
l=1:ysize(1,1)
l=l*0
kx=l
ky=l
t=l
ele=t
vel=t
ang=t
slantr=t
for j=1:ysize(1,1),
// calculating the incident vector, normalized, and in the array coordinates
nR=R(j)/norm(R(j))
nS=S(j)/norm(S(j))
// z axis of the array is parallel to S, nadir pointing. Nza=cos(theda_inc)
Nza=-nR*nS'
sintheda=sqrt(1-Nza^2)
// Nadir case has Nza=1 and RxS=0, nRxS= INF
if Nza < 1.0 then
 RxS=cross(R(j),S(j));
 nRxS=RxS/norm(RxS);
 nV=V(j)/norm(V(j));
 Nya=sintheda*(nRxS*nV');
 RxSxS=cross(RxS,S(j));
 nRxSxS=RxSxS/norm(RxSxS);
 Nxa=sintheda*(nRxSxS*nV');
 Ninc=[Nxa,Nya,Nza];
 else Ninc=[0,0,1],end;
// V perpendicular to the direction of incidence
VxR=cross(V(j),R(j))/norm(R(j));
Vp=norm(VxR);
// va, velocity aberation
va=2*Vp/c
vel(j)=va
// project each cube on to the plane perpendicular to R then calculate lrcs
// test one nadir pointing cube
for i=1:cnum,
  Nc=[cub(i,1),cub(i,2),cub(i,3)];
  theda=acos((Ninc*Nc'));
  // The next is parallel to the cubes y axis
  yc=cross(Ninc,Nc)
  Nyc=yc/norm(yc)
  vay=va*Nyc(1)
  vax=va*Nyc(2)
kx(j)=vax
ky(j)=vay
ang(j)=theda
  if theda < 0.9 then lc(i,j)=kLRCS(theda,vax,vay),end
```

```
  l(j)=l(j)+lc(i,j)
  ,end
ele(j)=y(j,31)
t(j)=time(j)
slantr(j)=norm(R(j))
// End of loop for one pass
,end
// write time,elevation, and lrcs to a file
for j=1:ysize(1,1),write(funit,[t(j),l(j),ele(j),slantr(j)],'(4e12.5)'),end
file("close",funit)
// save lrcs for each point/cube
save('22lrcs',lc)
save('22t',t)
save('22ele',ele)
save('22range',slantr)
xsetech([0,0,1.0,0.5])
plot(t,l)
xtitle('LRCS vs time')
xsetech([0,0.5,1.0,0.5])
plot(t,ele)
xtitle('Elevation vs time')
xsetech([0,0,1.0,1.0])
pca=0.0
for ipca=1:ysize(1,1),
    if pca < y(ipca,31) then pca=y(ipca,31),
    date='September '+string(y(ipca,1))+','+string(y(ipca,2))+'
     '+string(y(ipca,3))+':'+string(y(ipca,4))
    ,end,end
scnum=string(cnum)
title=string(pca)+' degree PCA'+' '+date+' c_number '+scnum
xtitle(title)
// End of main loop
,end
unix_w('date')
```

Appendix C

SPACECRAFT ENGINEERING DEPARTMENT SPACE QUALIFICATION REPORT

C.1 Test Report for the Retroreflector Array

August 1996
Robert B. Patterson
Design Section, Code 8211
U.S. Naval Research Laboratory

C.1.1 Random Vibration Tests

The test article (RR-ST-1100-01 assembly) was subjected to two random vibration tests. One in the axial (Z-axis) direction and one in the lateral (X-axis) direction. Since the assembly is a symmetrical round dome, a test in the Y-axis direction was considered unnecessary.

The test article was assembled using flight-quality parts with the exception of the optics, which are identical to the flight-quality units in all physical characteristics, but have slight flaws in the optical properties. The qualification dome (RR-ST-1030-1) was not irradiated; this will have no effect on the fit of the parts to one another or the strength or stiffness of either that part or the assembly.

The lateral test was run first. The accelerometer data, from an accelerometer mounted on the shake table close to the test article, are shown in Fig. C1. The test article survived the random vibration test in the lateral axis.

The axial test was run next. The accelerometer data are shown in Fig. C2. The test article survived the random vibration test in the axial axis.

C.1.2 Shock Testing

The shock tests were next. Again, only an axial and lateral test were needed. The test was performed on the same shake table that was used to perform the random vibration tests. The accelerometer data were obtained the same way, with the accelerometer mounted on the test fixture close to the test article.

The axial shock test was completed first. The test article passed. The accelerometer data are shown in Fig. C3.

The lateral shock test was then run. The test article passed. The accelerometer data are shown in Fig. C4.

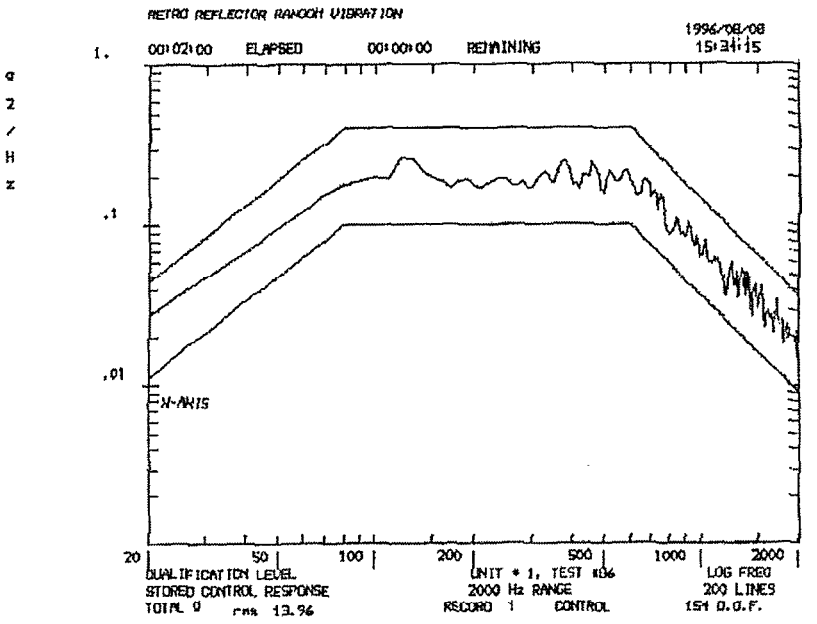

Fig. C1 - Lateral accelerometer data

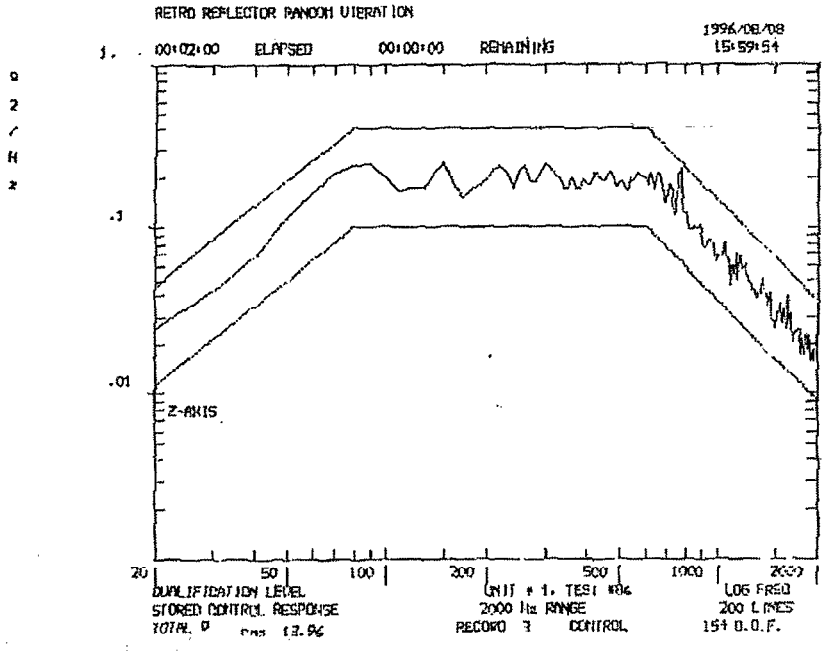

Fig. C2 - Axial accelerometer data

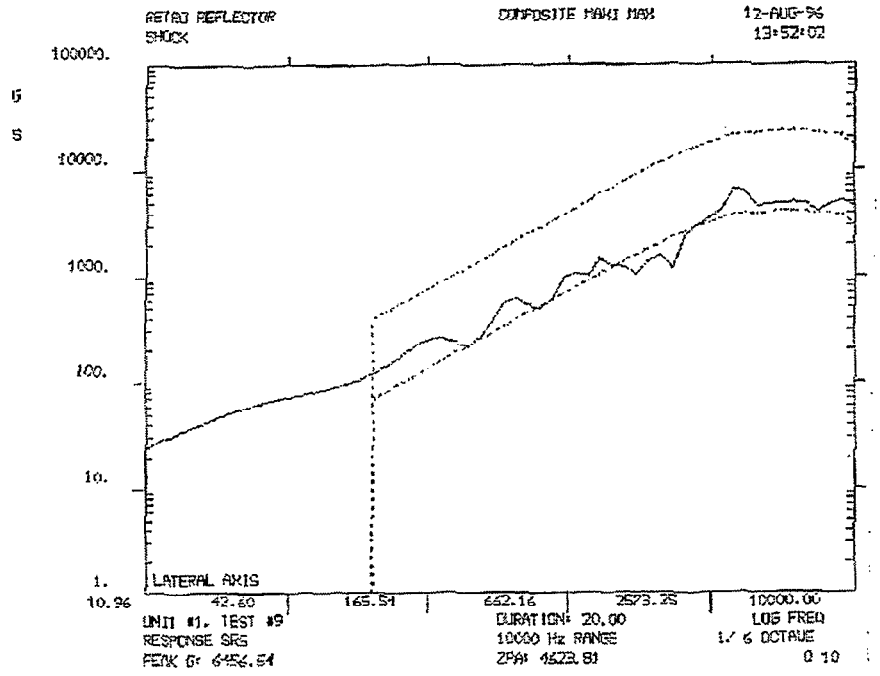

Fig. C3 - Axial shock accelerometer data

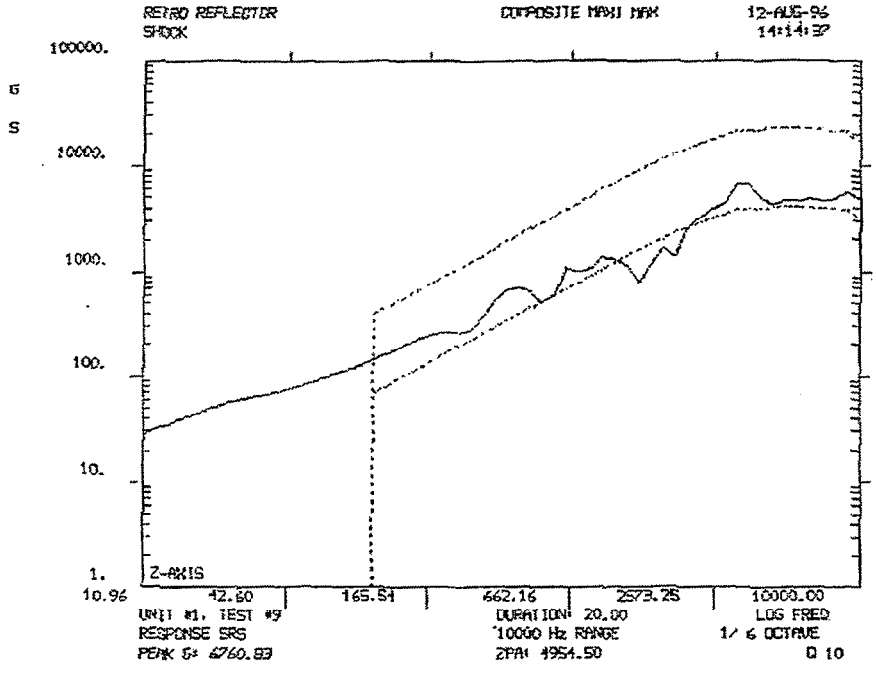

Fig. C4 - Lateral shock accelerometer data

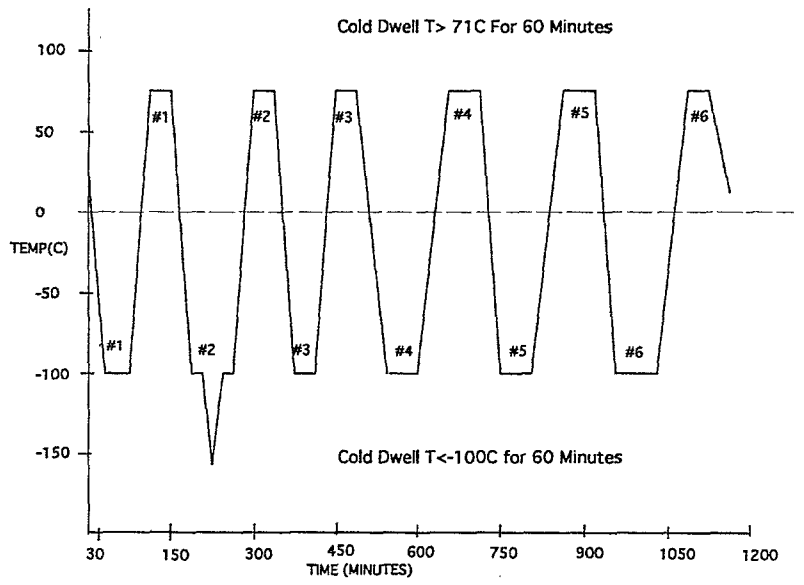

Fig. C5 - Thermal vacuum test temperature profile

C.1.3 Thermal Vacuum Testing

The qualification assembly was placed in a small vacuum chamber and cycled between the survival temperature extremes to verify that the assembly could survive the environments it will see while attached to the host. This was done by bolting the assembly to a small "cold" plate that had its temperature controlled by allowing liquid nitrogen to flow through copper tubing that was soldered to the backside of the copper "cold" plate or by applying power to electrical heaters that are attached to the front side of the plate, or some combination of the two. The plate had two thermocouples mounted to it. One was for feedback to the controller used to control the flow of liquid nitrogen; the other was used as the data for the test.

The test article was placed in the vacuum chamber, which was then pumped down to a vacuum of at least 0.0001 torr. The assembly was then subjected to temperature extremes of 71°C for the high temperature and −100°C for the low temperature. The assembly was held at each temperature extreme for a 1-h dwell period to ensure that the test article stabilized at the test temperature. The test consisted of 6 cold dwells alternated with 6 hot dwells.

The qualification assembly passed the test without suffering any failures. The test went according to plan, except when the control valve stuck open and the temperature went down to −157°C during the second cold dwell. Since the temperature stayed below the maximum of −100°C, this did not negate this part of the test. The faulty valve was changed out during the next transition from cold to hot dwell and the test continued. A time vs temperature graph of the test profile is shown in Fig. C5.

C.2 Test Procedure for the Retroreflector Array

June 19, 1996
Robert B. Patterson
Design Section, Code 8211
U.S. Naval Research Laboratory

C.2.1 Test Definition

C.2.1.1 Scope This document contains the requirements and procedures for the random vibration, shock, and thermal testing to be performed on the retroreflector array in order to qualify it for space flight on its host.

C.2.1.2 Test Objective The objective of this testing is to ensure that the retroreflector array is structurally sound and can withstand the launch and postlaunch environments without experiencing structural failure.

C.2.1.3 Pass/Fail Criteria

1. No parts (spring, retaining ring, retro seat, or retro optic) ejected from the assembly.
2. No noticeable permanent deformation around the seat area at the optic opening in the retroreflector housing.
3. No noticeable permanent deformation around the retaining ring groove area of the retroreflector housing.

C.2.1.4 Test Description Since the retroreflector assembly is a round part that is symmetrical about the axis of rotation, we will only have to test it in one longitudinal direction and the axial direction. We will mount the retroreflector assembly to the shaker table so that it is oriented for testing in the longitudinal direction. We will then run the test article through the 13.92 g rms random vibration test environment. We will then "hit" the test article with an extremely sharp impulse to simulate the shock environment (6000 g) specified by the host vehicle. We will now remount the retroreflector assembly so that it is oriented in the axial direction and repeat the random vibration and shock tests.

The thermal test consists of bolting the retroreflector assembly to a "cold" plate (that also has heaters installed on it), placing this assembly into a vacuum chamber, and then cycling the assembly through its survival temperature extremes six times.

C.2.1.5 Test Location The test will be conducted in the Naval Center for Space Technology's Payload Checkout Facility, Building A-59, at the Naval Research Laboratory in Washington, DC.

C.2.1.6 Responsibilities The Spacecraft Engineering Department is responsible for the overall performance of the test, the data reduction, and production of the final test report.

C.2.1.7 Test Log The test conductor shall maintain a daily test log that shall include a detailed record of the test progress, significant events and any deviations from the test procedures outlined in this document.

C.2.1.8 Photographic Coverage Photographs will be taken of the test specimens, test fixtures, and peripheral test equipment. Each transducer location will be marked and photographed.

C.2.2 Test Conditions

C.2.2.1 General The test will be conducted in the ambient temperature and pressure in the Payload Checkout Facility, Building A-59, Naval Research Laboratory.

C.2.2.2 Applied Loads The test articles shall be tested to the levels described by the host vehicle as listed in Appendix A NCST Qual. Procedures. The qualification unit shall be tested to qualification levels, and the flight unit shall be tested to acceptance levels.

C.2.2.3 Test Report A final test report will be prepared to document the test results. This report shall include overall test objectives, test article and test setup descriptions, reduced test data, test anomalies and/or significant observations, and a summary of the test results.

C.3 Final Acceptance Test Report of the Retroreflector Array

November 1996
Robert B. Patterson
U.S. Naval Research Laboratory

C.3.1 Random Vibration Tests

The flight units (RR-ST-1100-01 assembly) were each subjected to two random vibration tests, one in the radial (Z-axis) direction and one in the lateral (X-axis) direction. Since the assembly is a symmetrical round dome, a test in the Y-axis direction was not considered necessary.

The flight units were assembled using flight-quality parts and were labeled assembly A, B, and C. The flight units were tested to acceptance (flight) levels 6 dB below qualification for a total of 6.92 g rms.

The lateral test was run first. The accelerometer data, from an accelerometer mounted on the shake table close to the test article, are shown in Figs. C6, C7, and C8. The flight units survived the random vibration test in the lateral axis.

The axial tests were run next. The accelerometer data are shown in Figs. C9, C10, and C11. The flight units survived the random vibration test in the axial axis.

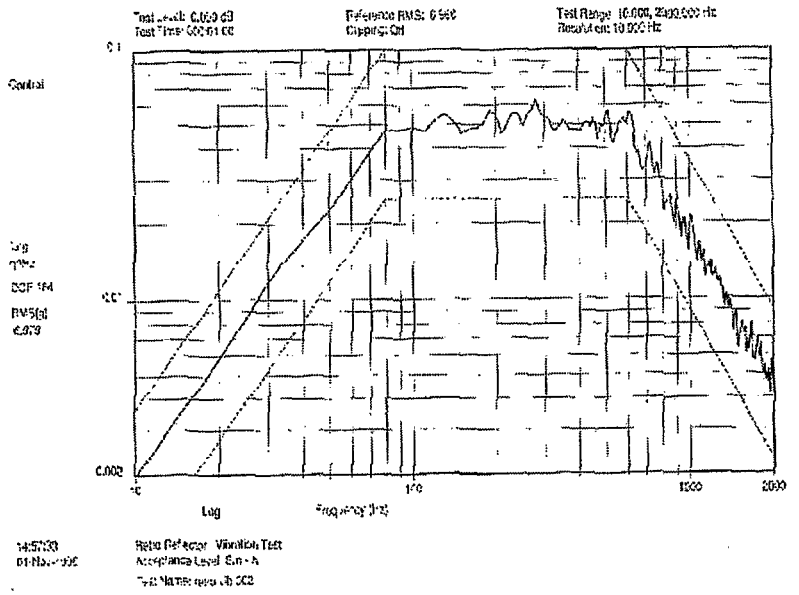

Fig. C6 - Lateral accelerometer data, acceptance level S/n -A

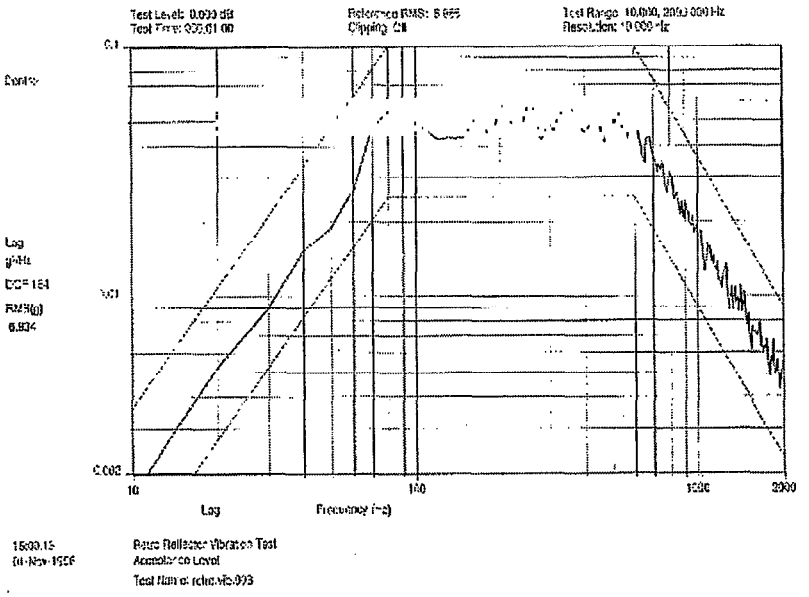

Fig. C7 - Lateral accelerometer data, acceptance level S/n -B

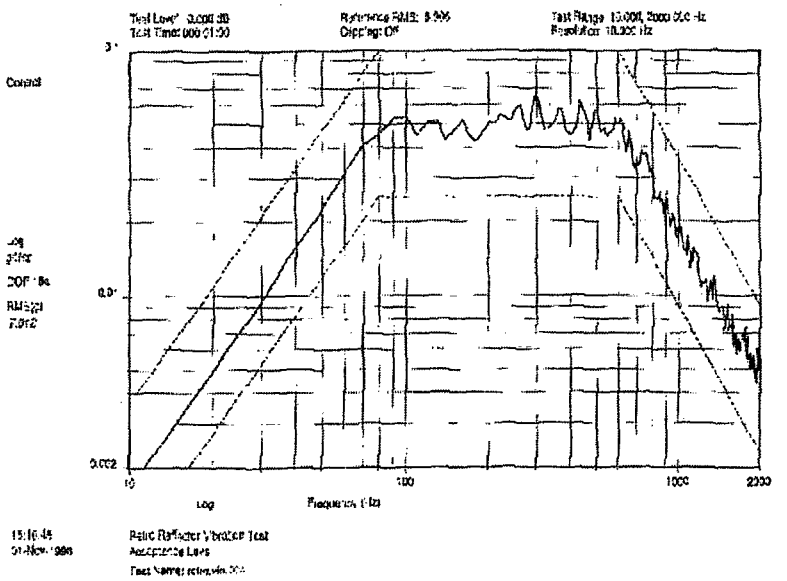

Fig. C8 - Lateral accelerometer data, acceptance level S/n -C

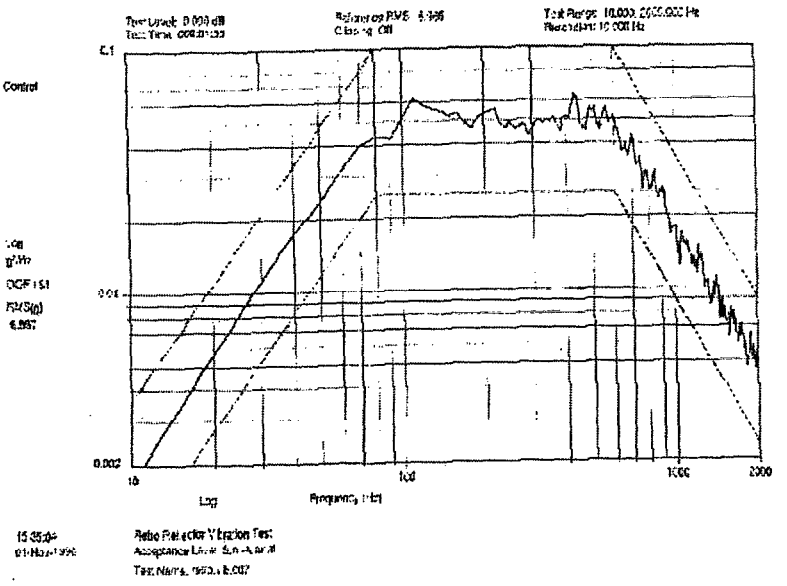

Fig. C9 - Axial accelerometer data, acceptance level S/n -A

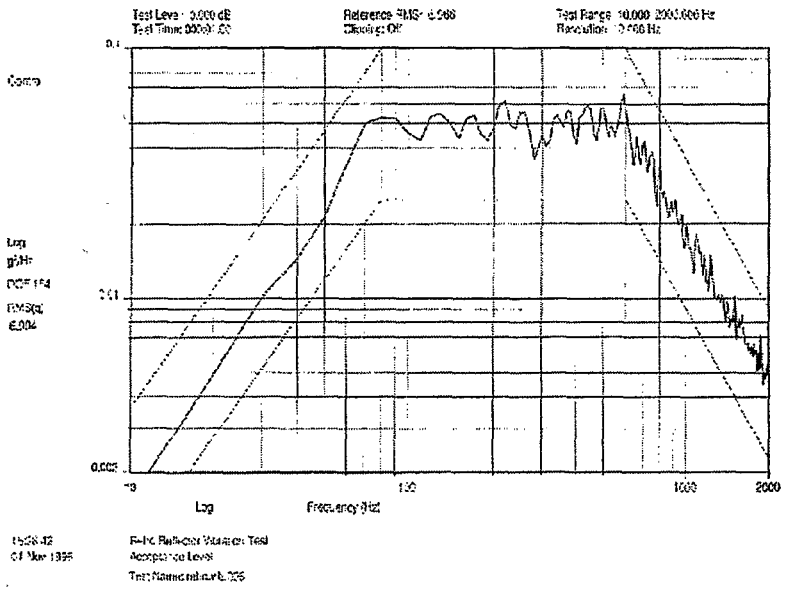

Fig. C10 - Axial accelerometer data, acceptance level S/n -B

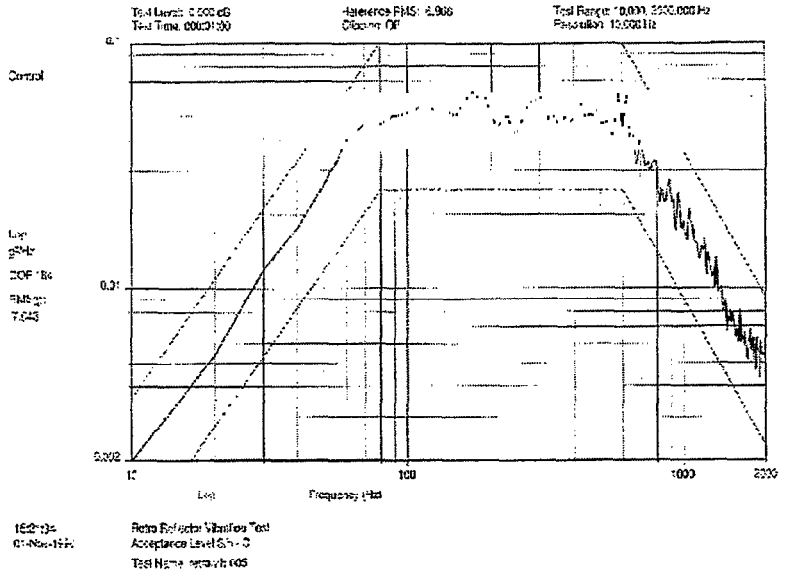

Fig. C11 - Axial accelerometer data, acceptance level S/n -C

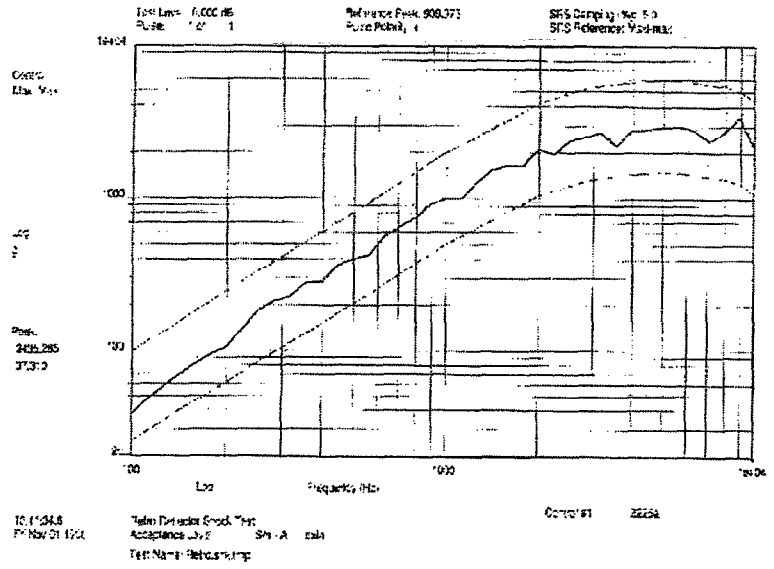

Fig. C12 - Axial shock accelerometer data, acceptance level S/n - A

C.3.2 Shock Testing

The shock tests were next. Again, only an axial and lateral test were needed. The test was performed on the same shake table that was used to perform the random vibration tests. The accelerometer data were obtained the same way, with the accelerometer mounted on the test fixture close to the test article.

The axial shock test was completed first. The flight units passed. The accelerometer data are shown in Figs. C12, C13, and C14.

The lateral shock test was then run. The flight units passed. The accelerometer data are shown in Figs. C15, C16, and C17.